1993

Cluster chemistry of reduced zirconium bromide compounds: syntheses and characterization

Ru-Yi Qi
Iowa State University

Recommended Citation

Qi, Ru-Yi, "Cluster chemistry of reduced zirconium bromide compounds: syntheses and characterization " (1993). *Retrospective Theses and Dissertations*. 10855.
https://lib.dr.iastate.edu/rtd/10855

INFORMATION TO USERS

This manuscript has been reproduced from the microfilm master. UMI films the text directly from the original or copy submitted. Thus, some thesis and dissertation copies are in typewriter face, while others may be from any type of computer printer.

The quality of this reproduction is dependent upon the quality of the copy submitted. Broken or indistinct print, colored or poor quality illustrations and photographs, print bleedthrough, substandard margins, and improper alignment can adversely affect reproduction.

In the unlikely event that the author did not send UMI a complete manuscript and there are missing pages, these will be noted. Also, if unauthorized copyright material had to be removed, a note will indicate the deletion.

Oversize materials (e.g., maps, drawings, charts) are reproduced by sectioning the original, beginning at the upper left-hand corner and continuing from left to right in equal sections with small overlaps. Each original is also photographed in one exposure and is included in reduced form at the back of the book.

Photographs included in the original manuscript have been reproduced xerographically in this copy. Higher quality 6" x 9" black and white photographic prints are available for any photographs or illustrations appearing in this copy for an additional charge. Contact UMI directly to order.

U·M·I

University Microfilms International
A Bell & Howell Information Company
300 North Zeeb Road, Ann Arbor, MI 48106-1346 USA
313/761-4700 800/521-0600

Order Number 9414016

Cluster chemistry of reduced zirconium bromide compounds: Syntheses and characterization

Qi, Ru-Yi, Ph.D.

Iowa State University, 1993

U·M·I
300 N. Zeeb Rd.
Ann Arbor, MI 48106

Cluster chemistry of reduced zirconium bromide compounds: syntheses and characterization

by

Ru-Yi Qi

A Dissertation Submitted to the
Graduate Faculty in Partial Fulfillment of the
Requirements for the Degree of
DOCTOR OF PHILOSOPHY

Department: Chemistry
Major: Inorganic Chemsitry

Approved:

Signature was redacted for privacy.

In Charge of Major Work

Signature was redacted for privacy.

For the Major Department

Signature was redacted for privacy.

For the Graduate College

Iowa State University
Ames, Iowa

1993

TABLE OF CONTENTS

INTRODUCTION

During the last 30 years or so, an extensive cluster chemistry has been established in the early transition metal halide systems. The first group of cluster compounds,[1-2] e.g., $K_4Nb_6Cl_{18}$,[3] Ta_6Cl_{15},[4] Nb_6F_{15},[5] and Nb_6Cl_{14},[6] were synthesized and characterized in the mid- and late-1960s. They all contain M_6 octahedra which are sheathed by 12 edge-bridging halide ligands (inner halogen, or X^i's) (Figure 1). An additional feature characteristic of the M_6X_{12} clusters was the apparent existence of a set of low-energy bonding orbitals extending radially from the vertices of the M_6 cluster cores, which were always occupied by some means by other halide ligands (outer or terminal halogen atoms, X^a's).[7] Owing to the presence of this set of orbitals and the numerous ways in which they can be occupied, a variety of metal to halogen stoichiometries as well as a diversity of structure types have been observed.

According to the function of the inner halogen atoms, there is another group of cluster compounds with M_6 cluster cores that are face-capped by eight halogen or chalcogen atoms. The M_6X_8 clusters are usually found in the situations where higher electron counts and larger anion ligands are available as in Ti_5Te_4,[8] Nb_6I_{11},[9-10] Nb_6I_9S,[11] and Mo_6S_8.[12] The recent studies in the mixed halide and chalcogenide systems offer another series of compounds in which the M_6X_8 cluster cores remain while the terminal ligands are replaced by the smaller halogen atoms.[13-14]

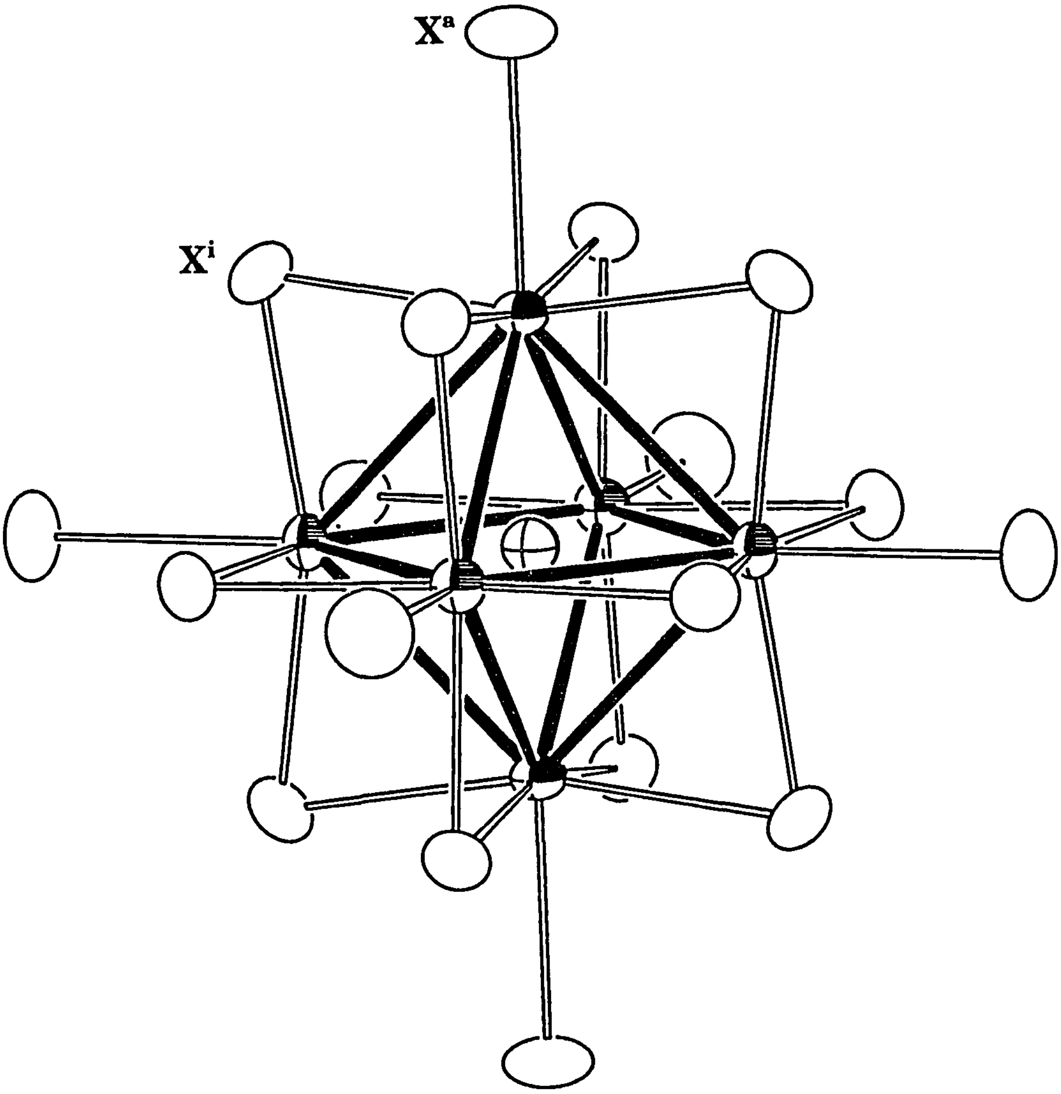

Figure 1. A centered M_6X_{12} - type cluster. Open ellipsoids are X atoms, and shaded and crossed ellipsoids are M and interstitial atoms, respectively. The six terminal X^a atoms are included for completeness

A great number of unique as well as similar cluster compounds have been realized in the electron-poorer halide systems, i.e., group III and IV metal systems, with the presence of an additional chemical and structural component, an interstitial atom in the center of M_6 octahedra.[15-18] In the early days, this phenomenon was treated as an impurity problem, and the accidental interstitial elements were limited to the light main group elements, i.e., H, C, N, and O. It was not until the late 1970s that the importance of the interstitial elements was recognized, systematically investigated, and theoretically rationalized. The interstitial atoms in the center of M_6 cluster cores not only have appropriate orbitals to strongly interact with those of the host atoms but also contribute their valence electrons to the otherwise electron-deficient M_6 clusters. In other words, these interstitial atoms serve as a binding force to hold the host atoms into the cluster unit. Since then, elements which cover a large portion of the periodic table have been consciously introduced into the syntheses. The research started with the light main-group elements, and later extended to the heavier ones, i.e., Al-P, and Ge.[19-20] Before long, cluster compounds stabilized by 3d transition-metal elements were prepared, which updated the concept of the interstitial elements. The next breakthrough was the incorporation of 4d and 5d transition-metal elements into the cluster cores,[21-26] especially marked by the discovery of several condensed "supercluster" phases.[27-28] As the number of valence electrons of interstitial elements varies, it became possible to systematically study the electronic configurations of the cluster phases. The investigations revealed that the optimal electron counts for the clusters stabilized by main-group elements was 14,[29-31] and 18 for those centered by transition-metal elements,[32-33] with a few exceptions. In both cases, a closed-shell electronic configuration was achieved with a sizable gap between the highest filled (HOMO) and the lowest empty (LUMO) state.

Among the centered cluster phases, the zirconium chloride and the zirconium iodide systems were the most investigated and best understood. As a result of more than ten years of persistent efforts, more than 25 structure types [15,18,30] have been discovered in the zirconium chloride system, and a rich solid state chemistry has been revealed, in company with the advance of synthetic techniques, and the development of new characterization methods. Each Zr-X cluster phase prepared via a high temperature solid state reaction route can be classified as a member of the $M_m(Zr_6X_{12}Z)X_n$ series,[30] where M = alkali metal, alkaline-earth metal, rare-earth metal, Zr, or several; Z = H, Be-N, Al-P, Ge, and Mn-Ni; X = Cl, Br, and I; $0 \leq n \leq 6$; $0 \leq m \leq 6$. Even though there have been only two structure types found in the zirconium iodide system, the studies revealed a fruitful interstitial chemistry as many more interstitial elements, especially those larger ones, e.g., Al, Si, P, and Ge, could be incorporated into the iodide cluster compounds.[19-20] In addition, a new cluster chemistry that fills the gap between traditional solid state chemistry and conventional solution chemistry has also been established.[21,34]

The earlier investigations in the zirconium bromide system afforded several cluster compounds.[15-16,35-36] The structure types of these bromide phases, however, were all known for the corresponding chloride or iodide compounds, e.g., $Zr_6I_{12}C$, $Zr_6Cl_{13}B$, and so on. Therefore, further study of the zirconium bromide system was more or less discouraged by these results. Recently, both the interests and research activities in the zirconium bromide system have been reinitialized by the preliminary results obtained in the zirconium-mixed halide system.[37] Not only were the compounds with the known structure type ($Zr_6Cl_3I_9Be$, $Zr_6I_{12}C$ type), or with modified structure type (tetragonal $Zr_6Cl_{11.4}I_{1.6}B$, related to orthorhombic $Zr_6Cl_{13}B$) found in the Zr-Cl-I system, but evidence for new structure types was observed in the Guinier powder patterns as well. Single crystal structure refinements were carried out on $Zr_6Cl_3I_9Be$ and $Zr_6Cl_{11.4}I_{1.6}B$, and it turned out that some of the halide positions in these two phases were occupied by both Cl and I. Considering the nominal atomic number as well as the bond distances to the adjacent atoms, one realized that the mixed halide position behaved rather like a bromine position. In other words, new structure types might be found in the zirconium bromide system.

So far, more than thirty new zirconium bromide cluster compounds have been synthesized over 10 structure types. More importantly, four distinctive new structure types which have not been observed in the other systems have been realized (Table 1). Besides different cluster linkages found in the zirconium bromide frameworks, novel polycations $[M_4Br]^{3+}$, where M = Na, K,

Table 1. Structure types and connectivities of all the known $M_m[Zr_6Br_{12}Z]Br_n$ classes, where m=0-8; n=0-6

Structure type	Connectivity	Reference
$Zr_6I_{12}C$	$[Zr_6I^{i}_{6}I^{i-a}_{6/2}]I^{a-i}_{6/2}$	29, 38
$Zr_6Cl_{13}Be$	$[Zr_6Cl^{i}_{10}Cl^{i-i}_{2/2}]Cl^{a-a}_{6/3}$	15
Nb_6Cl_{14}	$[Nb_6Cl^{i}_{10}Cl^{i-a}_{2/2}]Cl^{a-i}_{2/2}Cl^{a-a}_{4/2}$	6
$CsNb_6Cl_{15}$	$[Zr_6Cl^{i}_{12}]Cl^{a-a}_{6/2}$	39
$K_3Zr_6Cl_{15}Be$	$[Zr_6Cl^{i}_{12}]Cl^{a-a}_{6/2}$	40
$Cs_3Zr_6Br_{15}C$	$[Zr_6Br^{i}_{12}]Br^{a-a}_{6/2}$	this work
$Rb_5Zr_6Br_{15}Be$	$[Zr_6Br^{i}_{12}]Br^{a-a}_{6/2}$	this work
$Na_4Zr_6Cl_{16}Be$	$[Zr_6Cl^{i}_{12}]Cl^{a-a}_{4/2}Cl^{a}_{2}$	42
$(Cs_4Br)Zr_6Br_{16}B$	$[Zr_6Br^{i}_{12}]Br^{a-a}_{4/2}Br^{a}_{2}$	this work
$Ba_2Zr_6Cl_{17}B$	$[Zr_6Cl^{i}_{12}]Cl^{a-a}_{2/2}Cl^{a}_{4}$	43
$K_4Zr_6Br_{18}C$	$[Zr_6Br^{i}_{12}]Br^{a}_{6}$	this work
$(K_4Br)_2Zr_6Br_{18}B$	$[Zr_6Br^{i}_{12}]Br^{a}_{6}$	this work

Rb,or Cs, have been found in the zirconium bromide lattices as well. The formation of the $[M_4Br]^{3+}$ polycations not only pushes the limit of countercation number from 6 to 8 or even higher, but it also extends the functionalities of the countercations as well as those of the halide ligands in the cluster compounds.

The remainder of the thesis will be grouped into sections. Besides the synthesis and characterization techniques which will be discussed in the next chapter, the major portion of the thesis will focus on the new zirconium bromide cluster phases synthesized and characterized since 1992. The results will be presented in the order of increasing Zr/Br ratio. Under each given Zr/Br ratio, cluster examples are further divided into groups according to their structure types and stoichiometries. In addition, their structural relationship with other known cluster phases, and the magnetic properties will be emphasized as well.

EXPERIMENTAL

Starting Materials

Zirconium powder was prepared by the hydrogenation-dehydrogenation method. Reactor-grade zirconium metal (<500 ppm Hf) was obtained from the Ames Laboratory in the form of cold-rolled sheets with 0.3-0.5mm thickness. The metal strips were cleaned in a mixed acid solution (45% conc. HNO_3, 10% conc. HF, and 45% H_2O by volume), thoroughly rinsed with water, and dried in the air. For a typical preparation, about 10 grams of cleaned zirconium strips were loaded in a Mo boat which was later placed in a fused silica container. The container was evacuated and purged with hydrogen (Matheson, 99.999%) at least three times before being heated to 450°C under an atmosphere of hydrogen. Following a rapid hydrogen uptake, the temperature was gradually increased to about 600°C to speed up and assure the diffusion of hydrogen into the bulk of zirconium strips. After being cooled to room temperature under the hydrogen atmosphere, the container was evacuated and brought into a glovebox (VAC, HE 493) filled with N_2. The hydrogenated zirconium strips ($ZrH_{\sim1.5}$) were ground with a diamond mortar and pestle until the powder could pass through an 100-mesh sieve. The $ZrH_{\sim1.5}$ powder was reloaded into the Mo boat and dehydrogenated by slowly heating under dynamic vacuum to 300°C, around which the absorbed hydrogen started coming out. The temperature was eventually raised to 700°C to minimize the remaining hydrogen. After being cooled, the container was brought back to the glovebox and the zirconium was reground to pass through an 100-mesh sieve. The refined lattice constants were within 3σ of the reported value for zirconium metal.

$ZrBr_4$ was made by the direct reaction of the elements in a sealed, two-armed fused silica vessel. The end containing the high purity liquid Br_2 (0.02% Cl_2, A.D. Mackay) was kept in a warm water bath (40-50°C), while the other end, which contained cleaned zirconium strips, was heated by a tube furnace. The reaction started at about 300°C, and the temperature was slowly increased to 450°C and kept at this value until the reaction finished. The raw $ZrBr_4$ was purified by multiple sublimations over zirconium metal and through a frit under dynamic vacuum. The sublimed $ZrBr_4$ was poorly crystallized and had a light creamy color.

Reagent grade alkali-metal bromides were slowly dried under dynamic vacuum at a temperature below 200°C and then sublimed. The alkaline-earth metal bromides were prepared by slow decomposition of the corresponding hydrate under dynamic vacuum. Their Guinier powder patterns were usually taken to confirm that the desired bromides were free of hydroxides, oxides, or oxybromides. All the starting materials mentioned above were stored either in sealed ampoules or divided into small amounts and kept separately in stoppered vials that were stored in Mason jars in the dry box.

Interstitial atoms, Be, B, C, Fe, and Mn were introduced into the syntheses as elements. Amorphous B (Aldrich, 99.999%) and small Be chunks (Aldrich, 99.9%) were degassed at room temperature and stored in small vials in the glovebox. Spectroscopic grade graphite (National Brand, Union Carbide) was utilized as the source of C. An Fe powder (Baker, analyzed reagent) and Mn chips (Johnson Matthey, 99.99%) were used in the reactions with either Fe or Mn as interstitials.

Synthetic Techniques

The study of interstitially stabilized early transition-metal and rare-earth metal halide cluster compounds was started after the existence of adventitious impurities, namely, H, C, O, etc, was recognized in their "binary compounds".[44-48] These unexpected elements have been one of the major concerns in the preparation of the cluster phases with desired interstitial elements, especially with those light main group elements, such as H, Be, B, C, N, O, and so on. Therefore, precautions needed to be taken in every stage of the syntheses. Because of the limited analytical methods available for the small main-group elements in the centered cluster phases and the limited power of X-ray diffraction methods, the confirmation or identification of the presence of these light interstitial elements are mainly based on what were loaded and the relative yields of the cluster phases of interest. Generally, most of the cluster phases could be made with >90% yield. To some extent, the refined Guinier lattice constants could also be used to differentiate interstitials.

What made it more difficult to avoid introduction of these unexpected impurities into reactions was that both the starting materials and products were air- and moisture-sensitive. In other words, reactions could be very easily contaminated with H_2O or O_2 if not handled carefully. Besides, the reduced halide cluster phases and the metals themselves could readily attack the Pyrex or fused silica containers at the elevated temperatures necessary to form clusters (>600°C). The former problem has been overcome by using glovebox and vacuum techniques, and the latter was avoided by utilizing welded Ta or Nb tubing as reaction containers.[49] For zirconium halide systems, Ta rather than Nb tubing was used for the following reasons. Firstly, it has been shown by both visual observation and SEM analysis that the inner surface of the Ta tubing was not attacked under the chosen reaction temperatures (800-1000°C). Secondly, in case Ta was involved in the cluster formation, though not observed yet, the large difference between the atomic number of Zr and Ta would make the characterization process much easier.

The preparation of Ta containers was usually started with cutting 3/8" or 1/2" Ta tubing into 4-5 cm lengths, etching them in a Ta cleaning solution (25% conc. HNO_3, 20% conc. HF, and 55% conc. H_2SO_4 by volume), thoroughly rinsing and soaking with water, and then drying them in the air. Failure to do so resulted in reactions that could be easily contaminated by the elements in the cleaning solution. Following the cleaning procedure, one end of the Ta tube was crimped and heliarc welded.[50] Prior to use, these welded tubes were not cleaned further as the acid solutions trapped in the crimped end could not be easily removed.

For a typical Zr-Br reaction, about 200-250 mg of starting materials were usually loaded. The ratio of each starting material was calculated according to the stoichiometry of a designed target phase. After the Ta tubes were loaded and the other end was tightly crimped in the dry box, they were brought out in air-tight containers. The only time when the loaded, yet tightly crimped Ta tubes were exposed to the air, was during their transfer into the welder. Once transferred, the welder was quickly evacuated and purged with He gas, and then the Ta tubes were welded under a He atmosphere at slightly negative pressure. To prevent Ta tubes from being oxidized in the air at the chosen temperatures (800-1000°C), these loaded Ta containers were encased in fused silica jackets. The Ta containers as well as the inner surface of the jackets were cleaned with Ta cleaning solution, carefully yet thoroughly rinsed with water and acetone, and then dried in the oven (100°) for 10 minutes. Before being sealed under vacuum (~10^{-4} torr), the jackets were heated with a natural gas/oxygen flame to get rid of any possible residual moisture or air absorbed on the inner surface of the jackets.[51-52] The temperatures used to run Zr-Br reactions were around 800-850°C, similar to those used for Zr-Cl and Zr-I reactions. For the reactions containing alkaline-earth metals as countercations, higher temperatures of 900-1000°C were preferred. The reaction period was usually about 2-4 weeks. In some cases, a longer period and/or a vapor transporting agent $AlBr_3$ was employed in order to enhance the crystal growth. All reactions were opened in another glovebox that was equipped with a nearly horizontal window and a microscope to allow visual examination of reaction products and mounting of single crystals. Crystals, which looked suitable for single crystal studies, were picked up with a thin glass fiber (0.05-0.1 mm) that had a tiny amount of vacuum grease on the tip and were mounted into 0.3-0.5 mm thin walled glass capillaries. The open ends of the capillaries were filled with vacuum grease to avoid exposure of the crystals to the air, and then the capillaries were sealed with a natural gas/oxygen flame outside the box. Powder diffraction samples were routinely mounted for all reaction products and the rest of the products were kept in sealed Pyrex ampoules.

Methods of Characterization

Visual Examination: Whenever a reaction was opened, a careful visual inspection was made before mounting crystals and powder diffraction samples. This helped to check the number of different phases and their relative yields in a multi-product reaction because different phases may have different colors and morphologies. Thus, separate powder patterns could be taken to simplify the process of characterization. Some side products, namely, ZrBr (black hexagonal flakes), $ZrBrO_x$ (golden colored flakes), and M_2ZrBr_6 (white powder or transparent crystals) could be exclusively recognized by their appearances. Doing so also helped in the estimate of the stoichiometry of the unknown phases if any.

Powder Diffraction Method: As mentioned earlier, Guinier powder diffraction was routinely carried out on the products of every reaction to characterize the phases, estimate the relative yield, and obtain lattice parameters if necessary. Diffraction patterns were recorded on films photographically on an evacuable Hägg-Guinier camera with a bent quartz crystal monochromator which was adjusted to give nearly clean Cu Kα1 radiation (λ=1.540562Å). Samples were mounted in between two layers of Scotch tape together with a small amount of Si (SRM-40) as an internal standard. Whenever necessary, a non-water-based tape was utilized to prevent the decomposition of the sample in contact with the emulsion. The 2θ range was from 2-85°, within which 5 silicon lines were recorded (the zero line was not included). The evacuable Guinier camera not only gave the powder pattern a lower background but also minimized the exposure of the sample to the air.

Powder patterns of known or proposed structure types were calculated using the program POWDER (version 6)[53] and plotted on the appropriate scale for direct comparison with recorded Guinier film data. This greatly helped to recognize the unknown phases. If new compounds with known structure types were found, their powder patterns were read on an ENRAF NONIUS Guinier viewer with 0.005 mm precision. These values were converted to 2θ value by program GUIN[54] using a quadratic equation derived from the positions of the standard Si lines. After the indices were assigned manually to each reflection, the lattice constants were refined with program LATT.[55] In the cases of new phases with unknown structure types, Program TREOR (version 5)[56] was tried to index the powder patterns, yet with limited success.

Single Crystal X-Ray Studies: To large extent, the characterization of new structure types depended mainly on the single crystal X-ray diffraction study. This could give not only the stoichiometries but also the crystal structure features of new phases. Prior to data collection, the quality of each crystal was always checked with oscillation photos on a Weissenberg camera. If possible, Weissenberg films of more than one layer were also taken to get the cell dimensions, lattice symmetry, and extinction conditions. In some cases, Weissenberg films were taken after the structure was solved to verify the absence of possible superstructures or to confirm certain extinction conditions.

In this research, most of data collections were performed at ambient temperatures on a RIGAKU AFC6R or ENRAF NONIUS CAD4 diffractometer. They are both automated and equipped with a graphite monochromator to give Mo Kα radiation (λ=0.71073Å). The former with a rotating anode was operated at higher power to generate a stronger beam, which provided a better opportunity to study compounds with weak superstructures or weakly diffracting crystals.

Both diffractometers have softwares that conveniently gave cell dimensions, lattice symmetry, orientation matrix, which were essential for the data collection. For each data set, three intense reflections were used as standards to monitor any possible decay or the instrument instability. Following data collection, a ψ-scan at intervals of 10° in ϕ was collected on at least three intense reflections near $\chi=\pm 90°$ for use in an empirical absorption correction. Details of individual data collection have been included in each section of results.

Data sets, usually with redundant data, were examined to confirm the Laue symmetry and to determine the space group if possible. The data processing included Lorentz-polarization correction, decay correction with standards if necessary, and empirical absorption correction using an average ψ-scan measurement. The data thus processed were averaged according to the corresponding point group to generate a reduced data set which was used in structure determination and refinement.

If a phase adopted a known structure type, the positional parameters of an isostructural compound were employed in the initial stage of structure refinement. If the phase had a new structure type, the direct method provided by SHELXS-86 [57] was utilized to obtain an initial model. After atoms were located, structure refinements were carried out with full matrix least-square calculation and standard Fourier syntheses provided by TEXSAN.[58] The structure factors were calculated using neutral atomic scattering factors corrected for both the real and imaginary parts of anomalous dispersion for the elements with $Z>10$.[59] Following the anisotropic refinement, the secondary extinction coefficient was refined. For the compounds with light main group elements as interstitials, only isotropic thermal parameters were refined for the interstitial elements. In the final stage, occupancies of countercations if any, were refined, and a final difference Fourier map was calculated to get the information on residual electron densities, and to evaluate the quality of the solution.

For each structure solution, ORTEP[60] pictures of the unit cell, important structural fragments and local environment of countercations are presented under each structure type to illuminate its unique crystal structure features. Some important data collection parameters and results from data processing and structure refinement are reported in the crystal data table for each compound. The positional and anisotropic thermal parameters, as well as important bond distances and angles are compiled in the corresponding tables. In all cases, the refined Guinier powder cell constants were employed to calculate the bond distances and angles as the former usually have higher accuracy than those obtained from single crystal diffractometers. Some of the terms that appear in tables are defined as follows:

1) Linear Absorption Coefficient μ

$$\mu = \frac{1}{V_c} \sum_i n_i \mu_{ia}$$

where V_c is the unit cell volume and n_i is the number of a given atom in the unit cell. μ_{ia} is the atomic absorption coefficient tabulated in the International Tables.[59]

2) Secondary Extinction Coefficient g[61]

$$|F_o| = \frac{|F_c|}{1 + g|F_c|^2 Lp}$$

where L and p are the Lorentz and polarization factors.

3) The R factor for averaging data

$$R_{ave} = \frac{\sum_{i=1}^{n} \sum_{j=1}^{m} |<F_i^2> - F_{ij}^2|}{\sum_{i=1}^{n} m<F_i^2>}$$

where n is the number of unique reflections that was observed more than once and m is the number of times a given reflection was observed. $<F_i^2>$ is the average value of F^2 for a unique reflection i.

4) The crystallographic R factors

$$R = \frac{\sum_{i=1}^{n} (|F_{obs}|_i - |F_{calc}|_i)}{\sum_{i=1}^{n} |F_{obs}|_i}$$

$$R_w = \left(\frac{\sum_{i=1}^{n} w_i (|F_{obs}| - |F_{calc}|)^2}{\sum_{i=1}^{n} w_i |F_{obs}|^2} \right)^{1/2}$$

For refinements based on F, w = 1 / σ_F^2

5) The coefficient U_{ij} of the anisotropic temperature factor expressions are defined as follows:

$$T = exp[-2\pi^2(U_{11}h^2a^{*2} + U_{22}k^2b^{*2} + U_{33}l^2c^{*2}$$
$$+2U_{12}hka^*b^*\cos\gamma^* + 2U_{13}hla^*c^*\cos\beta^* + 2U_{23}klb^*c^*\cos\alpha^*)]$$

and the equivalent isotropic temperature factor is defined as

$$B_{eq} = \frac{8\pi^2}{3} \sum_{i=1}^{3} \sum_{j=1}^{3} U_{ij} a_i^* a_j^* \vec{a}_i \cdot \vec{a}_j$$

Magnetic Susceptibility Studies: In this research, magnetic susceptibility measurements were done mainly on the compounds with unusual and new structure types and/or interesting electronic properties indicated by the structure refinement. The magnetic data were collected on a SQUID (Quantum Design) by Mr. Jerome Ostenson. Data collection was usually carried out in a field of 3 Tesla, over the temperature range of 6-300K. Both the sample holder and diamagnetic core corrections were applied before any calculations were made. When samples had nearly ideal Curie-Weiss behavior over entire temperature or at relative high temperatures (>100K), a linear least-squares method was used to get the effective magnetic moment μ_{eff} and the Weiss constant θ. If the data had a nonlinear behavior over the entire temperature range on the Curie-Weiss plot, a nonlinear least-squares program [62] was employed to calculate the parameters mentioned above, as well as the temperature-independent term χ_0, which was the major contribution to the nonlinear behavior. The magnetic data are represented under each compound on which the measurements were carried out.

RESULTS

6-18 Type

In the last 30 years or so, five distinctive 6-18 structure types have been found in the zirconium as well as niobium halide systems. They all contain isolated $Zr_6X_{18}(Z)$ or Nb_6X_{18} cluster units. Among them, $Li_6Zr_6Cl_{18}H$,[63] $Rb_5Zr_6Cl_{18}B$,[31] and $K_4Nb_6Cl_{18}$ [3] can be classified as containing simple alkali metals as countercations and having relative large cation to cluster ratios. $K_2Zr_7Cl_{18}H$ [44] and $CsLuNb_6Cl_{18}$,[64] on the other hand, incorporate an additional polycation M′ to form so called double salt cluster phases expressed as $(K_2ZrCl_6)Zr_6Cl_{12}H$ and $(CsLuCl_6)Nb_6Cl_{12}$. The recent explorations in the zirconium bromide systems have contributed two more structure types to the 6-18 family. The new compound $K_4Zr_6Br_{18}C$ can be classified as having simple alkali metal as countercations. Although the second one, $K_8Zr_6Br_{20}B$, contains only alkali metal as countercations, it distinguishes itself as a representative of a new 6-18 type by forming a novel $[K_4Br]^{3+}$ polycation.

This section will focus on the crystal structures of these two 6-18 bromide phases. The structural relationship of $K_4Zr_6Br_{18}C$ to two chloride phases, $Rb_5Zr_6Cl_{18}B$ and $Rb_4Zr_6Cl_{18}C$ [63] ($K_4Nb_6Cl_{18}$ type), will be discussed. A magnetic study on a series of $(K_{4-x}Br)_2Zr_6Br_{18}B$ compounds will be reported as well.

$K_4Zr_6Br_{18}C$

Synthesis: This phase was originally found in the reaction loaded as $K_2Zr_6Br_{10}C$ and carried out at 820°C for four weeks, aiming at a more reduced hypothetical cluster phase. Dark purple colored needles were obtained in this reaction. Its Guinier powder pattern did not look like that of any known cluster phase, indicating that a new structure type might have been uncovered. After its crystal structure was characterized, a stoichiometric reaction was carried out and a >90% yield was realized therein. The same structure type could also form with Fe as the interstitial. The replacement of K with Na yielded an unknown phase A.

Single Crystal Study: One of the needle-like crystals found in the reaction loaded as $K_2Zr_6Br_{10}C$ was employed to characterize its single crystal structure. Data collection was performed on an ENRAF NONIUS CAD4 diffractometer. The 25 reflections found in random search could be indexed only in a triclinic cell. Therefore, a hemisphere of data was collected with an ω-θ scan mode which was chosen according to the peak profiles.

Data preparation involved the Lorentz and polarization corrections and an empirical absorption correction using three averaged ψ-scan measurements. Between the two possible space groups, $P\bar{1}$ was chosen based on the statistic analysis of the reflection intensities. Its correctness was later proven by the successful refinement. After the weak reflections ($I<3\sigma$) were rejected, all the observed data were averaged in the $\bar{1}$ point group with R_{ave}=3.1%. Other important data collection parameters and data processing results are listed in Table 2. An initial model was calculated by the direct methods provided by the

Table 2. Crystal data for $K_4Zr_6Br_{18}C$

space group, Z	$P\bar{1}$ (no. 2), 1
cell parameters[a]	
a (Å)	10.114(2)
b	10.283(3)
c	10.374(3)
α (deg.)	118.54(2)
β	99.98(2)
γ	104.08(2)
V (Å^3)	864.5(3)
crystal dimens. (mm)	0.03 x 0.05 x 0.32
octants measured	h, ±k, ±l
2θ (max.) deg.	55
reflections	
observed (I/σ(I)>3.0)	1603
indep.	1511
abs. coeff. (Mo Kα, cm^{-1})	228.08
transm. coeff. range	0.59-1.00
R_{ave}, % (obs.)	3.1
no. variables	129
sec. extinct. coeff.	1.1(3) x 10^{-6}
R, %	5.1
R_w, %	4.7

[a] Guinier data

SHELXS-86 program package. All Zr, Br as well as interstitial C atom positions could be located. Two K peaks were found in the difference Fourier map after the isotropic refinements were carried out for all Zr and Br positions. Isotropic refinements for all the heavy atoms converged at R=8.1% and R_w=7.9%. The anisotropic refinements went smoothly and converged at R=5.1% and R_w=4.7%. After the secondary extinction coefficient was refined, the final difference Fourier map was calculated where the largest peak was 1.6 e/Å^3, 1.75 Å away from Br1. The occupancies of the K positions were fixed at unity in the final refinement as they did not differ from the full occupancy by 1σ when refined. According to the refinement, the empirical formula of this phase is $K_4Zr_6Br_{18}C$, which is comparable to the chloride phase $Rb_4Zr_6Cl_{18}C$, yet different in the cell dimensions and lattice symmetry. The refined atom positions and anisotropic thermal parameters are compiled in Table 3. According to the structural information obtained from the carbide, the Guinier powder pattern of $K_4Zr_6Br_{18}Fe$ could be indexed and its lattice constants refined as a=10.178(2) Å, b=10.358(3) Å, c=10.454(3) Å, α=118.40(2)°, β=100.43(2)°, γ=103.54(2)°, and V=885.7(3) Å^3.

<u>Structure Description:</u> Similar to all the known 6-18 cluster phases, $K_4Zr_6Br_{18}C$ contains isolated $[Zr_6CBr^i_{12}]Br^a_6$ cluster units. As shown in Figure 2, there is only one cluster in the unit cell and the isolated $[Zr_6Br^i_{12}C]Br^a_6$ cluster units are surrounded by K^+ cations. Apparently, these K^+ cations not only provide electrons to form the optimal 14e clusters but also reduce the repulsions

Table 3. Positional and thermal parameters for $K_4Zr_6Br_{18}C$

Atom	Psn.	x	y	z	B_{eq}(Å^2)
Zr1	2(i)	0.3547(3)	0.2612(3)	0.9550(3)	1.8(1)
Zr2	2(i)	0.3503(3)	0.4440(3)	0.7699(3)	1.75(9)
Zr3	2(i)	0.3611(3)	0.6258(3)	0.1323(3)	1.6(1)
Br1	2(i)	0.1723(3)	0.5786(4)	0.8876(4)	2.5(1)
Br2	2(i)	0.4929(3)	0.0816(4)	0.7985(4)	2.4(1)
Br3	2(i)	0.1752(3)	0.3690(4)	0.0989(4)	2.4(1)
Br4	2(i)	0.5033(3)	0.2911(4)	0.2133(4)	2.5(1)
Br5	2(i)	0.4864(3)	0.2905(4)	0.5825(3)	2.6(1)
Br6	2(i)	0.1636(3)	0.1577(4)	0.6812(3)	2.4(1)
Br7	2(i)	0.1754(3)	0.9696(4)	0.8988(4)	3.0(1)
Br8	2(i)	0.1647(3)	0.3776(4)	0.4913(4)	3.1(1)
Br9	2(i)	0.1972(3)	0.7787(4)	0.2915(4)	3.1(1)
K1	2(i)	0.1880(8)	0.724(1)	0.5636(9)	4.3(3)
K2	2(i)	0.1546(9)	0.039(1)	0.2285(9)	4.7(3)
C	1(e)	1/2	1/2	0	4(1)

[a] U x 10^3

U_{11}[a]	U_{22}	U_{33}	U_{12}	U_{13}	U_{23}
22(2)	20(2)	23(2)	5(1)	6(1)	11(2)
20(2)	22(2)	21(2)	7(1)	5(1)	10(1)
20(2)	20(2)	21(2)	10(1)	8(1)	9(1)
25(2)	37(2)	32(2)	17(2)	8(2)	17(2)
30(2)	19(2)	38(2)	10(2)	13(2)	11(2)
28(2)	31(2)	39(2)	12(2)	18(2)	19(2)
32(2)	32(2)	33(2)	5(2)	5(2)	22(2)
30(2)	42(2)	20(2)	17(2)	9(2)	12(2)
25(2)	26(2)	27(2)	2(2)	2(2)	11(2)
38(2)	27(2)	43(2)	4(2)	14(2)	20(2)
36(2)	42(2)	29(2)	11(2)	-3(2)	17(2)
41(2)	40(2)	46(2)	25(2)	27(2)	21(2)
54(5)	54(6)	54(5)	20(4)	23(4)	28(5)
83(6)	60(6)	55(5)	48(5)	32(5)	34(5)
50(10)					

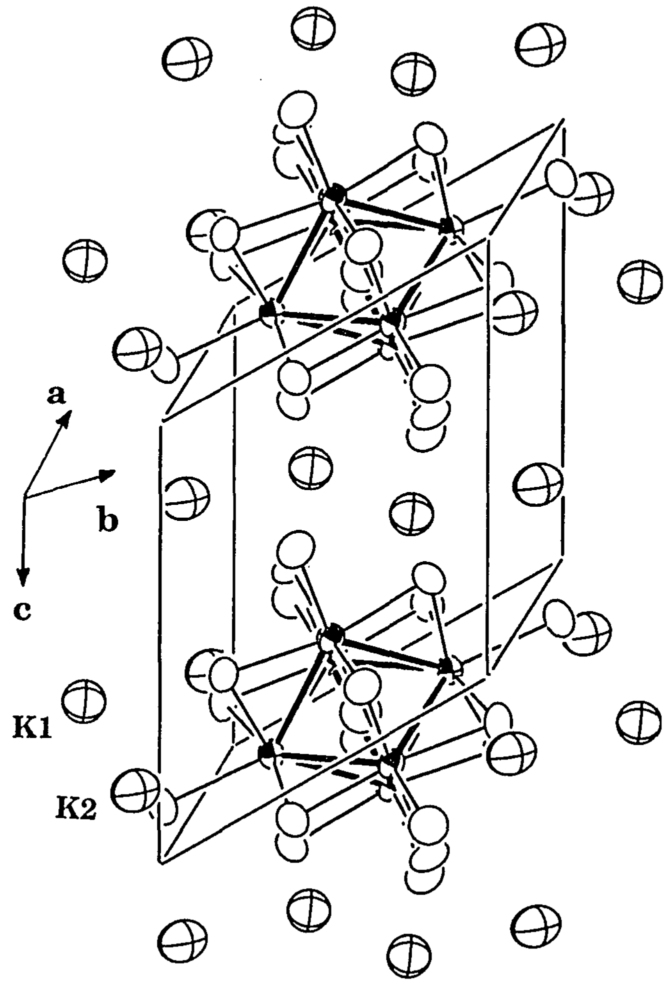

Figure 2. The unit cell view of $K_4Zr_6Br_{18}C$, showing the isolated clusters ina sea of K^+ countercations (80% probability)

among Cl^- atoms that sheath zirconium octahedra. Although the lattice has triclinic symmetry, the cluster itself (Figure 3) has a rather regular arrangement as indicated by the bond distances and angles in Table 4. In other words, the low lattice symmetry is probably caused by the irregular stacking of cluster units and/or the non-close- packed layers in the lattice. In $K_4Zr_6Br_{18}C$, the sublattice of Br^- anions lies in layers parallel to the bc plane. Figure 4 gives the layer view at x=0.5 containing Br2, Br4, Br5, and interstitial C atoms. As seen, even though the Br atoms around the interstitials remain close packed, the long range symmetric arrangement is lost. It is even more so in the layer at $x=0.17\pm0.02$ (Figure 5), which is composed of Br and K atoms. As noted, the intrusion of the smaller K^+ cations into the Br layer destroys the long range as well as the short range close packing feature of the Br atoms. One may notice in Figures 6 and 7 that the cluster layers in $K_4Zr_6Br_{18}C$, while parallel to the bc plane, slide with respect to each other, giving a β and γ angles 99.98(2)° and 104.08(2)°, respectively. This explains why the lattice has such low symmetry while the individual cluster unit exhibits a fairly regular octahedral arrangement.

The structure of $K_4Zr_6Br_{18}C$ can be considered new as it has unique cell dimensions and lattice symmetry. Nonetheless, this triclinic cell can be transformed into a pseudo C-centered monoclinic cell which is related to the structures of $Rb_4Zr_6Cl_{18}C$ [63] and $Rb_5Zr_6Cl_{18}B$.[31] The transformation is elaborated in Figure 8 and Table 5. These three 6-18 phases form a series in terms of the lattice symmetries. Among them, $Rb_5Zr_6Cl_{18}B$ has the highest lattice symmetry.

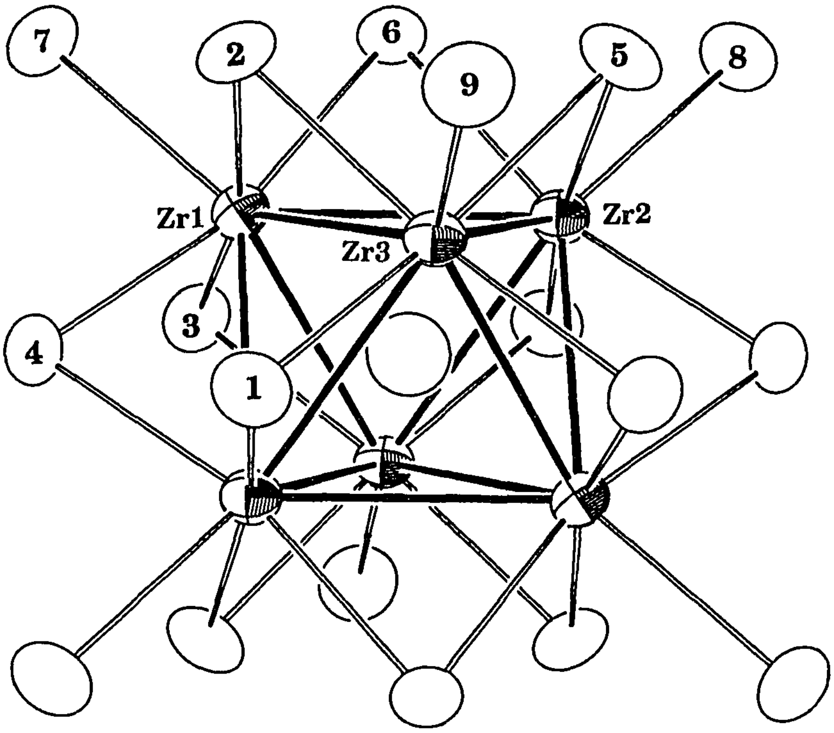

Figure 3. The isolated $[Zr_6CBr^i_{12}]Br^a_6$ cluster unit in $K_4Zr_6Br_{18}C$ with a crystallographic C_i point symmetry in the space group $P\bar{1}$. It actually has a very regular octahedral arrangement and exhibits an O_h symmetry. The picture is drawn with 70% probability and the a axis vertical

Table 4. Important bond distances (Å) and angles (°) in $K_4Zr_6Br_{18}C$

d(Zr-Zr)			d(K-Br)		
Zr1-Zr2	x2[a]	3.258(4)	K1-Br9	x1	3.144(8)
	x2	3.269(4)	-Br8	x1	3.203(8)
Zr1-Zr3	x2	3.270(4)	-Br7	x1	3.226(8)
	x2	3.273(4)	-Br8	x1	3.325(8)
Zr2-Zr3	x2	3.269(4)	-Br2	x1	3.506(8)
	x2	3.270(4)	-Br4	x1	3.632(8)
$\bar{d}$		3.270	$\bar{d}$		3.339
			K2-Br9	x1	3
.151(8)					
d(Zr-C)			-Br8	x1	3.196(8)
Zr1-C	x1	2.306(3)	-Br7	x1	3.200(8)
Zr2-C	x1	2.309(3)	-Br7	x1	3.332(8)
Zr3-C	x1	2.321(3)	$\bar{d}$		3.220
$\bar{d}$		2.312	d(Br-Br)[b]		
d(Zr-Br^i)			Br1-Br8	x1	3.587(5)
Zr1-Br2	x1	2.679(4)	-Br9	x1	3.606(6)
-Br3	x1	2.663(4)	Br3-Br7	x1	3.611(5)
-Br4	x1	2.669(4)	Br6-Br7	x1	3.612(4)
-Br6	x1	2.673(4)	Br3-Br9	x1	3.625(5)
Zr2-Br1	x1	2.647(4)	Br4-Br7	x1	3.630(5)
-Br4	x1	2.671(4)			
-Br5	x1	2.687(4)			
-Br6	x1	2.680(4)	Zr2-Zr1-Zr2	x1	90.1(2)
Zr3-Br1	x1	2.650(4)	Zr2-Zr1-Zr3	x1	59.98(8)
-Br2	x1	2.675(4)	Zr3-Zr1-Zr3	x1	90.4(1)
-Br3	x1	2.667(4)	Zr1-Zr2-Zr3	x1	60.03(9)
-Br5	x1	2.686(4)	Zr3-Zr2-Zr3	x1	90.3(1)
$\bar{d}$		2.670	Zr1-Zr3-Zr1	x1	89.6(1)
d(Zr-Br^a)			Br2-Zr1-Br3	x1	165.2(1)
Zr1-Br7	x1	2.817(4)	Br4-Zr1-Br6	x1	165.0(1)
Zr2-Br8	x1	2.820(5)	Br1-Zr2-Br5	x1	165.4(1)
Zr3-Br9	x1	2.772(5)	Br4-Zr2-Br6	x1	165.4(1)
$\bar{d}$		2.803	Br1-Zr3-Br5	x1	165.4(1)
			Br2-Zr3-Br3	x1	165.9(1)

---

[a] Number of times the distances and angles occur per atom

[b] d(Br-Br) < 3.630 Å

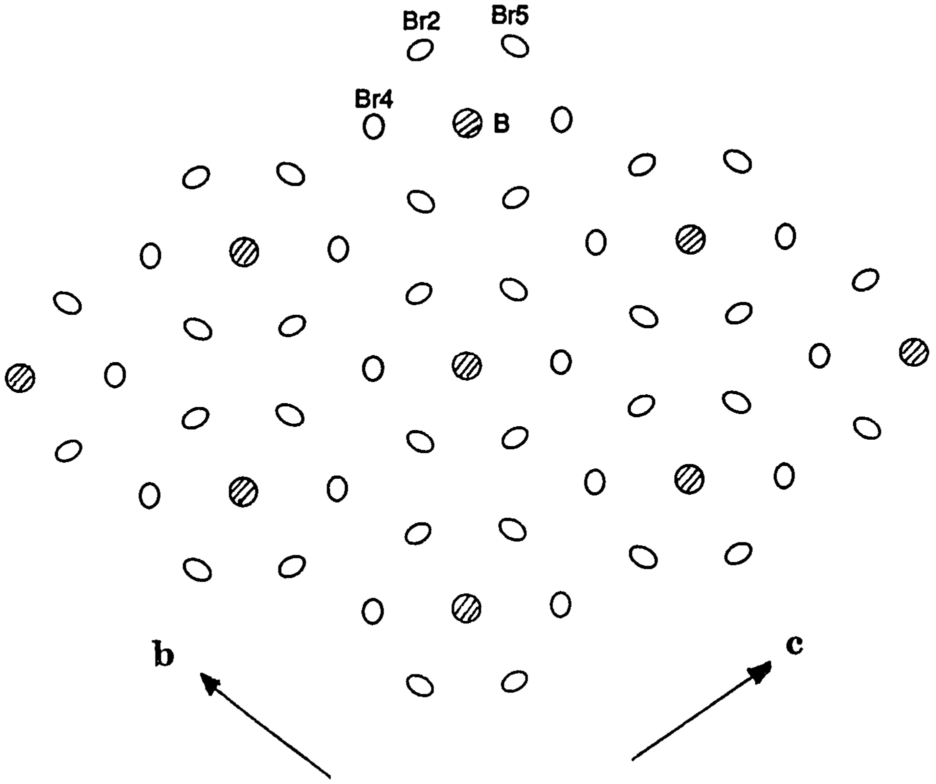

Figure 4. The projection of B-Br layer at x=0.5, indicating that the Br atoms around B or related to the cluster unit remain close packed, yet the long range symmetry is not existed (90% probability)

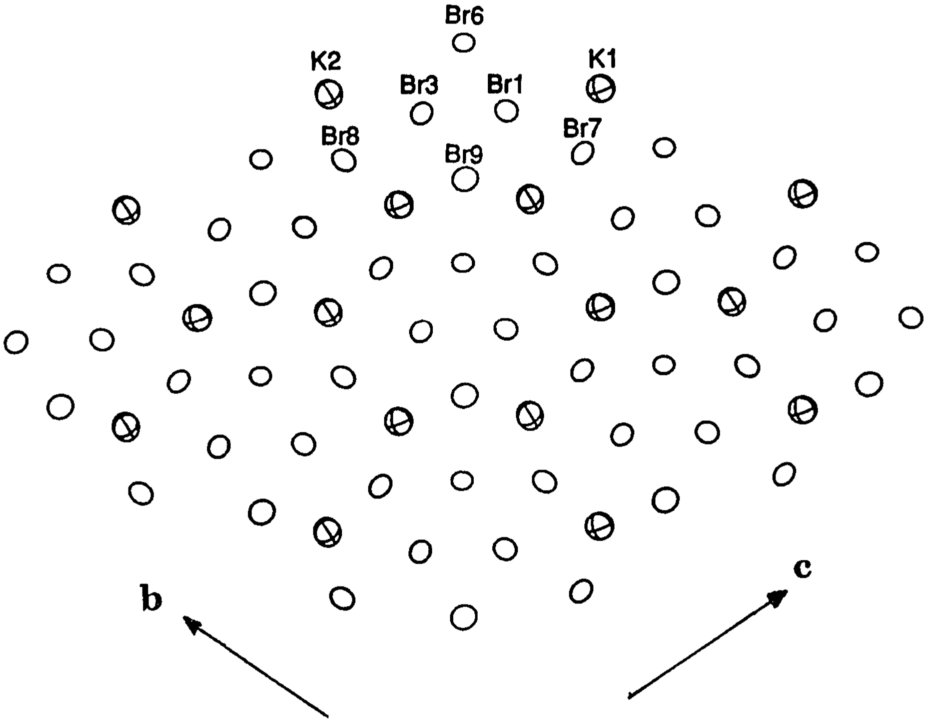

Figure 5. The projection of K-Br layer at x=0.17±0.02, showing that the close packing feature is destroyed by the inclusion of the K^+ into the Br^- layer (90% probability)

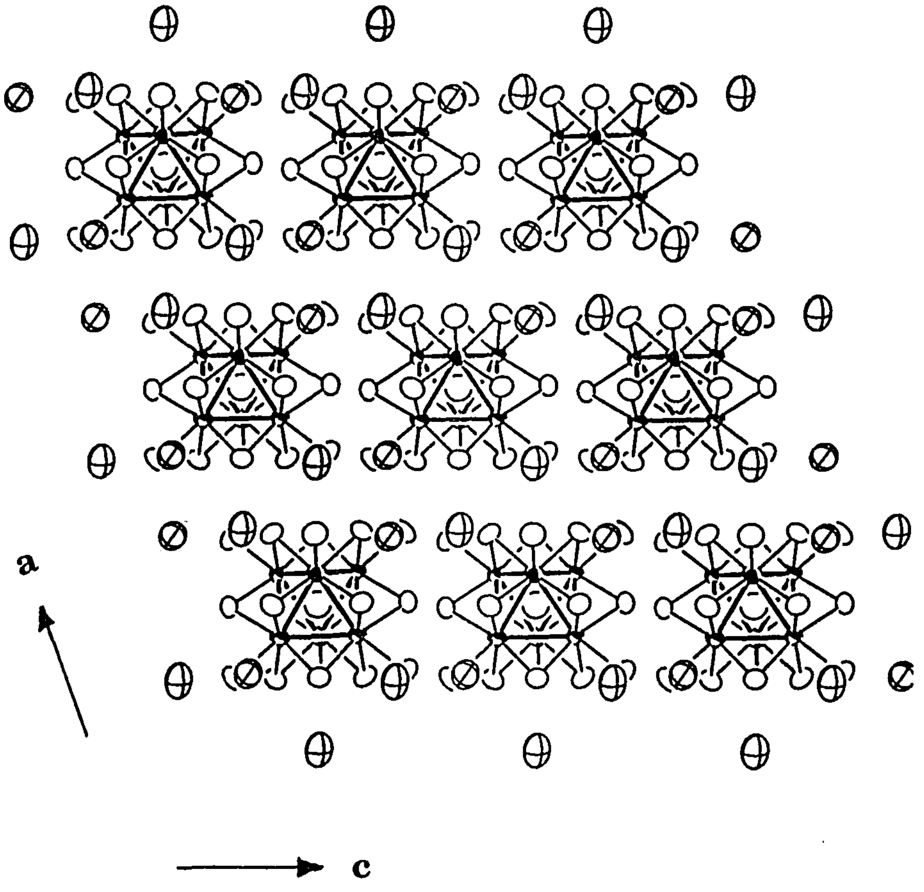

Figure 6. The projection along [010] direction, showing that the cluster layers shift along the c direction, resulting in a β of 99.98(2)° and a triclinic lattice (90% probability)

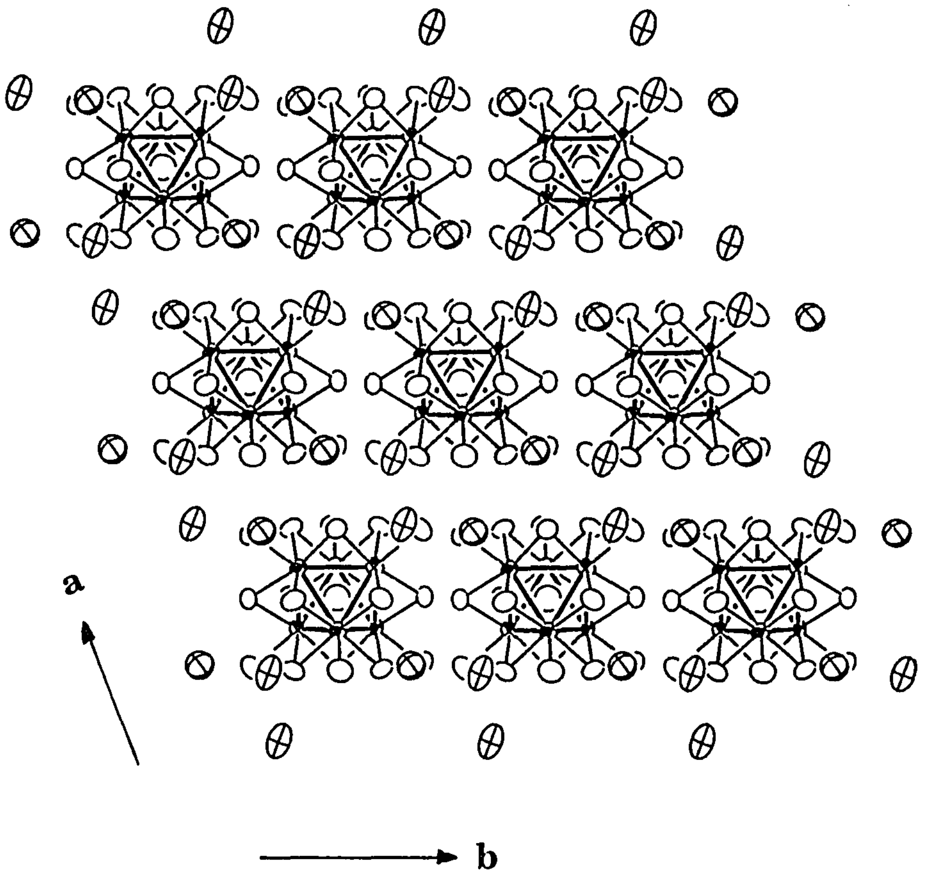

Figure 7. The projection along [001] direction, showing that the cluster layers are parallel to the bc plane, and the K atoms are in the Br layers near the gaps. The cluster layers shift along the b direction, yielding a γ of 104.08(2)° (90% robability)

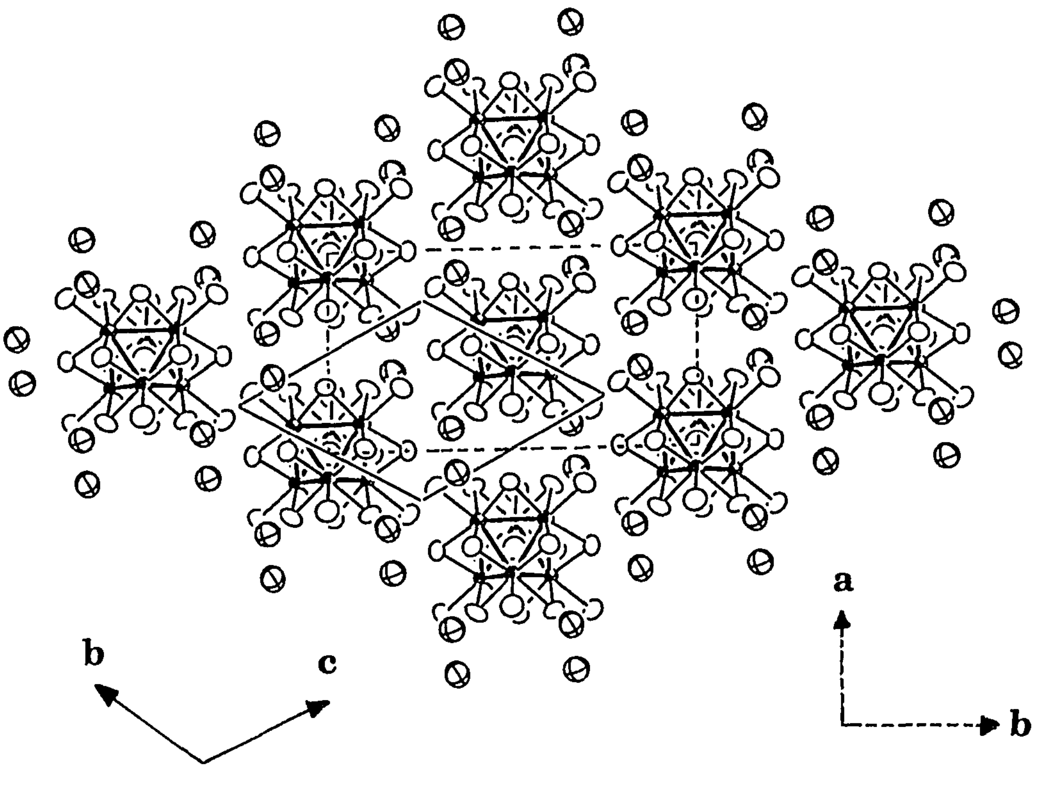

Figure 8. The projection along [100] direction, showing the bc plane in the triclinic cell and the ab plane in the pseudo C-centered monoclinic cell (dotted lines) with γ=92.27(3)° (90% probability)

Table 5. The Guinier cell constants for the three structurally related 6-18 phases.

	$Rb_5Zr_6Cl_{18}B$	$Rb_4Zr_6Cl_{18}C$	$K_4Zr_6Br_{18}C$
space group	Pman	C2/m	"$C\bar{1}$" [a]
a (Å)	10.941(4)	10.460(4)	10.114(2)
b	17.769(4)	17.239(4)	17.757(5)
c	9.078(5)	9.721(4)	10.556(3)
α (°)	90.00	90.00	90.58(2)
β	90.00	115.05(3)	114.04(3)
γ	90.00	90.00	92.27(3)
V (Å^3)	1760(1)	1588.0(9)	1729(2)

[a] The pseudo C-centered monoclinic cell is transformed from the triclinic cell by the matrix

$$\begin{pmatrix} 1 & 0 & 0 \\ 0 & 1 & -1 \\ 0 & 1 & 1 \end{pmatrix}$$

It contains close packed atom layers, and the cluster units form two dimensional layers as well. These cluster layers are stacked in ...AAA..., and the cluster units are packed right on top of each other, giving the lattice orthorhombic symmetry. In $Rb_4Zr_6Cl_{18}C$, however, the long range close packing within the anion layers is lost. Besides, the clusters are not packed directly on top of each other, rather glide along the a direction, forming a monoclinic lattice with a β of 115°. As mentioned earlier, a severe distortion is found in $K_4Zr_6Br_{18}C$, for the shift of the cluster layer is in two directions resulting in a triclinic lattice. The driving force for the distortion in $Rb_4Zr_6Cl_{18}C$ is to create the required cation sites and to maximize the interactions between Rb^+ and Cl^-. Doing so, the repulsions among the Cl^- anions are reduced, which results in a more stable lattice. It is even more so in $K_4Zr_6Br_{18}C$. The ease in preparing $K_4Zr_6Br_{18}C$ suggests a much more stable lattice.

The distortion in $K_4Zr_6Br_{18}C$ creates two different cation sites. The environment of K1 is very similar to that of Rb in $Rb_4Zr_6Cl_{18}C$. As indicated in Figure 9, K1 occupies a distorted tetrahedral site created by four adjacent cluster units among which three are from the same cluster layer and form the basal plane, and the one from the adjacent layer fills the apical position to complete the tetrahedral polyhedron. Each cluster in the basal plane offers one Br^a and one Br^i to K1, and the apical one only furnishes one Br^a. The basicity of halide ligands have the order of $X^a > X^{a-a} > X^i > X^{a-i}$.[18] The interaction between countercations and halide ligands also follow the same trend. As a result, the

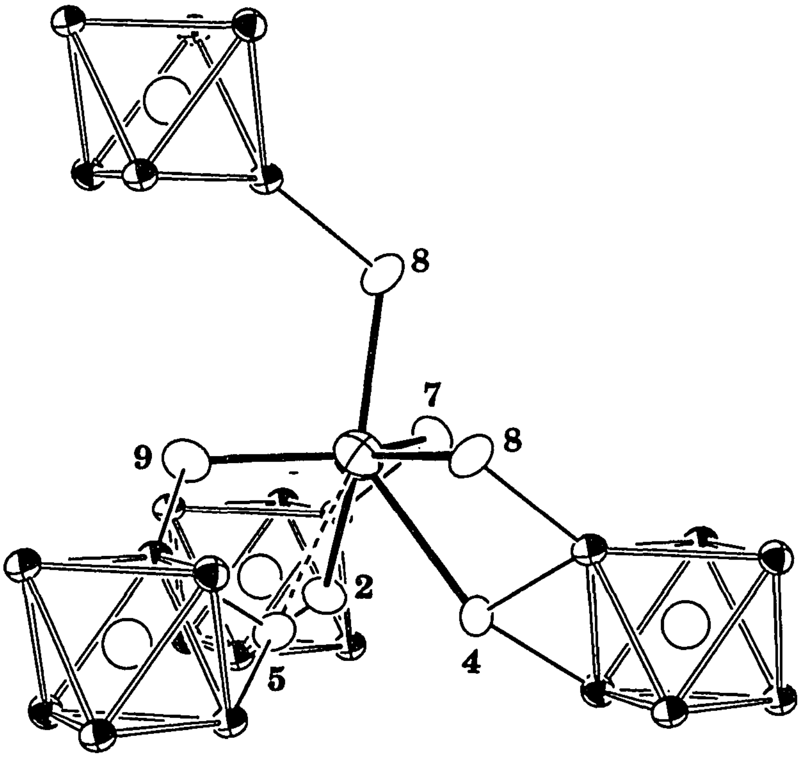

Figure 9. The distorted tetrahedral environment around K1 in $K_4Zr_6Br_{18}C$. The three clusters in the basal plane are from the same layer, and the apical one is from the adjacent layer. K1 is within the bromine layer, and has three Br^a as neighbor. Br5 is connected by a dotted line as it is at a longer distance, 3.861 Å (70% probability)

terminal X^a usually lies closer to the countercation than X^i does, or the M^{n+}-X^a separation is usually shorter than that of M^{n+}-X^i, where M represents a countercation. The same phenomenon has been seen in $K_4Zr_6Br_{18}C$ as well. For instance, the average K1-Br^a distance is 3.224 Å, 0.442 Å shorter than that of K1-Br^i, 3.666 Å. If one only considers the six Br atoms at the distances shorter than 3.75 Å, the average K1-Br distance is 3.339 Å, which is in a good agreement with the summation of the corresponding crystal radii (Br^-(VI), 1.82 Å; K^+(VI), 1.52 Å).

K2 is also surrounded by four tetrahedrally arranged cluster units (Figure 10), however, it has only five Br atoms at the distances smaller than 3.75 Å. Compared with K1 which is within the anion layer formed by Br1, 3, 6, 7, 8, and 9, K2 is slightly above the same anion layer, therefore it is farther from the Br^i atoms connected to the clusters in the basal plane of the tetrahedron. As a result, it has only four Br^a atoms in its first bonding sphere with the average distance as 3.220 Å, which is about 0.1 Å shorter than the summation of the crystal radii of 4-coordinate K^+ (1.51 Å) and Br^- (1.82 Å). There are four Br^i atoms as its secondary neighbors at the distances of 3.723-3.990 Å.

The average distance between Zr and Br^a is 2.803 Å, 0.133 Å longer than that between Zr and Br^i, 2.670Å. Among the Zr-Br^i distances, those between Zr and Br1 (2.647(4) Å and 2.650(4) Å) are slightly shorter than the rest of Zr-Br^i distances, 2.663(4) Å–2.687(4) Å. This can be attributed to the fact that Br1 does not have any K^+ as its neighbors, or has a lower coordination number.

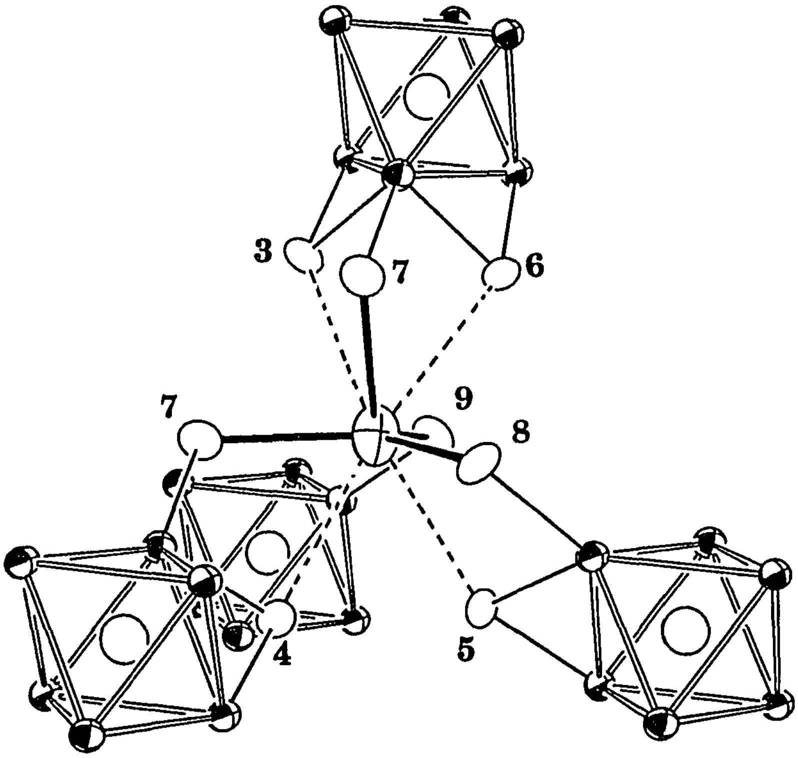

Figure 10. The distorted tetrahedral environment around K2 in $K_4Zr_6Br_{18}C$. The clusters in the basal plane of the tetrahedron are in the same layer and the apical one is from the adjacent layer. K2 is slightly above the anion layer defined by Br7, 8, and 9. It has five Br atoms at the distances < 3.75 Å. The Br atoms at longer distances are connected by the dotted lines (70% probability)

Owing to the fact that terminal Br9 has only one K^+ in its adjacent area and Br7 and Br8 have 2 K^+ as their neighbors, the Zr-Br9 distance 2.772(5) Å is shorter than those of Zr-Br7 and Zr-Br8, 2.817(4) Å and 2.820(5) Å, respectively. The cluster unit $[Zr_6CBr^i_{12}]Br^a_6$ possesses an inversion symmetry (C_i). The cluster core itself, however, has a very regular octahedral arrangement, as the Zr-Zr distances range from 3.258(4) Å to 3.279(4) Å, within 3.7σ. The average Zr-Zr distance is 3.270 Å, 0.042 Å longer than that in $Rb_4Zr_6Cl_{18}C$, 3.2283 Å. The average Zr-C distance is 2.312 Å, 0.025 Å longer than the one in the corresponding chloride. Since both $K_4Zr_6Br_{18}C$ and $Rb_4Zr_6Cl_{18}C$ are 14 e^- cluster phases, the differences in Zr-Zr and Zr-C distances are mainly caused by the size difference between Cl^- and Br^-, which are about 1.67 Å and 1.82 Å, respectively, or because of the so called matrix effect.[18] The very short Br-Br distances 3.587(5) Å–3.630(5) Å (Table 4) are one of the evidences of matrix effect.

In the Zr-Cl system, when the interstitial carbon was replaced by B as from $Rb_4Zr_6Cl_{18}C$ to $Rb_5Zr_6Cl_{18}B$, the lattice symmetry, the number of countercations, and some other structure features varied only to a small degree so that they still had the similar framework. The situation in the bromide system is totally different, as the replacement of carbon by boron results in a new phase $(K_4Br)_2Zr_6Br_{18}B$ with a novel structural fragment, $[K_4Br]^{3+}$ polycation, in a face-centered cubic lattice.

$(K_4Br)_2Zr_6Br_{18}B$

Synthesis: Similar to $K_4Zr_6Br_{18}C$, $(K_4Br)_2Zr_6Br_{18}B$ was first observed in the reaction loaded as KZr_6Br_9B, targeting a more reduced hypothetical cluster phase. This reaction was carried out at 850°C for three weeks. Based on the powder pattern, the major product was the 6-14 phase with a Nb_6Cl_{14} structure type.[6] In addition, an unknown phase with 10-15% yield was also observed. The same new phase was also observed in reactions loaded as $K_2Zr_6Br_{10}B$ and $K_4Zr_6Br_{15}B$, and the yields were about 25% and 50%, respectively. The Guinier powder pattern of the new phase contained fewer lines than most of the cluster phases, indicating a possible high lattice symmetry. It turned out that this new phase has a face-centered-cubic lattice. After the crystal structure of this cubic phase was characterized, a stoichiometric reaction was run, and about a 90% yield was achieved. Several more new compounds with the same structure type were prepared with Na or Rb as countercations, and H, Be or Mn as interstitials. This structure type, however, does not form with Cs^+ as the countercation. When Na and Be were loaded in the same reaction, a similar, yet different powder pattern was observed. The splitting of some of the lines observed for the cubic phase as well as some weak extra lines indicated a lower lattice symmetry.

Single Crystal Studies: As mentioned before, 10-15% of the new phase was found in the reaction loaded as KZr_6Br_9B. Out of the entire reaction, one needle-like crystal was found. Its identity, however, was not very clear at that moment. Therefore, oscillation and Weissenberg photos were taken to gain some crystallographic information. The axis calculated from the oscillation film was 11.6 Å, and the other two axes were calculated as 11.7 Å and 16.6 Å with 90° angle according to the zero and first layer Weissenberg photos. Furthermore, the body-centering extinction condition (h+k+l=2n+1) was observed as well. This result indicated that the crystal was indeed of the unknown phase, for the cell parameters of the 6-14 phase found in the same reaction were refined in a primitive orthorhombic cell with a=14.777(1) Å, b=13.3016(9) Å, and c=12.0602(7) Å. However, the lattice symmetry of the new phase still seemed lower than that reflected by the powder pattern. In other words, this body-centered orthorhombic cell could be a nonstandard setting of a cell with a higher lattice symmetry. Since the a, b, and c axes of this body-centered tetragonal cell has the relation of $a = c / \sqrt{2}$, this tetragonal cell actually has a face-centered cubic symmetry.

Data collection was performed on a RIGAKU AFC6R diffractometer. The 25 reflections located in program SEARCH could be indexed in a primitive rhombohedral cell with a=11.41 Å. The cubic symmetry was recognized as the angle was 60°, and the cell was transformed to the standard cubic setting (a=16.146(2) Å) with cell reduction program DELAUNAY. As noticed, the oscillation axis happened to be the rhombohedral axis, along which the crystal grew. This explains why the shape of the crystal is needle-like and the real lattice symmetry was not reflected directly on the Weissenberg photos. One octant of data was collected with the F-centering condition applied. A ψ-scan measurement was performed on one reflection, the only one with moderate intensity and a suitable ϕ angle.

The Laue class $m\bar{3}m$ was determined by the Program LAUE. Data processing involved Lorentz and polarization correction, and an empirical absorption correction using ψ-scan measurements. The other important data collection parameters can be found in Table 6. The face-centering extinction conditions, h+k, h+l, k+l=2n+1 were observed in the data. There were three possible space groups in the Laue class $m\bar{3}m$ that fulfill the observed extinctions. Among them, the one with the highest symmetry, $Fm\bar{3}m$, was first used to get the initial model, and the correctness was proven by the success in the structural refinements.

Program SHELXS-86 provided a solution; however, the peak assignment was somewhat ambiguous, as the atomic number of Br is not very different from that of Zr. A rough ORTEP picture was drawn with the first several peaks. Zr and Br positions could be clearly recognized by their bonding features. Atoms forming octahedra were assigned as Zr, while those attached to the octahedra were assigned as Br. Furthermore, the peak in the center of the octahedron was assumed to be the interstitial boron. At this stage, the formula was $Zr_6Br_{18}B$. It seemed that the K peaks should be the only leftovers. Two peaks showed up in the difference Fourier map after the isotropic refinements were carried out for Zr and Br positions. The first peak was not connected to any refined atoms and the height was about 30 $e^-/Å^3$, which was too high for a K position. With an

Table 6. Crystal data for $(K_4Br)_2Zr_6Br_{18}B$ and $(K_{3.42(6)}Br)_2Zr_6Br_{18}B$

	$(K_4Br)_2Zr_6Br_{18}B$	$(K_{3.42(6)}Br)_2Zr_6Br_{18}B$
space group, Z	$Fm\bar{3}m$, 4	$Fm\bar{3}m$, 4
cell parameters[a]		
a (Å)	16.191(2)	16.2025(7)
V (Å^3)	4244(2)	4253.5(5)
crystal dimens. (mm)	0.03 x 0.03 x 0.28	0.08 x 0.14 x 0.23
octant measured	h, k, l	h, k, l
2θ (max.), deg.	50	50
reflections		
measured	1363	4157
observed (I/σ(I)>3)	616	479
indep.	160	135
abs. coeff. (Mo, Kα, cm^{-1})	208.47	208.02
transm. coeff. range	0.93-1.00	0.30-1.00
R_{ave}, % (obs.)	5.6	5.1
no. variables	16	18
sec. extinct. coeff.	0	8(3) x 10^{-9}
R, %	3.2	3.9
R_w, %	1.6	3.0

[a] Guinier cell constants

open mind, this position was filled with Br. According to the distances to the neighboring Br atoms, the next peak was assigned as a K position. It turned out that the isolated Br^- and K^+ countercations form a polycation $[K_4Br]^{3+}$.

The isotropic refinement for all Zr, Br, and K positions converged at R=9.1% and R_w=4.7%. The anisotropic refinements were carried out very smoothly and converged at R=4.7% and R_w=2.2%. The thermal parameter of boron, however, was negative. This could be caused by the insufficient absorption correction (one ψ-scan) for a very anisotropic (needle-like) crystal. Therefore, a cylindric correction provided by program PABSN[66] was performed on the data. The least-square refinement with the data thus prepared gave the temperature factor of interstitial boron a positive value and converged with much smaller residuals, R=3.2% and R_w=1.6%. After the secondary extinction coefficient and isotropic thermal parameter of boron were refined, the occupancy of K^+ refined to 100(1)%, and was fixed at unity in the final refinement. The positional and anisotropic thermal parameters are compiled in Table 7. Based on the refinement, this phase has the empirical formula $K_8Zr_6Br_{20}B$, a 15e cluster phase. Using the refinement results, the lattice constants of the compounds with the same structure type were refined from Guinier data and reported in Table 8.

The single crystal structure refinements were also performed on a crystal from the reaction loaded as $K_4Zr_6Br_{15}B$. Its data collection conditions and refinement results are listed together with the corresponding information for the

Table 7. Positional and thermal parameters for $(K_4Br)_2Zr_6Br_{18}B$ and $(K_{3.42(6)}Br)_2Zr_6Br_{18}B$

Atom	Psn.	x	y	z	B_{eq}(Å^2)
$\underline{(K_4Br)_2Zr_6Br_{18}B}$					
Zr	24(e)	0.1437(1)	0	0	1.47(6)
Br1	48(h)	0	0.16629(7)	y	2.39(4)
Br2	24(e)	0.3190(1)	0	0	3.16(7)
Br3	8(c)	1/4	1/4	1/4	3.319(1)
K[b]	32(f)	0.3591(2)	x	x	5.379(2)
B	4(a)	0	0	0	0.3(10)
$\underline{(K_{3.5}Br)_2Zr_6Br_{18}B}$					
Zr	24(e)	0.1441(2)	0	0	1.88(8)
Br1	48(h)	0	0.1657(1)	y	2.77(6)
Br2	24(e)	0.3183(2)	0	0	3.30(9)
Br3	8(c)	1/4	1/4	1/4	4.100(2)
K[c]	32(f)	0.3602(3)	x	x	4.971(3)
B	4(a)	0	0	0	1(2)

[a] U x 10^3

[b] 100(1)% occupied

[c] 86(1)% occupied

U_{11}^{a}	U_{22}	U_{33}	U_{12}	U_{13}	U_{23}
16(1)	19.9(8)	U_{22}	0	0	0
45(1)	23.2(5)	U_{22}	0	0	-8.9(8)
15(1)	53(1)	U_{22}	0	0	0
42.03(2)	U_{11}	U_{11}	0	0	0
68.12(2)	U_{11}	U_{11}	-15(2)	U_{12}	U_{12}
3(10)					
21(2)	2591)	U_{22}	0	0	0
48(2)	28.9(8)	U_{22}	0	0	-8(1)
21(2)	52(1)	U_{22}	0	0	0
51.93(2)	U_{11}	U_{11}	0	0	0
62.95(4)	U_{11}	U_{11}	-18(3)	U_{12}	U_{12}
10(20)					

Table 8. Guinier lattice constants of the compounds[a] with $(K_4Br)_2Zr_6Br_{18}B$ structure type

	a (Å)	V (Å^3)	yield
$(K_4Br)_2Zr_6Br_{18}B$[b]	16.197(1)	4248.8(9)	> 95%
$(K_4Br)_2Zr_6Br_{18}Be$	16.240(2)	4283(1)	95%
$(K_4Br)_2Zr_6Br_{18}H$	16.178(1)	4234(1)	90%
$(K_4Br)_2Zr_6Br_{18}Mn$[c]	16.320(2)	4347(1)	50%
$(Rb_4Br)_2Zr_6Br_{18}B$	16.585(2)	4562(2)	> 90%
$(Rb_4Br)_2Zr_6Br_{18}Be$	16.628(1)	4597.6(8)	> 90%
$(Rb_4Br)_2Zr_6Br_{18}Mn$[c]	16.692(3)	4651(3)	50%
$(Na_4Br)_2Zr_6Br_{18}B$	15.704(3)	3873(2)	> 95%

[a] Unless noted, the data are for the compounds from the stoichiometric reactions

[b] 10% excess Zr

[c] 20-30% excess Mn, as it is not easy to control the weight of Mn chunks

first crystal in Tables 6, 7, and 9. It turned out that the occupancy of the K^+ in this compound was 86(1)%, which yielded a 13.8(1)e cluster phase. It is very interesting to notice that the higher K content phase is from the reaction with less $K/Zr_6Br_{20}B$ in the loaded stoichiometry, while the phase containing less K was from the reaction loaded with more $K/Zr_6Br_{20}B$. It seemed that the more reduced stoichiometry (excess Zr in this case) was crucial to form the former 15e phase. The same phenomenon has been observed in the Zr-Cl system.[42,63] According to this result, several reactions were run with different K and Zr contents. Interestingly, the phase breadth was not strongly reflected in their Guinier cell parameters (Table 10), rather in their magnetic properties (see the section of magnetic results).

Structure Description: The structure of this cubic phase is composed of two fragments, isolated $\{[Zr_6Br^i_{12}B]Br^a_6\}^{-6}$ cluster units and $[K_4Br]^{3+}$ polycations. Thus, $(K_4Br)_2Zr_6Br_{18}B$ is a better way to represent its structural features. The isolated cluster units form close packed layers which stack along the body diagonal direction in ...ABCABC..., resulting in a face-centered cubic cell (Figure 11), a special case of a rhombohedral lattice. This arrangement has been previously observed in the lattice of $Li_6Zr_6Cl_{18}H$, which has a squashed rhombohedral lattice with a rhombohedral angle of 111.08°. The cation distributions, however, are very different in these two compounds. In $Li_6Zr_6Cl_{18}H$, Li^+ occupies octahedral sites created by six Cl^- atoms. In $(K_4Br)_2Zr_6Br_{18}B$, on the other hand, the $[K_4Br]^{3+}$ polycation is located in a

Table 9. Important bond distances (Å) and angles (°) in $(K_4Br)_2Zr_6Br_{18}B$ and $(K3.4Br)_2Zr_6Br_{18}B$

		$(K_4Br)_2Zr_6Br_{18}B$	$(K_{3.4}Br)_2Zr_6Br_{18}B$
Distances (Å)			
d(Zr-Zr)			
Zr-Zr	x4[a]	3.290(2)	3.302(2)
d(Zr-B)			
Zr-B	x1	2.326(2)	2.335(3)
d(Zr-Br^i)			
Zr-Br1	x4	2.717(1)	2.707(2)
d(Zr-Br^a)			
Zr-Br2	x1	2.840(3)	2.823(4)
d(K-Br)			
K-Br3	x1	3.061(5)	3.093(5)
-Br^a2	x3	3.290(4)	3.274(6)
-Br^i1	x6	3.889(1)	3.904(4)
$\bar{d}$(CN=4)		3.233	3.229
d(Br-Br)[b]			
Br1-Br1	x4	3.808(1)	3.797(2)
	x1	3.834(2)	3.863(2)
-Br2	x2	3.655(2)	3.650(3)
Zr-Zr-Zr	x2	90.00	90.00
	x4	60.00	60.00
	x1	180.00	180.00
Br2-Zr-B	x1	180.00	180.00
K-Br3-K	x4	109.47	109.47
Br^i1-Zr-Br^i1	x2	164.60(5)	165.4(1)

[a] Number of times the distances and angles occur per atom

[b] d(Br-Br) < 4.0 Å

Table 10. Guinier lattice constants of $(K_{4-x}Br)_2Zr_6Br_{18}B$[a]

Lattice Constants[b] a (Å)	V (Å^3)	μ_{eff} (μ_B)	Stoichiometry Loaded	Yield
16.191(2)	4244(2)		KZr_6Br_9B	10-15%
16.197(1)	4248.8(9)	1.77(1)	$(K_4Br)_2Zr_6Br_{18}B$, with 10% excess Zr	> 95%
16.196(1)	4244.5(9)	1.57(1)	$(K_4Br)_2Zr_6Br_{18}B$	> 90%
16.201(1)	4252.5(8)	1.1(1)	$(K_{3.75}Br)_2Zr_6Br_{18}B$	> 90%
16.209(2)	4259(2)	0.78(6)	$(K_{3.5}Br)_2Zr_6Br_{18}B$	90%
16.2025(7)	4253.5(5)		$K_4Zr_6Br_{15}B$	50%

[a] All the reactions were run at 850°C for about four weeks.

[b] Guinier cell constants.

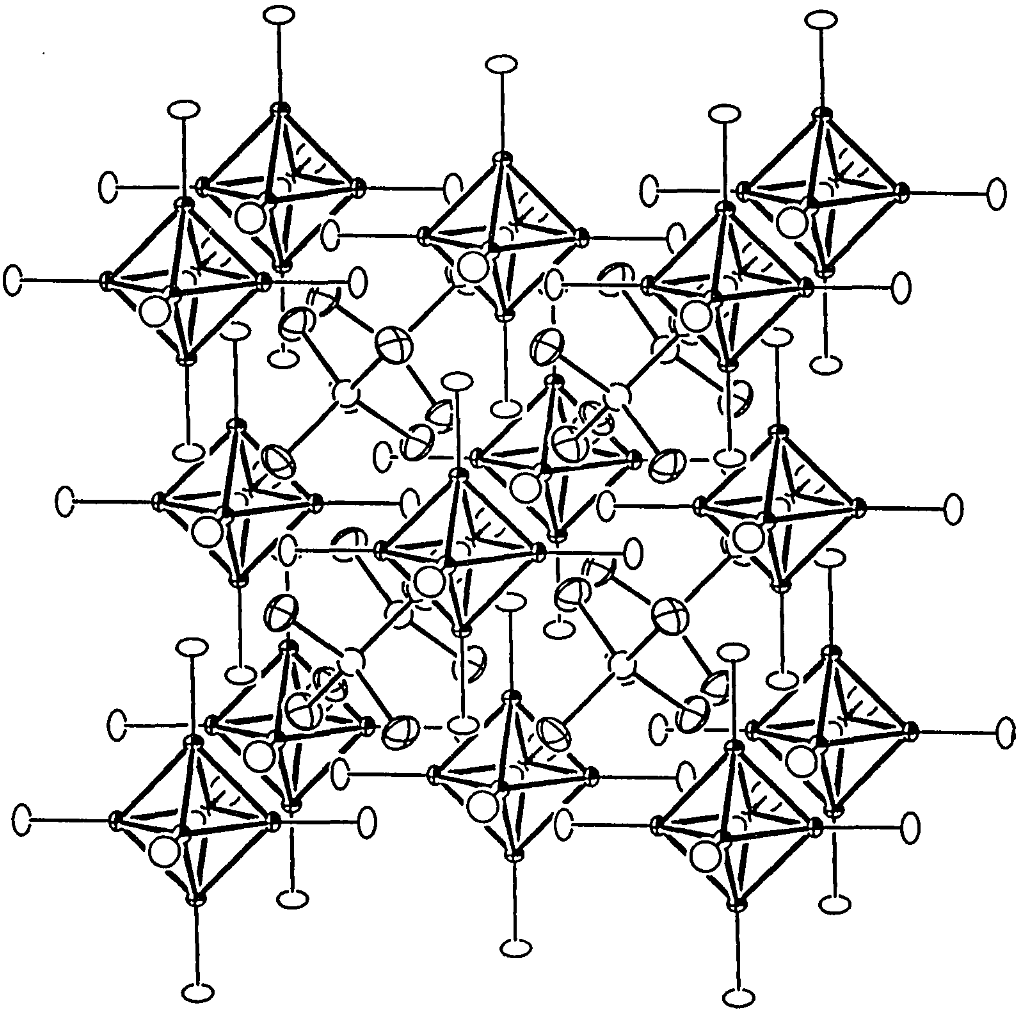

Figure 11. The unit cell view of $(K_4Br)_2Zr_6Br_{18}B$ with Br^i omitted for clarity. The lattice is composed of two structural fragments, i.e., isolated cluster units and $[K_4Br]^{3+}$ polycations. It adopts the antifluorite structure type with the $[K_4Br]^{3+}$ polycations in the tetrahedral site created by the negatively charged cluster units (70% probability)

tetrahedral environment created by four isolated cluster units (Figure 12). In other words, it adopts an antifluorite structure type. For a cation in the site created by four tetrahedrally arranged anions, the cation will push the anions apart when $r_m/r_x > 0.225$. Since the radius ratio of $[K_4Br]^{3+}$ to $\{[Zr_6Br^i_{12}B]Br^a_6\}^{-6}$ is about 0.59, the negatively charged cluster units are very well separated by the $[K_4Br]^{3+}$ polycations. Owing to its larger size, $[K_4Br]^{3+}$ can separate the anions more than Li^+ and some other simple countercations, while keeping a strong interaction with the anions. This is a very effective way to stabilize the lattice, and may be one of the major reasons that the polycation $[K_4Br]^{3+}$ is formed.

The tetrahedral environment for an isolated Br^- is very unusual, and has not been observed in any halide cluster phases before; neither has the polycation $[K_4Br]^{3+}$ except for the $[Cs_4Br]^{3+}$ in $(Cs_4Br)Zr_6Br_{16}B$ (6-16 type) and the $[Na_4Cl]^{3+}$ in one of the cage-like zeolites, i.e., sodalite.[67] One may find it very difficult to explain why the cubic structure was preferred over that of $Rb_5Zr_6Cl_{18}B$, a fundamental question in the field of solid state chemistry. The function of the isolated Br^-, however, can be justified as follows. Structurally, the existence of the isolated Br^- helps to reduce the repulsions among positively charged K^+ countercations. Electronically, the isolated Br atom acts as an electron sink to give the clusters with an optimal number of electrons or nearly so. The $[K_4Br]^{3+}$ polycation has an ideal tetrahedral arrangement (T_d point symmetry) with 109.47° K-Br3-K angle (Table 9). The Br3-K distance is 3.061(5)Å in $(K_4Br)_2Zr_6Br_{18}B$ and 3.093(5) Å in $(K_{3.4}Br)_2Zr_6Br_{18}B$. The difference ($4.5\sigma$) can

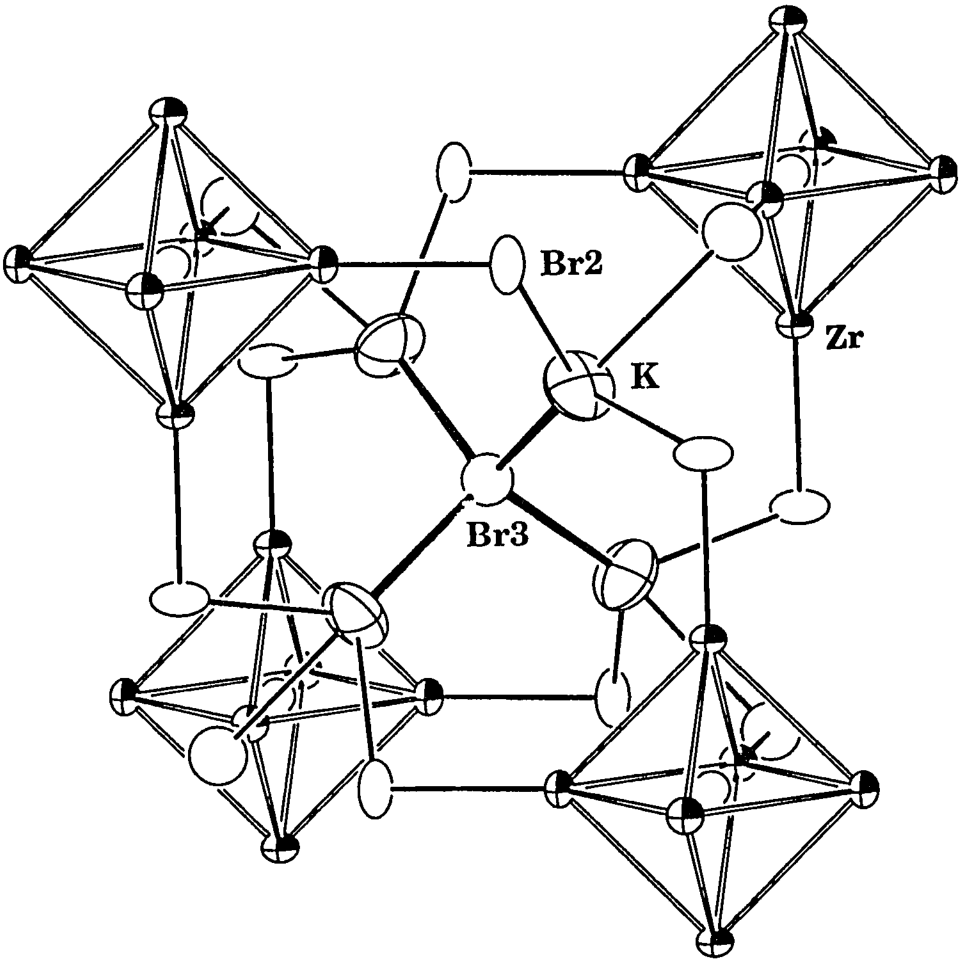

Figure 12. The environment of $[K_4Br]^{3+}$ in the lattice of $(K_4Br)_2Zr_6Br_{18}B$. It occupies the tetrahedral site created by the close packed clusters (70% probability)

can be attributed to the difference in the K occupancies, for the Br3 in the former has 4 K^+ as its neighbors and 3.4 K^+ in the latter.

The unique environment of the K^+ cation is pictured in Figure 13. It has 4 Br^- atoms (1 Br3 + 3 Br2) in its first bonding sphere, forming a distorted tetrahedron (133.35(8)° for Br2-K-Br3). The isolated Br3 is at the apical position and the three Br^a are 3.290(4) Å from the K^+, forming the basal plane of the distorted tetrahedron. The average K-Br distance within the first bonding sphere is 3.233 Å in $(K_4Br)_2Zr_6Br_{18}B$ and 3.229 Å in $(K_{3.4}Br)_2Zr_6Br_{18}B$, about 0.1 Å shorter than the summation of the corresponding crystal radii of Br^- and K^+, 3.33 Å (Br^-(VI), 1.82 Å; K^+(CN=4), 1.51 Å). According to the basic trend of the Br atoms mentioned earlier, the isolated Br3 should have the highest basicity among all the types of Br atoms. Therefore, the short K-Br3 distance may be justified by the high basicity as well as the low coordination number of Br3 (4 K) when compared with Br2 (1 Zr + 4 K). The second bonding sphere of K^+ is formed by six inner Br^- atoms (Br1) at 3.889(1) Å in $(K_4Br)_2Zr_6Br_{18}B$ and 3.904(4) Å in $(K_{3.4}Br)_2Zr_6Br_{18}B$. As shown in Figure 13, the six Br1 form a ring in between Br3 and Br2 atoms.

The cluster unit $[Zr_6BBr^i_{12}]Br^a_6$ has an O_h point symmetry. There are $15e^-$ available for the $[Zr_6B]$ cluster core in $(K_4Br)_2Zr_6Br_{18}B$. The Zr-B bond distance is 2.326(2) Å, and the Zr-Zr distance is 3.290(2) Å. Those in the ~14e cluster phase $(K_{3.4}Br)_2Zr_6Br_{18}B$ are 2.335(3) Å and 3.302(2) Å, respectively. Usually, the lattice with a larger matrix effect tends to stabilize the cluster phases with more

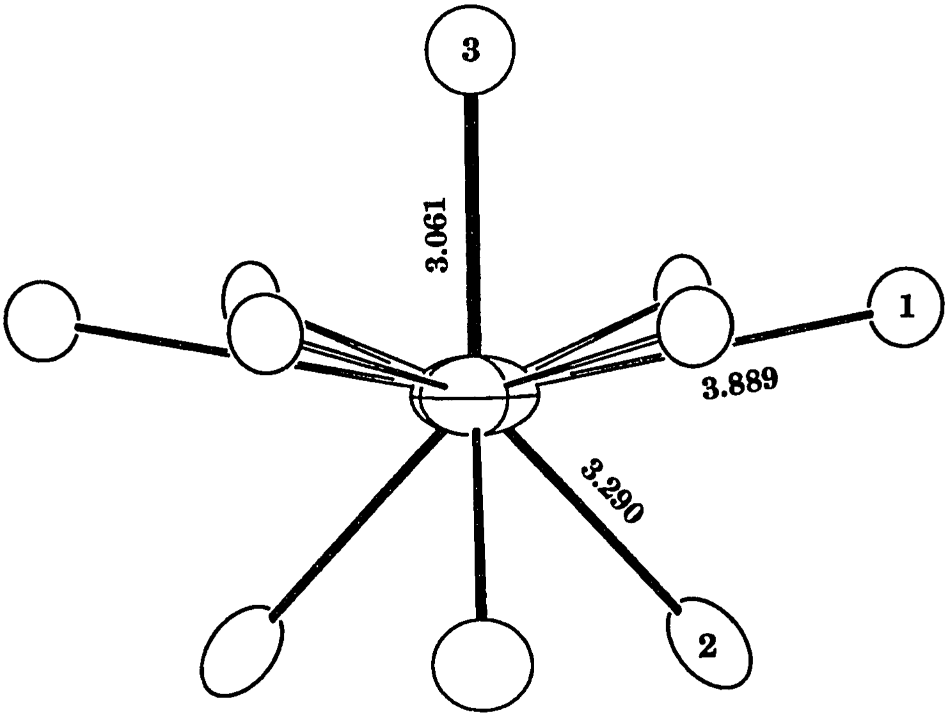

Figure 13. The local environment of K in $(K_4Br)_2Zr_6Br_{18}B$. It has C_{3v} point symmetry. There are four Br^- (1 Br3 + 3 Br2) in its first bonding sphere, and another six (Br1) in its second bonding sphere (70% probability)

than 14e in the bonding orbitals of the cluster unit. According to the extended Hückel calculations,[31] the HOMO is a_{2u} for a 15e or 16e compound (Figure 14). This a_{2u} orbital is slightly bonding among Zr atoms, and antibonding between Zr and Br^i. The larger withdrawal of the Zr from Br^i square planes (Figure 15) gives a_{2u} more bonding character. Consequently, it helps to stabilize the 15e or 16e cluster phases. Apparently, the larger withdrawal of Zr from the Br^i plane will result in a smaller trans Br^i-Zr-Br^i angle, a good criterion of the extent of the matrix effect. The trans Br^i-Zr-Br^i angle in the 15e phase $(K_4Br)_2Zr_6Br_{18}B$ is 164.60(5)°, and 165.4(1)° in the 14e one, indicating a slightly larger matrix effect in the former. The distance between Zr and Br2 (Br^a) in $(K_4Br)_2Zr_6Br_{18}B$ is 2.840(3) Å, 0.123 Å (39σ) longer than that between Zr and Br1 (Br^i), 2.717(1)Å. Again, it can be justified by the different coordination number of Br^a (1 Zr + 4 K) and Br^i (2 Zr).

Studying the structure carefully, one realizes that the body-centered position and the other three symmetry related positions, e.g. the middle point of the edges, are empty. These empty sites are surrounded by 6 Br2 atoms at a distance of 2.93 Å. Electronically, the occupation of this position is not preferable as the clusters in the boride already have either 14 or $15e^-$ in their bonding orbitals. Furthermore, it is not big enough to host a K^+ either. According to this, one reaction was loaded as $(K_4Br)_2NaZr_6Br_{18}Be$ and carried out at 850°C for four weeks. The powder patterns calculated with or without the Na in the body-center position are practically indistinguishable. Not surprisingly,

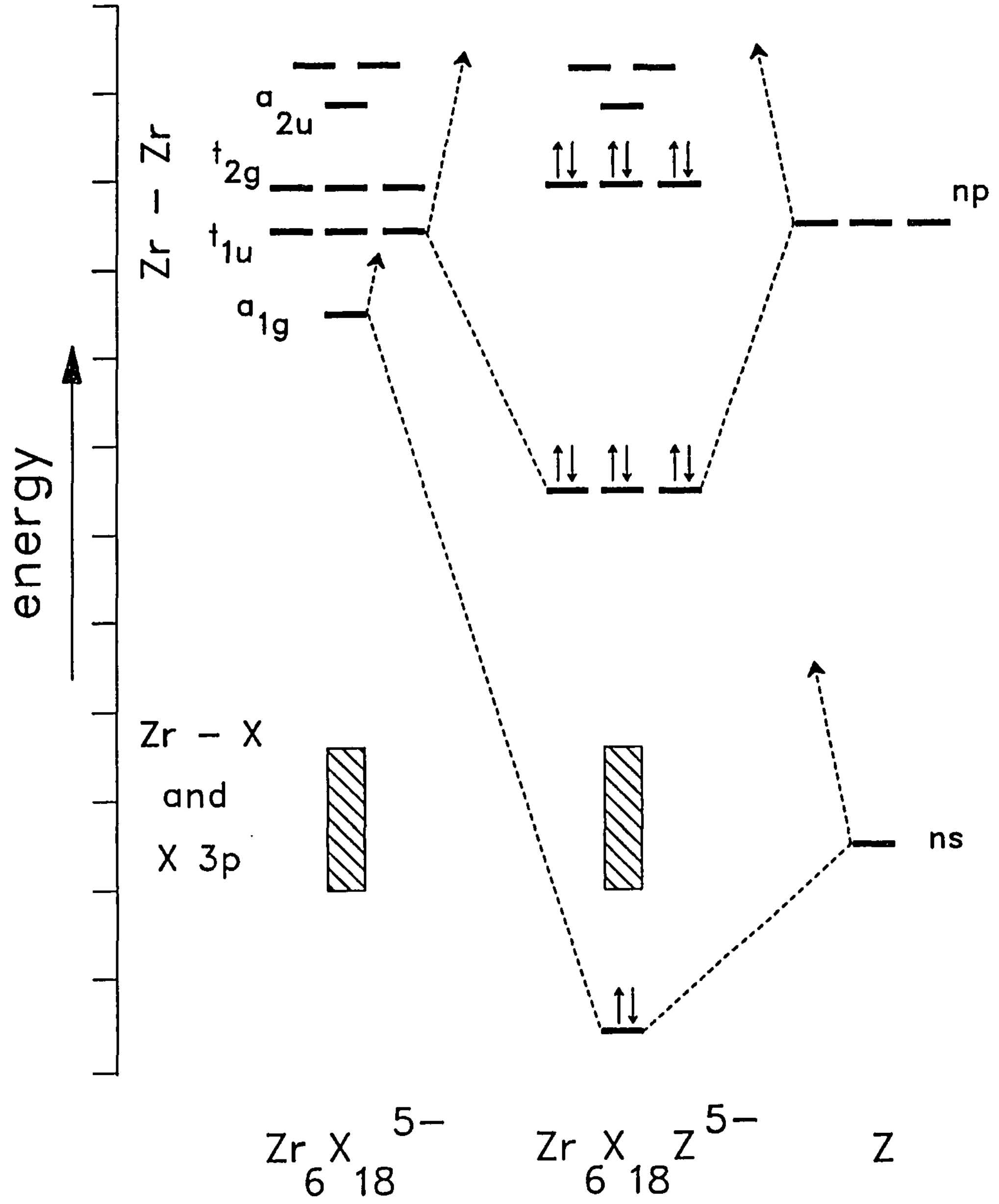

Figure 14. Molecular orbital diagrams from extended-Hückel calculations.[31] Left: Hypothetical $Zr_6X_{18}^{n-}$ cluster (O_h); Right: Main group interstitial Z; Center: Interstitial-centered $Zr_6X_{18}Z^{n-}$ 14e cluster (O_h)

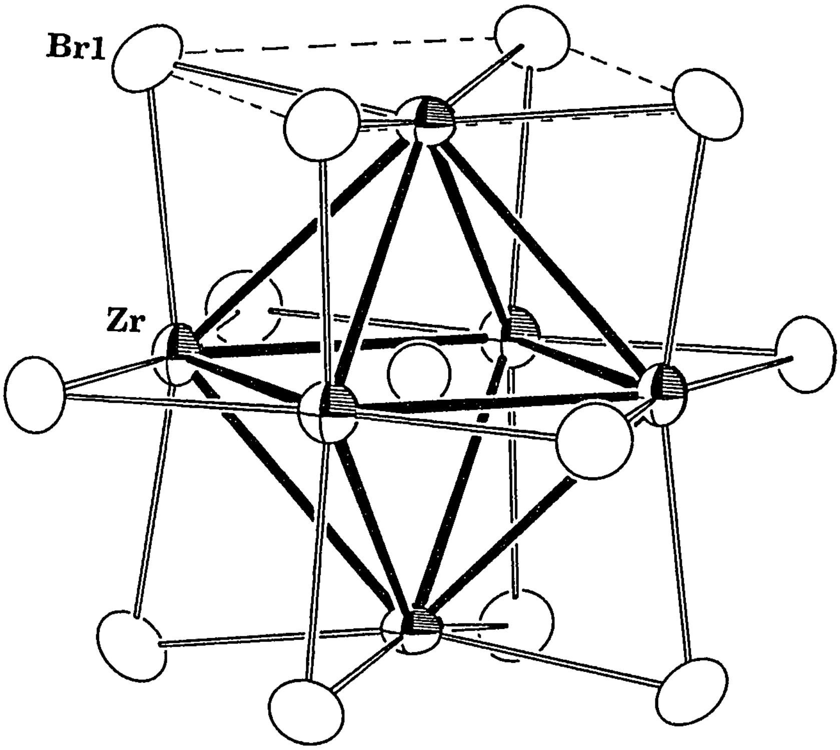

Figure 15. The $Zr_6Br^i_{12}B$ cluster unit in $(K_4Br)_2Zr_6Br_{18}B$, showing that Zr is pulled in from the Br^i square plane due to the matrix effect. The cluster unit has an ideal O_h point symmetry (70% probability)

the Guinier powder pattern of the product from the reaction mentioned above looked very similar to that of the K-containing phase. Its lattice constants refined as a=16.191(1) Å and V=4244.5(9) Å^3, significantly smaller than those of the pure K phase, a=16.240(2) Å and V=4283(1) Å^3. The magnetic susceptibility measurements showed a temperature-independent behavior, indicating the absence of unpaired electrons in the cluster units. In other words, Na did not go to the empty body-centered position, and the cluster cores remained with 14e in their bonding orbitals. The change in the lattice constants is probably caused by mixing Na into the K position.

One may wonder what would happen if all the K$^+$ cations were replaced by smaller Na$^+$ cations. A reaction loaded as $Na_8Zr_6Br_{20}Be$ yielded about 20% $Zr_6Br_{12}Be$, and the Guinier powder pattern of the rest of the product was similar to the cubic phase, except that some of the lines were split into two plus some very weak extra lines appeared, indicating a lower lattice symmetry. To compare, another reaction was also carried out with $Na_8Zr_6Br_{20}B$ as loaded stoichiometry. It turned out that the sodium boride retained the face-centered cubic lattice symmetry (Table 8). According to the preparations and compositions of the products, the beryllide phase contains a higher number of countercations than the cubic potassium-containing one and has $Na_9Zr_6Br_{20}Be$ as its empirical formula, if the empty site (4b position) is fully occupied by Na. Program TREOR was employed to index the powder pattern, and it gave two reasonable solutions. One was an orthorhombic cell with a=15.761(5) Å, b=11.167(3) Å, c=11.013(2) Å, and V=1938(1) Å^3, and the other one was a hexagonal setting cell with a=b=18.07(1) Å and c=11.156(5) Å. According to the line splitting observed in the Guinier powder pattern, the latter is more reasonable. It will be very interesting to study how the lattice is distorted by the extra Na. Workable single crystals from this phase, however, have not been found yet.

Magnetic Study on $(K_{4-x}Br)_2Zr_6Br_{18}B$: As mentioned earlier, the phase breadth for $(K_{4-x}Br)_2Zr_6Br_{18}B$ is x=0-0.5. When x=0, the clusters contain 15e in its bonding orbitals. In other words, each cluster contains one unpaired electron in the a_{2u} orbital. If it is true, the 15e phase should show a temperature-dependent paramagnetic behavior with 1.73 μ_B magnetic moment, the value for one unpaired, spin-only, localized electron in the transition metal clusters. The Curie-Weiss plot in Figure 16 comes from the product from the reaction loaded as $(K_4Br)_2Zr_6Br_{18}B$, and with 10% excess Zr (a=16.197(1) Å, V=4248.8(9) Å^3, (Table 10). As seen, it has a nearly ideal Curie-Weiss behavior over the entire temperature region with 1.77(1) μ_B as its magnetic moment, indicating that it is indeed a 15e cluster phase. The measurement on the product from the stoichiometric reaction (third reaction in Table 10, a=16.196(1) Å and V=4244.5(9) Å^3) showed a similar behavior, yet with a slightly lower moment 1.57(1) μ_B. In other words, the clusters in the latter have fewer than one unpaired electron in the bonding orbitals or the K site is slightly less than fully occupied. The measurements on the products from the other two reactions

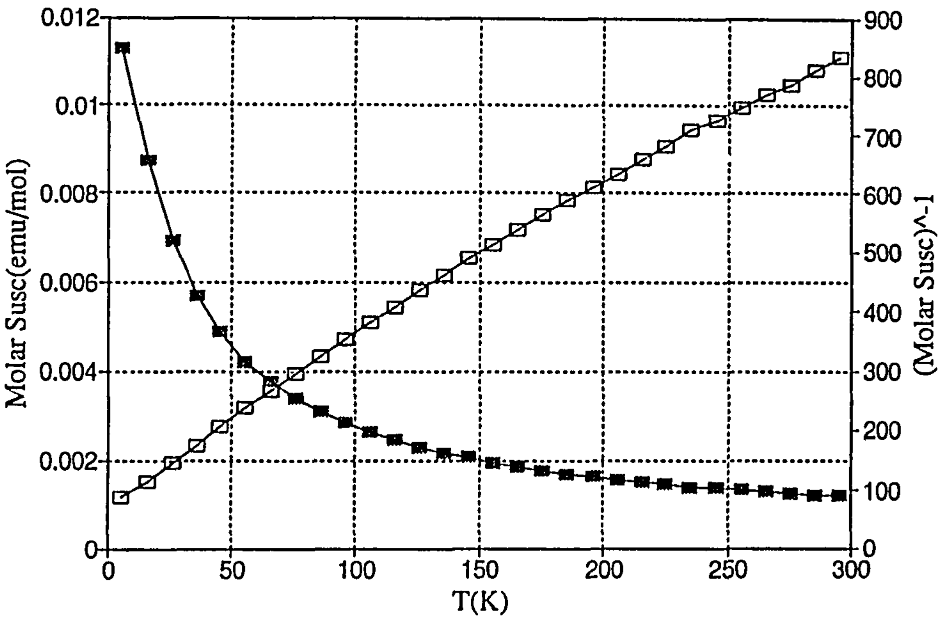

Figure 16. The magnetic susceptibility measurement conducted on $(K_4Br)_2Zr_6Br_{18}B$. It has a nearly ideal Curie-Weiss paramagnetic behavior over the entire temperature region with 1.77(1) μ_B as its magnetic moment

which were loaded as $(K_{3.75}Br)_2Zr_6Br_{18}B$ and $(K_{3.5}Br)_2Zr_6Br_{18}B$, exhibited a similar behavior, but with much smaller moments, 1.1(1) μ_B and 0.78(6) μ_B, respectively (Table 10).

6-17 Type

The discovery of the cluster phase $Ba_2Zr_6Cl_{17}B$ [43] completed the $[Zr_6ZCl_{12}]Cl_n$ $0 \leq n \leq 6$ series in the zirconium chloride system. The same is true in the bromide system. According to the connectivity between the clusters, this 6-17 can be expressed as $[Zr_6ZX^i_{12}]X^a_4X^{a\text{-}a}_{2/2}$. The linear cluster chains are formed by sharing one pair of the terminal Br atoms in trans positions. In this sense, these also completed the geometric series, for only two- and three-dimensional networks were previously found in the zirconium halide systems.

$Ba_2Zr_6Br_{17}B$

Synthesis: The 6-17 bromide phase $Ba_2Zr_6Br_{17}B$ was synthesized as designed. According to the study in the chloride system, the useful single crystals of the cluster phases with either alkaline-earth or rare-earth metal as countercations usually formed at relatively high temperatures (about 1000°C), yet with only the low yield (5-10%) of the target phase.[43] A high yield could be obtained at about 850°C with a loss of sizable single crystals. In some cases, vapor transporting agents helped the crystal growth.[68] Therefore, in the synthesis of $Ba_2Zr_6Br_{17}B$, a small amount of $AlBr_3$ was added to the reaction as a vapor transporting agent. The stoichiometric reaction was carried out at 900°C. In order to grow large enough crystals, the reaction was purposely run for an extended period of time, i.e., 40 days. As expected, the product contained more than 95% $Ba_2Zr_6Br_{17}B$, and large crystals were found in this reaction as well. Reactions with carbon as interstitial and Ba or Ca as countercations yielded an unknown phase B. No single crystals have been available for this phase yet. The reaction loaded as $Ba_3Zr_6Br_{18}Be$ failed to give the target phase. Except for some unrecognized very weak lines, the nice strong lines shown in the powder pattern were those from $BaBr_2$.

Single Crystal Study: The powder pattern of $Ba_2Zr_6Br_{17}B$ looked identical to that of $Ba_2Zr_6Cl_{17}B$ except that lines from the bromide phase shift slightly towards the lower angle. All the lines could be indexed according to the structural information obtained from the corresponding chloride phase which has a body-centered tetragonal lattice. In other words, the bromide phase has the same structure as adopted by $Ba_2Zr_6Cl_{17}B$. The data collection was performed on an ENRAF NONIUS CAD4 diffractometer. The reflections found in the random search could be indexed in a primitive triclinic cell which was transformed to the body-centered tetragonal cell by the program TRANS. Two octants of data were collected with the body-centering reflection condition (h+k+l=2n) applied. The other important data collection parameters are listed in Table 11. An empirical absorption correction was done according to three averaged ψ-scan measurements. All the corrected data were merged in the 4/m point group with R_{ave} as 4.8%. The extinction conditions, l=2n+1 for hhl type and k=2n+1 for 0k0 type reflections were also observed. These extinction conditions fulfill the

Table 11. Crystal data for $Ba_2Zr_6Br_{17}B$

space group, Z	I4/m (no. 87), 2
cell parameters[a]	
a (Å)	12.0406(5)
c	10.3180(5)
V (Å^3)	1495.9(2)
crystal dimens. (mm)	0.16 x 0.17 x 0.23
octants measured	±h, k, l
2θ (max.), deg.	50
reflections	
measured	1446
observed (I/σ(I)>3.0)	1045
indep.	522
abs. coeff. (Mo Kα, cm^{-1})	270.60
transm. coeff. range	0.60-1.00
R_{ave}, % (all data)	4.8
no. variables	37
sec. extinct. coeff.	5.7(1) x 10^{-6}
R, %	3.0
R_w, %	3.8

[a] Guinier data

requirements of the space group I4/m which was used in solving the structure of $Ba_2Zr_6Cl_{17}B$. The atomic positions refined in $Ba_2Zr_6Cl_{17}B$ were utilized as the initial model, and the isotropic refinement carried out for all the atoms except for the light interstitial atom boron converged at R=8.7% and R_w=11.4%. At this stage, the thermal parameters of the two Zr positions were negative, but they became positive after the secondary extinction coefficient was refined. Besides, the residue values also dropped to R=5.9% and R_w=6.3%. The relative large secondary extinction coefficient ($5.7(1)x10^{-6}$) could be the result of the near perfectness of the crystal grown with the aid of the vapor transporting agent, $AlBr_3$. The anisotropic refinement went smoothly and converged at R=3.0% and R_w=3.8%. The final difference Fourier map was calculated after the isotropic thermal parameter of the interstitial element boron was refined. The background of the map was basically flat as the largest peak was 1.1 e/Å^3, 1.14 Å away from Zr1. The other structure refinement results are listed in Table 11 and the atomic positions and anisotropic thermal parameters are compiled in Table 12.

Structure Description: As mentioned earlier, $Ba_2Zr_6Br_{17}B$ is isostructural with the corresponding chloride phase $Ba_2Zr_6Cl_{17}B$. The clusters form one-dimensional linear chains along the crystallographic c axis by sharing one pair of the terminal bromine atoms in trans positions (Figure 17). Within each unit cell, there are two independent cluster chains related by the body-centering symmetry. Without considering the function of the Ba^{2+} cations in the

Table 12. Positional and thermal parameters for $Ba_2Zr_6Br_{17}B$

Atom	Psn.	x	y	z	B_{eq}(Å^2)
Zr1	8(h)	0.0681(1)	0.1809(1)	0	0.58(7)
Zr2	4(e)	0	0	0.2270(2)	0.57(5)
Br1	16(i)	0.4185(1)	0.2932(1)	0.2429(1)	1.28(6)
Br2	8(h)	0.2855(2)	0.1286(2)	0	1.09(8)
Br3	8(h)	0.1419(2)	0.4062(1)	0	1.41(9)
Br4	2(b)	0	0	1/2	2.1(1)
Ba	4(d)	0	1/2	1/4	2.17(5)
B	2(a)	0	0	0	0.4(7)

[a] U x 10^3

U_{11}[a]	U_{22}	U_{33}	U_{12}	U_{13}	U_{23}
6.6(9)	4.9(9)	11(1)	-0.6(8)	0	0
7.1(7)	U_{11}	7(1)	0	0	0
22.7(7)	11.6(6)	14.1(8)	-4.8(6)	-2.7(6)	-3.2(6)
7(1)	11(1)	23(1)	-3.2(8)	0	0
20(1)	11(1)	23(1)	-6(1)	0	0
38(2)	U_{11}	4(2)	0	0	0
31.9(7)	U_{11}	19(1)	0	0	0

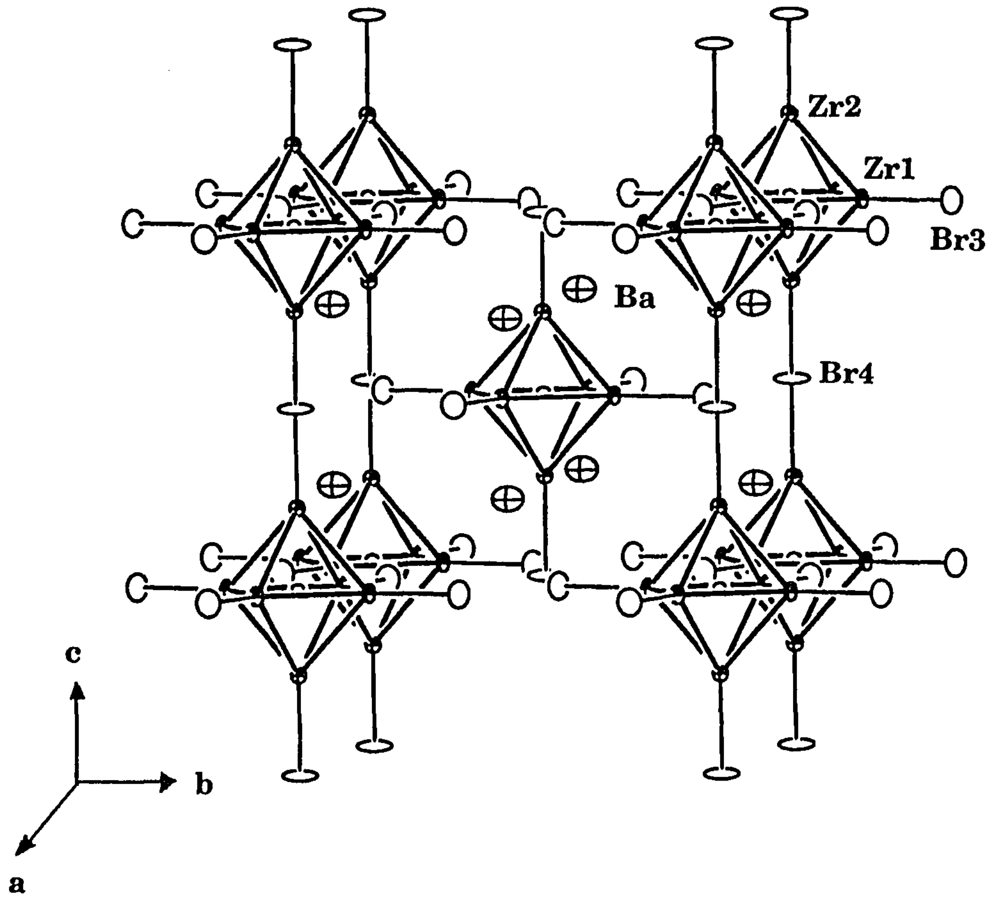

Figure 17. The unit cell view of $Ba_2Zr_6Br_{17}B$, showing the linear cluster chains are along the c direction. The inner Br^i atoms are omitted for clarity. The open circles are drawn for the Br^a and $Br^{a\text{-}a}$ atoms and the crossed ones for the Ba^{2+} cations (90% probability)

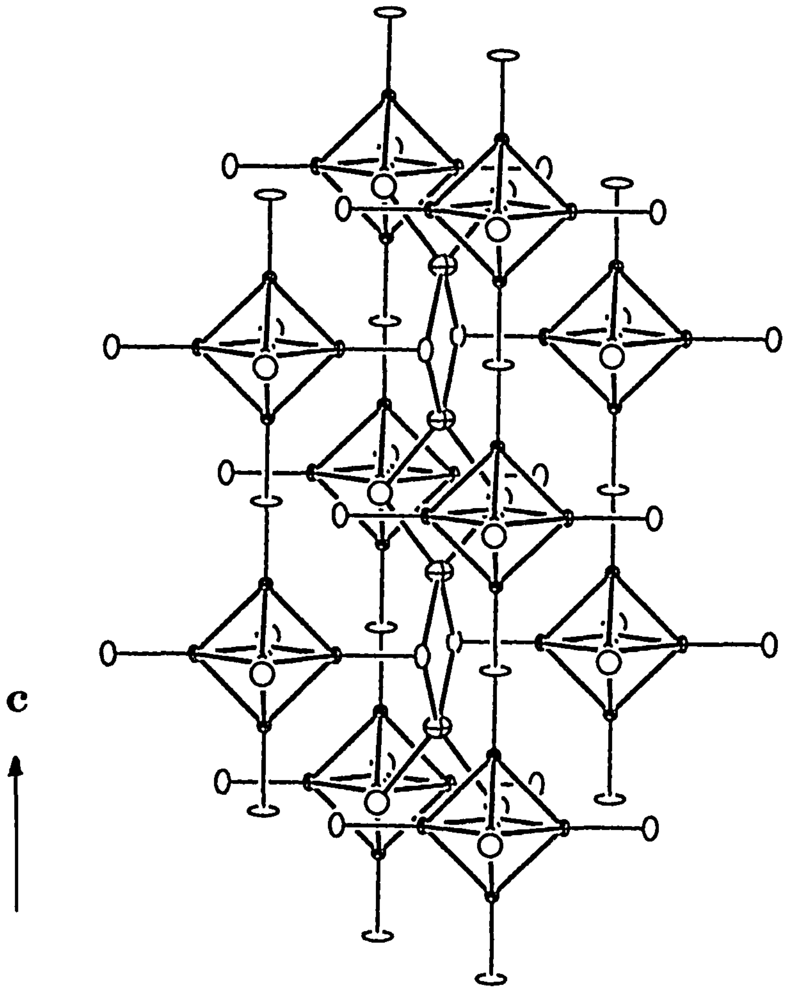

Figure 18. The extended view along the c axis of $Ba_2Zr_6Br_{17}B$, emphasizing the role of Ba^{2+} in combining the isolated cluster chains into the lattice. The crossed-ellipsoids represent Ba^{2+} cations and the open circles are drawn for Br^a and $Br^{a\text{-}a}$. The inner Br^i atoms are left out for clarity (90% probability)

lattice, these cluster chains may be described as isolated. According to the drawing in Figure 18, these cluster chains are, in fact, connected via the Ba^{2+} cations. In other words, Ba^{2+} cations serve as a binding force to combine these otherwise isolated cluster chains into the lattice by strongly interacting with the terminal bromine atoms around the waist of the clusters. One may notice in Figure 18 that each Ba atom is tetrahedrally surrounded by four cluster units with S_4 point symmetry ($\bar{4}$ axis vertical). The four closest bromine neighbors are the Br^a atoms at the distance of 3.294(1) Å (Table 13). The extrapolated 4-coordinate Ba^+ crystal radius is about 1.44 Å. This makes the Ba-Br^a distance very reasonable. Besides, there are also eight more inner bromine atoms (Br^i) at distances of 3.665(1) Å and 3.966(1) Å, respectively (Figure 19). If only considering the bromine atoms at the distance shorter than 3.7 Å, the average Ba-Br distance is 3.480(1) Å, which is fairly comparable to the sum of the 8-coordinate Ba^{2+} and corresponding Br^- crystal radii, 3.38 Å. The same holds true if one takes into account all the twelve bromine atoms within the range of 4.0 Å. In this case, the average distance is 3.642 Å, rather close to the sum of the crystal radii of 12-coordinate Ba^{2+} and Br^-, 3.57 Å. In most of cluster phases, Zr-$X^{a\text{-}a}$ bond is usually longer than that of Zr-X^a. In $Ba_2Zr_6Br_{17}B$, however, the Zr-Br^a bond distance is 2.854(2) Å, 0.038 Å (10σ) longer than that of Zr-$Br^{a\text{-}a}$, 2.816(3) Å. This abnormality could be attributed to the higher coordination number of Br^a (1 Zr + 2 Ba) vs $Br^{a\text{-}a}$ (2 Zr). The shortest Zr-Br bonds are those of Zr-Br^i, ranging from 2.676(1) Å to 2.695(1) Å.

Table 13. Important bond distances (Å) and angles (°) in $Ba_2Zr_6Br_{17}B$

d(Zr-Zr)			d(Br-Br)[b]		
Zr1-Zr1	x2[a]	3.291(2)	Br1-Br1	x2	3.786(2)
Zr1-Zr2	x4	3.302(2)	-Br2	x1	3.574(2)
$\bar{d}$		3.298		x1	3.735(2)
				x1	3.786(2)
d(Zr-B)			-Br3	x1	3.651(2)
Zr1-B	x1	2.327(2)		x1	3.749(2)
Zr2-B	x1	2.343(3)	-Br4	x1	3.667(1)
$\bar{d}$		2.332	Br2-Br3	x1	3.567(3)
				x1	3.717(3)
d(Zr-Br^i)				x1	3.762(3)
Zr1-Br1	x2	2.676(1)			
Zr1-Br2	x1	2.683(3)			
Zr1-Br2	x1	2.692(3)			
Zr2-Br1	x4	2.695(1)			
d(Zr-Br^a)			Zr1-Zr1-Zr1	x1	90.00
Zr1-Br3	x1	2.854(2)	Zr1-Zr1-Zr2	x2	60.11(2)
			Zr1-Zr2-Zr1	x1	89.62(7)
d(Zr-Br^{a-a})				x2	59.78(4)
Zr2-Br4	x1	2.816(3)	Zr2-Zr1-Zr2	x4	90.38(7)
			Br1-Zr1-Br1	x1	164.89(9)
d(Ba-Br)			Br1-Zr2-Br1	x1	166.8(1)
Ba-Br3	x4	3.294(1)	Br2-Zr1-Br2	x1	165.52(8)
-Br1	x4	3.665(1)	Zr1-Br1-Zr2	x2	75.87(7)
-Br2	x4	3.966(1)	Zr1-Br2-Zr1	x1	75.52(8)
$\bar{d}$(CN=8)		3.480	Br1-Ba-Br1	x1	177.70(4)
$\bar{d}$(CN=12)		3.642	Br3-Zr1-B	x1	177.51(9)

---

[a] Number of times the distances and angles occur per atom

[b] d(Br-Br) < 3.8 Å

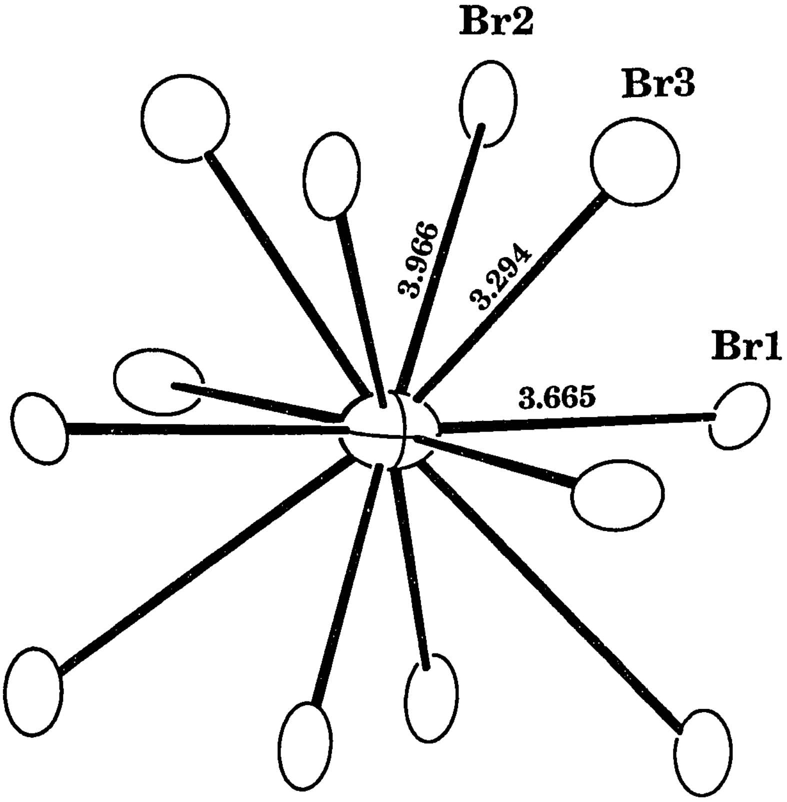

Figure 19. The local environment of Ba^{2+} in the lattice of $Ba_2Zr_6Br_{17}B$. The picture is drawn with the S_4 axis vertical through the central Ba^{2+} cation (90% probability)

Like most of the zirconium halide cluster phases, the [Zr_6B] cluster core in $Ba_2Zr_6Br_{17}B$ has $14e^-$ in its bonding orbitals. The cluster unit has the C_{4h} point symmetry. The average Zr-Zr distance in $Ba_2Zr_6Br_{17}B$ is 3.298(2) Å, 0.043(2) Å (21σ) longer than that in $Ba_2Zr_6Cl_{17}B$. The average Zr-B distance is 2.332(3) Å, 0.031(3) Å (10σ) longer than that in the corresponding chloride phase. Since the lattice symmetry, the type of the countercation, and the interstitial element in the bromide 6-17 phase are exactly the same as those in the chloride, the differences between the Zr-Zr and Zr-B bond distances are solely caused by the different halide ligands. Therefore, this is the best situation to compare the magnitude of the matrix effect caused by different halogen anions.

The ideal M_6X_{12} clusters probably consist of cuboctahedra of halide with metals more-or-less centered on the square faces created by X^i atoms. In practice, all clusters with X=Cl, Br, I deviated from this norm to an increasing degree. Because of relative sizes, the X^i-X^i distances about the cluster are often intrinsically greater than optimal M-M distances in most bonded M_6 octahedra. Therefore, the metal atoms are often significantly withdrawn from the X^i_4 planes about them as seen in Figure 20. This drive to achieve more appropriate M-M bonding pulls the halogens toward each other and into increasingly repulsive interactions, limiting at about 3.6 Å in chlorides, 3.7 Å in bromide, and 4.0 Å in iodides. Because of this, the M-M bonding is compromised and forced to be less than optimal, the so called matrix effect. This explains why the Zr-Zr and

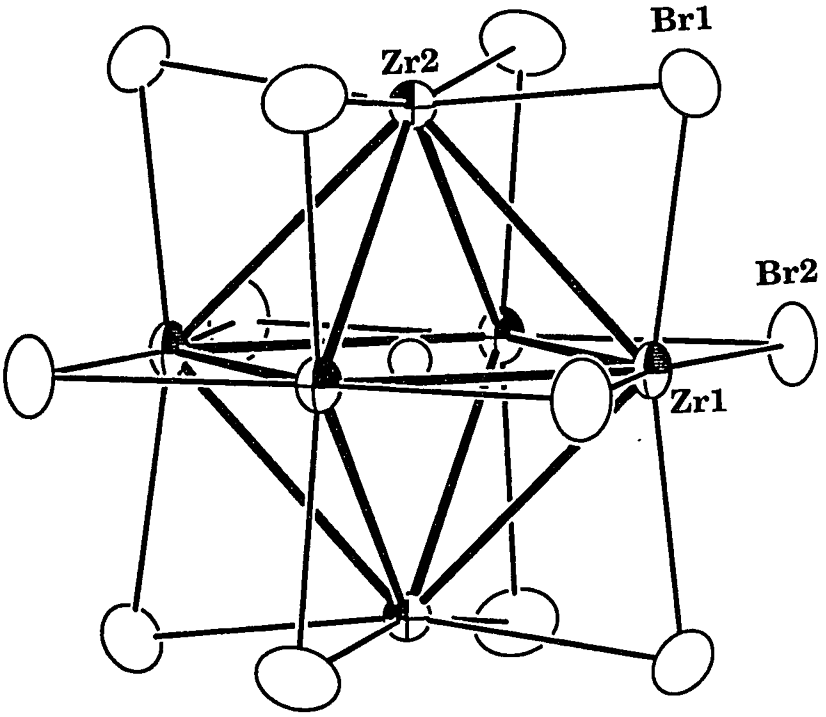

Figure 20. The $(Zr_6B)Br^i_{12}$ cluster in $Ba_2Zr_6Br_{17}B$, showing the withdrawn of the Zr atoms from the square planes of Br^i_4. The cluster has the C_{4h} point symmetry and the picture is drawn with the 4 fold axis vertical (90% probability)

Zr-B distances in $Ba_2Zr_6Br_{17}B$ are longer than those in $Ba_2Zr_6Cl_{17}B$. The trans X^i-M-X^i angle is a good measurement of the magnitude of the matrix effect. The average Br^i-Zr-Br^i trans angle in $Ba_2Zr_6Br_{17}B$ is 165.74(9)°, 3.47(9)° (38σ) smaller than that in $Ba_2Zr_6Cl_{17}B$. It is why the increase of the Zr-Zr and Zr-B distances in the bromide are much smaller than the size difference between Br^- and Cl^-, 0.15 Å.

6-16 Type

The earlier investigations in the zirconium–chloride system provided two slightly different 6-16 phases, $Na_{3.9}Zr_6Cl_{16}Be$ and $Cs_{3.0}Zr_6Cl_{16}C$.[42] With four of the terminal chlorine atoms shared by the adjacent cluster units, these two 6-16 phases both form two-dimensional networks. The 14e⁻ cluster phase $Na_{3.9}Zr_6Cl_{16}Be$ has an orthorhombic lattice symmetry with Na^+ cations distributed within the layers and in the cavities between the layers. The 15e⁻ cluster phase $Cs_3Zr_6Cl_{16}C$, on the other hand, has a monoclinic lattice symmetry with big Cs^+ cations occupying the positions only between the cluster layers.

The recent explorations in the zirconium–bromide system added three more 6-16 phases to the halide systems. Among them, $Na_3Zr_6Br_{16}B$ is related to $Na_{3.9}Zr_6Cl_{16}Be$, and $Cs_4Zr_6Br_{16}Be$ adopts the structure type exhibited by $Cs_3Zr_6Cl_{16}C$. The third 6-16 phase has a new structure type which cannot be converted to the other two 6-16 types without breaking and rearranging the Zr-$Br^{a\text{-}a}$-Zr bonds. It has wavy cluster layers stacked in eclipsed fashion, i.e., ...AAA.... The one–dimensional tunnels created by this kind of layer packing lie perpendicular to the layer and are occupied by the new polycations $[Cs_4Br]^{3+}$. Structurally, this new 6-16 phase should be expressed as $(Cs_4Br)Zr_6Br_{16}B$, even though its empirical formula is $Cs_4Zr_6Br_{17}B$. This section will focus on these three 6-16 bromide phases and their structural relationships.

$NA_3ZR_6BR_{16}B$

Synthesis: Similar to $Cs_3Zr_6Cl_{16}C$, $Na_3Zr_6Br_{16}B$ could only be made with excess Zr. The stoichiometric reactions always yielded an unknown phase C, which was also observed in the reactions with more Na. However, good single crystals have not been available to study the structure of this unknown phase. A relatively high yield of $Na_3Zr_6Br_{16}B$ was obtained in the reaction loaded as $Na_2Zr_6Br_9B$ and carried out at 820°C for about 40 days. Nice needle-like crystals were found therein. Its Guinier powder pattern looked very similar to that of $Na_{3.9}Zr_6Cl_{16}Be$; however, whether the bromide was a 15e^- $Na_4Zr_6Br_{16}B$ or 14e^- $Na_3Zr_6Br_{16}B$ remained unknown at this stage. Therefore, its single crystal structure was characterized to determine the Na content. It turned out that the structure refinement not only yielded the Na content, but also revealed the distribution of Na^+ in three crystallographic cation sites available in the lattice.

Single Crystal Study: Data collection was performed on an ENRAF NONIUS CAD4 diffractometer. The 25 peaks found in SEARCH could be indexed in the expected orthorhombic cell. Therefore, two octants of data were collected up to 50° in 2θ. An ω-scan mode was chosen according to peak profiles. An empirical absorption correction was conducted according to three averaged ψ-

scan measurements. The extinction conditions found in the data set were l=2n+1 for 0kl and h0l, h+k=2n+1 for hk0, indicating that space group Pccn was the right choice. All the observed data ($I>3\sigma$) were merged in the corresponding point group mmm with R_{ave}=4.4% The other important parameters related to the data collection and the structure refinement can be found in Table 14.

The Zr and Br positions were obtained using the direct methods provided by the SHELXS-86 package. After the isotropic refinement of all Zr and Br atoms, two relatively large peaks showed up in the difference Fourier map with heights of 11 e/Å^3 and 6 e/Å^3. They each had six Br neighbors at the distances reasonable for Na-Br bonds. Thus, these two positions were loaded as Na atoms. The refined occupancy of Na1 was not different from unity by 2σ and was fixed at full occupancy in the final refinement. The second Na position (Na2) was refined to have the occupancy as 0.52(3). The isotropic refinement converged at R=6.8% and R_w=5.9%, and the anisotropic refinement went smoothly and converged at R=5.3% and R_w=4.4%. After the temperature factor of boron was refined, the final different Fourier map was calculated. The largest peak, 2.7 e/Å^3, was right at the position which was occupied by Na3 in $Na_{3.9}Zr_6Cl_{16}Be$. The heights of the next 5 peaks, however, ranged from 2.2 to 1.8 e/Å^3. In other words, the background of the different Fourier map was fairly bumpy. Since the first peak was not very distinguishable from the background, it was not considered as a real Na peak even though it has reasonable bond distances to the adjacent Br atoms. According to the refinement, this 6-16 cluster phase had

Table 14. Crystal data for $Na_3Zr_6Br_{16}B$

space group, Z	Pccn (no. 56), 4
cell parameters[a]	
a (Å)	13.869(1)
b	14.720(1)
c	14.5814(7)
V (Å^3)	2976.9(3)
crystal dimens. (mm)	0.03 x 0.05 x 0.31
octants measured	h, k, ±l
2θ (max.), deg.	50
reflections	
measured	5677
observed (I/σ(I)>3.0)	1711
indep.	1044
abs. coeff. (Mo Kα, cm^{-1})	233.13
transm. coeff. range	0.68-1.00
no. variables	115
R_{ave}, % (obs.)	4.4
sec. extinct. coeff.	0
R, %	5.3
R_w, %	4.4

[a] Guinier data

$Na_{3.04(6)}Zr_6Br_{16}B$ as its empirical formula, giving the zirconium clusters an optimal electron count, i.e., 14e$^-$. The atom positions and their anisotropic thermal parameters are listed in Table 15.

Structure Description: The network of $Na_3Zr_6Br_{16}B$ is very similar to that of $Na_{3.9}Zr_6Cl_{16}Be$. As shown in Figure 21, the four $Br^{a\text{-}a}$ atoms about the waist of a Zr_6 octahedron are shared by the adjacent Zr_6 octahedra to generate an extended two–dimensional network along b and c directions. As seen, the Zr-Br^a bonds are not perpendicular to the cluster layer, rather are about 10° from the ac plane. There are two kinds of columns within each layer. As the picture in Figure 22 demonstrates, clusters in column A tilt in the direction opposite to those in column B. These cluster axes, on the other hand, are perpendicular to the cluster layers in the ab plane. There are two cluster layers within the unit cell (Figure 21). The stacking of these layers is staggered (...ABAB...) so that the terminal Br atoms from clusters in one layer lie in voids in the cluster layers above and below (Figure 23).

As mentioned earlier, the Na1 position has the full occupancy, while the Na2 position is 52(3)% occupied. The total Na amount is determined by the optimal electron count (14e$^-$) of the clusters. The distribution of these Na atoms, however, has something to do with the environment of these Na positions. There are 2 Br^a (Br6), 1 $Br^{a\text{-}a}$ (Br7), and 3 Br^i atoms around Na1 position and 1 Br^a, 1 $Br^{a\text{-}a}$, 4 Br^i around Na2. For the empty "Na3" position, however, there are no Br^a atoms around it. The adjacent atoms are 2 $Br^{a\text{-}a}$ and 4 Br^i. Usually,

Table 15. Positional and thermal parameters for $Na_3Zr_6Br_{16}B$

Atom	Psn.	x	y	z	B_{eq}(Å^2)
Zr1	8(e)	0.9788(2)	0.4063(2)	0.3738(2)	1.4(1)
Zr2	8(e)	0.5272(2)	0.3776(2)	0.0972(2)	1.3(1)
Zr3	8(e)	0.1650(2)	0.4679(2)	0.4996(2)	1.4(1)
Br1	8(e)	0.3454(3)	0.3246(2)	0.1128(2)	2.2(2)
Br2	8(e)	0.7193(2)	0.3941(2)	0.1106(2)	2.1(2)
Br3	8(e)	0.2887(2)	0.5692(2)	0.1458(2)	2.2(2)
Br4	8(e)	0.6635(3)	0.6446(2)	0.1475(2)	2.6(2)
Br5	8(e)	0.5113(3)	0.4687(2)	0.2575(2)	2.2(2)
Br6	8(e)	0.8656(2)	0.5702(2)	0.0025(3)	2.7(2)
Br7	8(e)	0.4444(3)	0.7212(2)	0.2793(2)	2.2(2)
Br8	8(e)	0.4394(3)	0.7481(2)	0.0338(2)	2.2(2)
Na1	8(e)	0.553(1)	0.085(1)	0.082(1)	4.1(8)
Na2[b]	8(e)	0.625(2)	0.826(2)	0.180(2)	6(2)
B	4(a)	0	0	0	2(1)

[a] U x 10^3

[b] 52(3)% occupied

U_{11}[a]	U_{22}	U_{33}	U_{12}	U_{13}	U_{23}
20(2)	19(2)	15(2)	2(1)	-1(2)	-2(1)
18(2)	18(2)	15(2)	-1(1)	0(2)	-0(1)
15(1)	19(2)	18(2)	2(1)	-1(2)	-3(2)
22(2)	31(2)	30(2)	-6(2)	0(2)	10(2)
23(2)	31(2)	28(2)	3(2)	-3(2)	5(2)
21(2)	37(2)	26(2)	-0(2)	4(2)	-10(2)
25(2)	41(3)	34(2)	-9(2)	-1(2)	-10(2)
43(2)	24(2)	16(2)	5(2)	1(2)	-0(2)
17(2)	41(2)	45(2)	-5(2)	-6(2)	2(2)
39(2)	23(2)	22(2)	-2(2)	1(2)	-7(2)
42(2)	22(2)	21(2)	3(2)	2(2)	1(2)
50(10)	50(10)	60(10)	-4(7)	5(9)	-10(10)
70(10)					
20(10)					

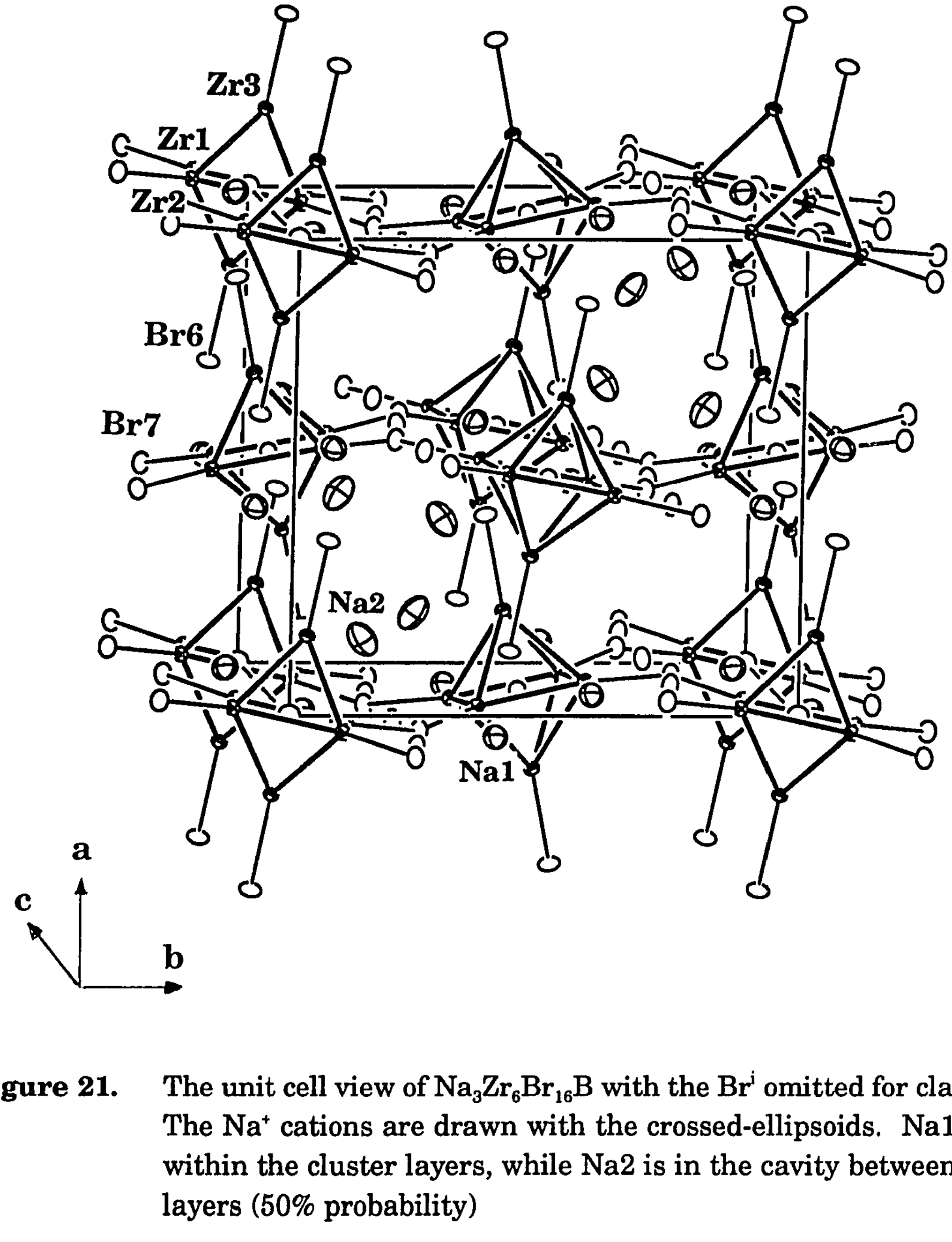

Figure 21. The unit cell view of $Na_3Zr_6Br_{16}B$ with the Br^i omitted for clarity. The Na^+ cations are drawn with the crossed-ellipsoids. Na1 is within the cluster layers, while Na2 is in the cavity between the layers (50% probability)

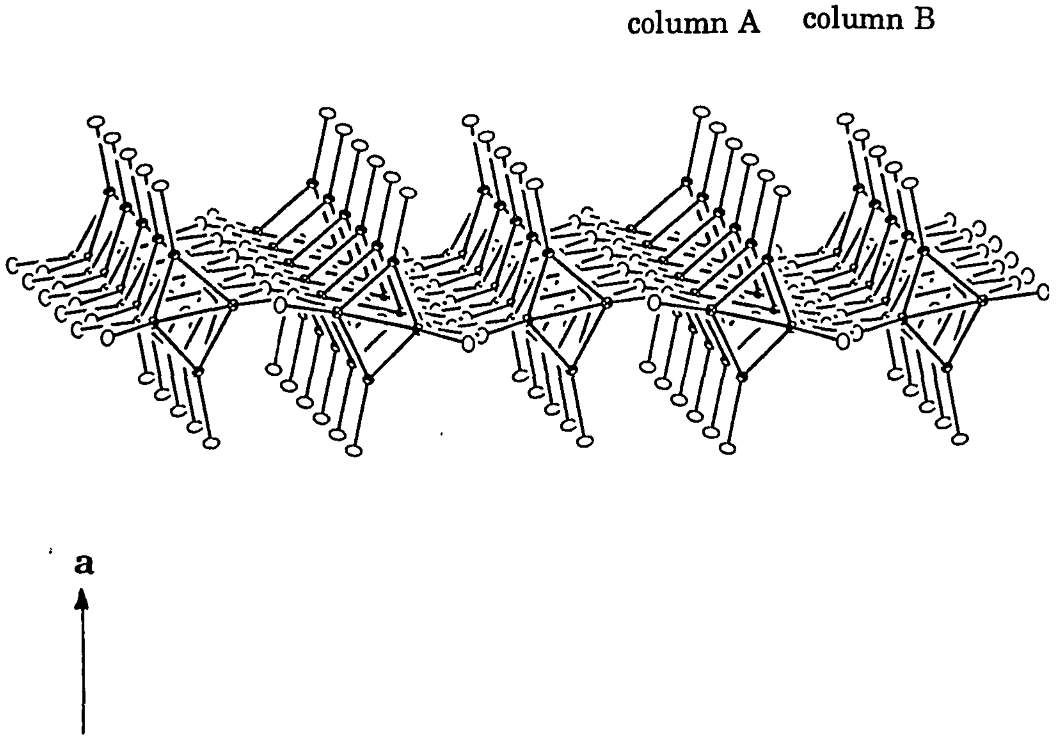

Figure 22. A view of cluster layer in $Na_3Zr_6Br_{16}B$. The terminal Br^a atoms are in trans positions. The clusters in column A and B tilt away from ac plane by 10°, yet in alternate directions (50% probability)

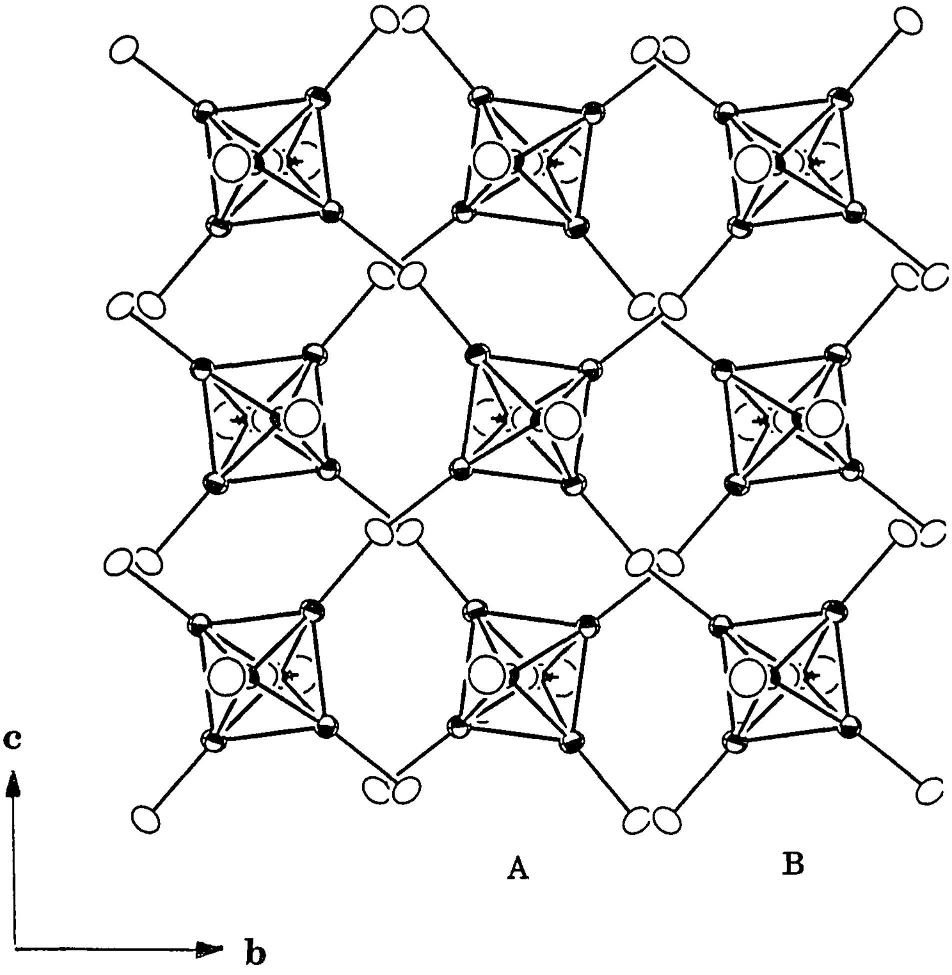

Figure 23. The [100] view of two layers in $Na_3Zr_6Br_{16}B$ showing that the cluster layers are stacked in ...ABAB..., or each cluster unit sits in the void created by the clusters in the layers above and below (90% probability)

cations tend to occupy positions that fall higher in the expected basicity ranking $X^a>X^{a-a}>X^i>X^{i-a}$, where X represents halide anions.[18] Therefore, it is rather clear why the Na3 position is less favored. As seen in Figure 21, Na atoms in the Na1 position are basically located within the cluster layers. Those in the Na2 position, on the other hand, arrange themselves in opposite quadrants of the cell between the layers. As seen, these two areas are different from those in the other pair in that the neighboring Br^a atoms point towards the former but away from the latter two. This is why Na3 would not have any Br^a as its neighbors. The average Na1-Br and Na2-Br distances are 2.96(2) Å and 3.01(3) Å, respectively, in a very good agreement with the sum of the corresponding crystal radii of Br^-(VI) and Na^+(VI), 2.98 Å (Table 16).

The cluster core [Zr_6B] has C_i point symmetry. The average Zr-Zr distance is 3.290(4) Å and the Zr-B distance is 2.326(3) Å The Zr-Br^{a-a} distances are the longest ones among all the Zr-Br bonds, 2.955(4) Å and 2.950(5) Å, respectively. The Zr-Br^a is 2.838(4) Å, longer than those of Zr-Br^i, ranging from 2.649(5) Å to 2.710(5) Å.

Compared with the structure of $(K_4Br)_2Zr_6Br_{18}B$ (6-18 type), one notices some similarities between these two structures. Like the face-centered lattice of $(K_4Br)_2Zr_6Br_{18}B$, the clusters in $Na_3Zr_6Br_{16}B$ also have a quasi-face-centered arrangement. The four Na atoms (Na2) in the same quadrant have a roughly tetrahedral arrangement as well. The difference is that there is not an isolated Br atom to hold these Na atoms together. Owing to the bridging Br^{a-a} atoms, the

Table 16. Important bond distances (Å) and angles (°) in $Na_3Zr_6Br_{16}B$

d(Zr-Zr)			d(Zr-Br^a)		
Zr1-Zr2	x1[a]	3.278(4)	Zr3-Br6	x1	2.838(4)
	x1	3.286(4)	d(Zr-Br^{a-a})		
Zr1-Zr3	x1	3.296(4)	Zr1-Br7	x1	2.955(4)
	x1	3.289(4)	Zr2-Br7	x1	2.950(5)
Zr2-Zr3	x1	3.301(4)	$\bar{d}$		2.952
	x1	3.290(4)	d(Na-Br)		
$\bar{d}$		3.290	Na1-Br6	x1	2.80(1)
d(Zr-B)			-Br6	x1	2.89(1)
Zr1-B	x1	2.319(3)	-Br7	x1	2.85(1)
Zr2-B	x1	2.323(3)	-Br8	x1	2.98(2)
Zr3-B	x1	2.337(3)	-Br5	x1	3.04(2)
$\bar{d}$		2.326	-Br2	x1	3.20(1)
d(Zr-Br^i)			$\bar{d}$	x1	2.96
Zr1-Br3	x1	2.677(5)	Na2-Br4	x1	2.76(3)
-Br4	x1	2.686(5)	-Br5	x1	2.96(3)
-Br5	x1	2.693(5)	-Br6	x1	3.00(3)
-Br8	x1	2.698(5)	-Br4	x1	3.02(3)
Zr2-Br1	x1	2.649(5)	-Br1	x1	3.06(3)
-Br2	x1	2.682(5)	-Br7	x1	3.27(3)
-Br5	x1	2.704(5)	$\bar{d}$	x1	3.01
-Br8	x1	2.700(5)			
Zr3-Br1	x1	2.683(5)			
-Br2	x1	2.697(5)	Br3-Zr1-Br4	x1	164.7(2)
-Br3	x1	2.679(5)	Br1-Zr2-Br2	x1	164.9(2)
-Br4	x1	2.710(5)	Br1-Zr3-Br2	x1	166.9(2)
$\bar{d}$	x1	2.688	Zr1-Br7-Zr2	x1	159.3(2)

[a] Number of times the distances and angles occur per atom

cavities are not as big as those in $(K_4Br)_2Zr_6Br_{18}B$. This may be one of the reasons why the isolated Br atoms are not present here. More importantly, the existence of these isolated Br atoms is not electronically favored in this case. However, when it does become electronically demanded as in the case of $(Cs_4Br)Zr_6Br_{16}B$, one will see that Nature has found her own way to create large enough sites to accommodate big $[Cs_4Br]^{3+}$ polycations.

$Cs_4Zr_6Br_{16}Be$

Synthesis: Over 90% yield of $Cs_4Zr_6Br_{16}Be$ was obtained in the reaction loaded as $Cs_4Zr_6Br_{15}Be$ and carried out at 830°C for 30 days. Nice brick-shaped crystals were also found in this reaction. The Guinier powder pattern looked the same as that of $Cs_3Zr_6Cl_{16}C$ except that lines from the bromide phase were shifted to lower angles. However, this reaction could not be repeated at either 830°C or 850°C, where a new 6-15 phase $Cs_{4+x}Zr_6Br_{15}Be$ formed. Therefore, two reactions loaded as $Cs_4Zr_6Br_{16}Be$ and $Cs_4Zr_6Br_{15}Be$, respectively, were tried at 750°C for two weeks. The products were loose, dull black powders. Their Guinier powder patterns looked similar to that of the target compound $Cs_4Zr_6Br_{16}Be$. However, the intensities and the positions of the lines were not exactly the same, and the products were not well crystallized either since the lines in their Guinier powder patterns were not very sharp. Hence, these products were reloaded and heated at 800°C for another two weeks. High yields of $Cs_4Zr_6Br_{16}Be$ (about 95%) were found in both of these reactions. That is to say, $Cs_4Zr_6Br_{16}Be$ is a low temperature phase relative to $Cs_{4+x}Zr_6Br_{15}Be$. It is possible that the temperature indicated by the temperature controller was 20°C higher than the real temperature in the first reaction or it was located in a lower temperature zone as every furnace has a certain temperature gradient. The product formed at 750°C was probably an intermediate phase. Since it was not well crystallized at 750°C and disappeared at 800°C, it may be worth repeating at 750°C with the aid of some vapor transporting agent, $AlBr_3$.

In the zirconium–chloride system, a single crystal structure study has been done on $Cs_3Zr_6Cl_{16}C$, a 15e$^-$ cluster phase. The Cs content was obtained from the structure refinement. The same structure type was also realized with B and Be as interstitials with unknown Cs content. When boron was used in the Cs-Zr-Br reactions, two more new phases were observed depending upon the stoichiometries loaded. Interestingly, neither of them has the same structure type as $Cs_3Zr_6Cl_{16}C$ or $Cs_4Zr_6Br_{16}Be$ has. The slightly lower Cs content gave the 6-15 structure type adopted by $Cs_3Zr_6Br_{15}C$ (6-15 type) and a higher Cs content, on the other hand, yielded a new 6-16 phase, $(Cs_4Br)Zr_6Br_{16}B$, which will be discussed later.

Single Crystal Study: Prior to the data collection, both the oscillation and the Weissenberg photos were taken, and a monoclinic cell, similar to that of $Cs_3Zr_6Cl_{16}C$, was confirmed. The data collection was performed on an ENRAF NONIUS CAD4 diffractometer. Since the lattice has the monoclinic symmetry, a hemisphere of data were collected. Tables 17 and 18 list all the important data collection and structure refinement parameters. The initial model was again

Table 17. Crystal data for $Cs_4Zr_6Br_{16}Be$

space group, Z	$P2_1/c$ (no. 14), 2
cell parameters[a]	
a (Å)	11.493(2)
b	12.465(2)
c	14.591(2)
β (deg.)	122.08(1)
V (Å^3)	1771.1(4)
crystal dimens. (mm)	0.06 x 0.12 x 0.38
octants measured	±h, k, ±l
2θ (max.), deg.	55
reflections	
measured	8449
observed (I/σ(I)>3.0)	3245
indep.	1897
abs. coeff. (Mo Kα, cm^{-1})	235.85
transm. coeff. range	0.51-1.00
R_{ave}, % (obs.)	4.0
no. variables	120
sec. extinct. coeff.	5.6(4)x10^{-8}
R, %	5.6
R_w, %	3.7

[a] Guinier data

Table 18. Positional and thermal parameters for $Cs_4Zr_6Br_{16}Be$

Atom	Psn.	x	y	z	$B_{eq}(Å^2)$
Zr1	4(e)	0.0824(2)	0.0941(2)	0.9048(2)	1.00(7)
Zr2	4(e)	0.0889(2)	0.1356(2)	0.1350(2)	1.06(7)
Zr3	4(e)	0.7897(2)	0.0957(2)	0.9008(2)	1.02(7)
Br1	4(e)	0.8560(2)	0.2140(2)	0.7821(2)	1.50(8)
Br2	4(e)	0.8645(2)	0.2362(2)	0.5388(2)	1.51(8)
Br3	4(e)	0.0116(2)	0.0436(2)	0.2627(2)	1.7(1)
Br4	4(e)	0.1923(2)	0.2381(2)	0.5432(2)	1.71(9)
Br5	4(e)	0.1972(2)	0.2009(2)	0.7969(2)	1.55(8)
Br6	4(e)	0.3411(2)	0.0442(2)	0.2683(2)	1.8(1)
Br7	4(e)	0.6637(2)	0.0016(2)	0.9953(2)	1.76(8)
Br8	4(e)	0.5431(2)	0.2109(2)	0.7823(2)	1.9(1)
Cs1	4(e)	0.5212(2)	0.2225(2)	0.5209(1)	3.44(8)
Cs2	4(e)	0.6975(2)	0.0223(1)	0.2969(2)	3.95(8)
Be	2(a)	0	0	0	2.2(8)

[a] U x 10^3

U_{11}[a]	U_{22}	U_{33}	U_{12}	U_{13}	U_{23}
15(1)	12(1)	12(1)	0(1)	8.0(9)	2(1)
14(1)	13(1)	12(1)	-1(1)	6(1)	-1.1(9)
13(1)	12(1)	14(1)	2(1)	7.3(9)	1(1)
20(1)	19(1)	20(1)	3(1)	12(1)	8(1)
18(1)	17(1)	20(1)	-5(1)	8(1)	3(1)
30(1)	21(1)	21(1)	-4(1)	18(1)	-3(1)
28(1)	19(1)	21(1)	9(1)	15(1)	5(1)
22(1)	18(1)	22(1)	4(1)	14(1)	10(1)
18(1)	21(1)	21(1)	-1(1)	6(1)	-7(1)
18(1)	25(1)	29(1)	5(1)	16(1)	9(1)
18(1)	27(2)	24(1)	8(1)	9(1)	6(1)
35(1)	64(1)	27(1)	-2(1)	13.1(9)	1(1)
62(1)	29(1)	74(1)	1(1)	46(1)	-3(1)
30(10)					

obtained from the direct methods provided by the SHELXS-86. The structure refinement went very smoothly and converged at R=5.6% and R_w=3.7% anisotropically. The occupancies of Cs1 and Cs2 refined to 0.989(4) and 0.995(4), respectively, and were fixed at unity in the final refinement. Based on the refinement, the compound has the $Cs_4Zr_6Br_{16}Be$ stoichiometry with $14e^-$ clusters.

Structure Description: The structure of $Cs_4Zr_6Br_{16}Be$ is similar to that of $Cs_3Zr_6Cl_{16}C$ except that the Cs positions in the former are fully occupied, while one of them in the latter is partially occupied. It can also be related to the structure of $Na_3Zr_6Br_{16}B$ in the sense that they are both layered compounds and have the same connectivity among the cluster units (Figure 24). The major difference is the size of the countercation. This is also the cause of the differences in lattice symmetry, the layer spacing as well as the orientation of the cluster units.

In order to accommodate large Cs^+ cations, the distance between the layers increases from 6.93 Å in $Na_3Zr_6Br_{16}B$ to 9.74 Å in $Cs_4Zr_6Br_{16}Be$. This change is realized by reducing the number of layers in the unit cell. Within the unit cell of $Na_3Zr_6Br_{16}B$, there are two cluster layers along the a direction (Figure 21) so that these can stack on to each other in ... ABAB... sequence. In $Cs_4Zr_6Br_{16}Be$, on the other hand, there is only one cluster layer in the unit cell. As a result, the layer packing repeats itself as ...AAA.... This packing sequence does not necessarily mean that the clusters are stacked right on top of each other. As shown in the drawing of Figure 24, owing to the 122° monoclinic

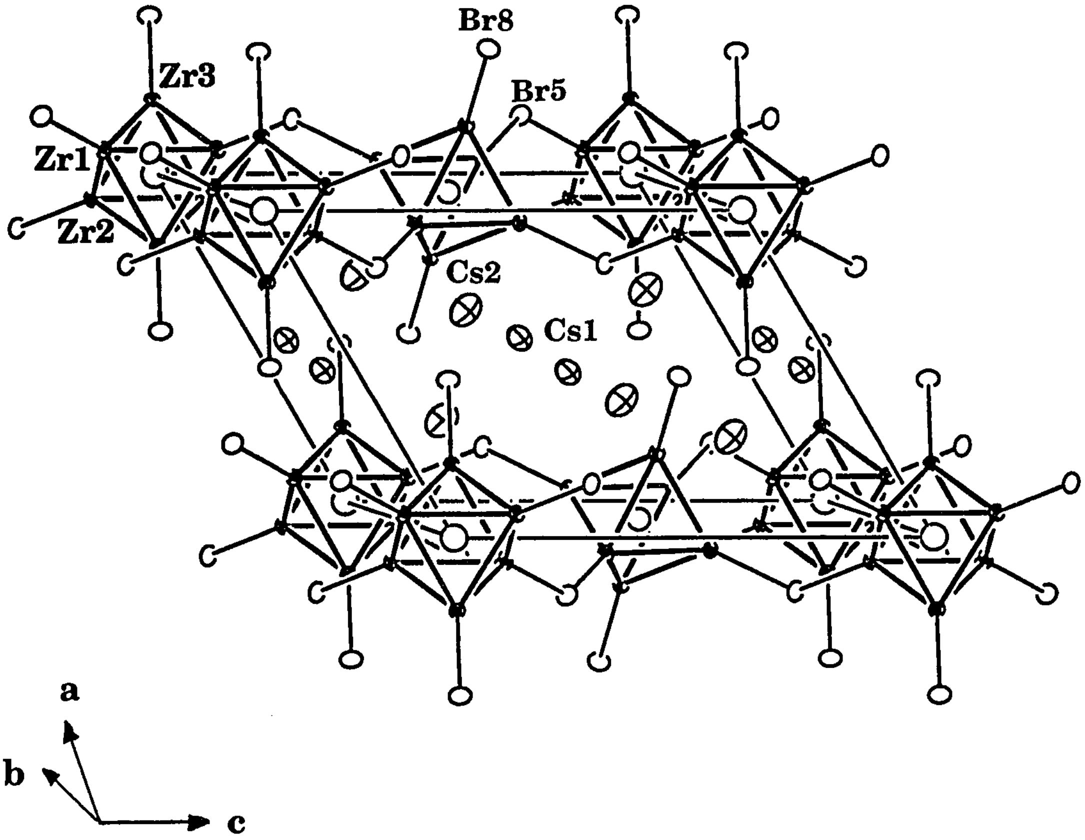

Figure 24. The unit cell view of $Cs_4Zr_6Br_{16}Be$, with the inner bromine atoms Br^i left out for clarity. The clusters are connected via four $Br^{a\text{-}a}$ around the waist of the clusters an the connections are extended throughout the bc plane to form two dimensional layers. The crossed ellipsoids represent the Cs^+ cations which are in between the cluster layers (70% probability)

angle, each cluster unit actually still sits in the void created by the adjacent clusters in the layers above and below. As discussed before, in $Na_3Zr_6Br_{16}B$ the trans Br^a-Zr-Zr-Br^a axes are basically perpendicular to the cluster layers in the ab plane and tilt 10° away from ac plane. In $Cs_4Zr_6Br_{16}Be$, however, the tilt angle from ac plane increases to approximately 30° for the clusters in column A and B, yet in the opposite directions (Figure 25). Furthermore, the Br^a-Zr-Zr-Br^a axes also tilt from the ab plane in the same direction by 5°. As a result, the bond angle at Br^{a-a} decreases from 159.3(2)° in $Na_3Zr_6Br_{16}B$ to 131.4(1)° in $Cs_4Zr_6Br_{16}Be$ (Table 19). The rotation or the larger tilt angles of the clusters in $Cs_4Zr_6Br_{16}Be$ contribute more space between the layers. In doing so, they also maximize the number of neighboring Br atoms around the Cs^+.

There are two crystallographically different Cs^+ sites in the lattice and they are both between the cluster layers. Cs1 is located midway between the cluster layers (Figure 24), while Cs2 is about 2 Å closer to the cluster layers. They each have 9 Br^- atoms around them, 2 Br^a, 1 Br^{a-a}, and 6 Br^i. The average Cs-Br distances for Cs1 and Cs2 are 3.800 Å and 3.841 Å, respectively, slightly longer than the summation of the corresponding crystal radii of the nine-coordinate Cs^+ and Br^-, 3.74 Å.

The cluster core has C_i symmetry and the average Zr-Zr distance is 3.355 Å, 0.056 Å longer than that in $Na_{3.9}Zr_6Cl_{16}Be$, 3.299 Å. The average Zr-Be distance is 2.372 Å which is 0.039 Å longer than the one in the corresponding chloride, 2.333 Å. As discussed in the previous chapter, the longer Zr-Zr and

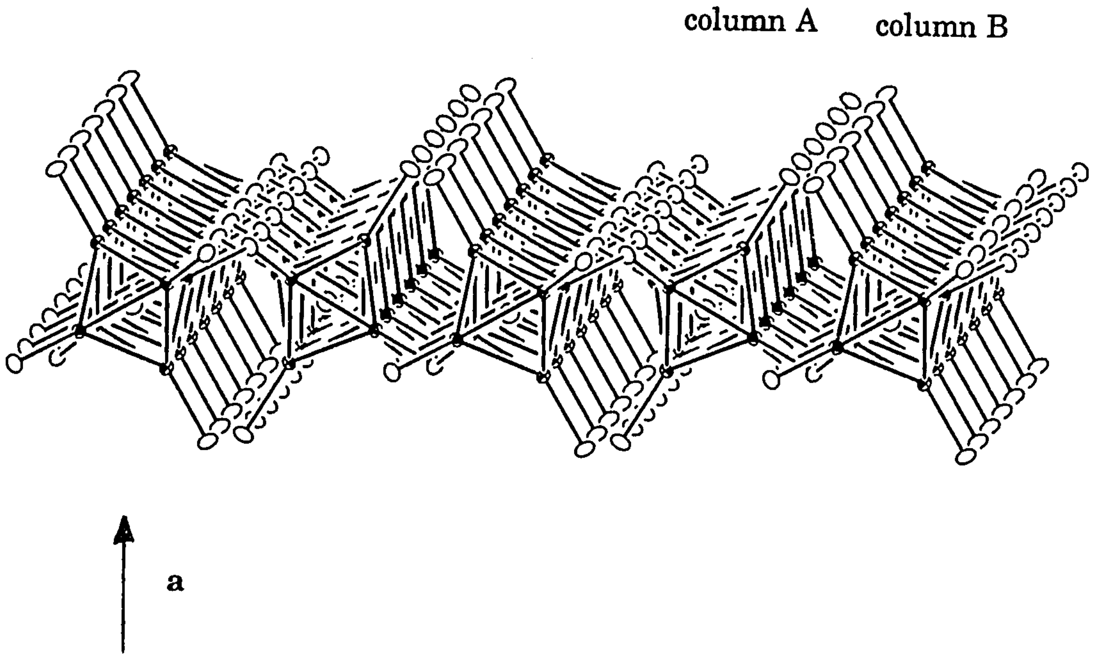

Figure 25. The ruffled layer in $Cs_4Zr_6Br_{16}Be$ with the terminal Br^a in trans positions. The clusters in column A and B tilt 30° from the ab plane, yet in alternate directions. The clusters in the same column are not connected directly, but rather through the clusters in the adjacent columns (70% probability)

Table 19. Important bond distances (Å) and angles (°) in $Cs_4Zr_6Br_{16}Be$

d(Zr-Zr)			d(Cs-Br)		
Zr1-Zr2	x1[a]	3.346(3)	Cs1-Br5	x1	3.540(3)
	x1	3.360(3)	-Br8	x1	3.689(3)
Zr1-Zr3	x1	3.334(3)	-Br1	x1	3.710(3)
	x1	3.372(3)	-Br8	x1	3.716(3)
Zr2-Zr3	x1	3.357(3)	-Br2	x1	3.818(3)
	x1	3.363(3)	-Br6	x1	3.835(3)
$\bar{d}$		3.355	-Br7	x1	3.912(3)
d(Zr-Be)			-Br4	x1	3.967(3)
Zr1-Be	x1	2.366(2)	-Br7	x1	4.018(3)
Zr2-B	x1	2.375(2)	$\bar{d}$		3.800
Zr3-B	x1	2.376(2)			
$\bar{d}$		2.372	Cs2-Br5	x1	3.584(3)
d(Zr-Br^i)			-Br8	x1	3.722(3)
Zr1-Br1	x1	2.695(3)	-Br8	x1	3.746(3)
-Br3	x1	2.699(3)	-Br4	x1	3.801(3)
-Br4	x1	2.709(3)	-Br1	x1	3.818(3)
-Br7	x1	2.746(3)	-Br6	x1	3.899(3)
Zr2-Br2	x1	2.708(3)	-Br3	x1	3.907(3)
-Br3	x1	2.708(3)	-Br2	x1	4.007(3)
-Br4	x1	2.716(3)	-Br7	x1	4.086(3)
-Br6	x1	2.738(3)	$\bar{d}$		3.841
Zr3-Br1	x1	2.675(3)			
-Br2	x1	2.709(3)			
-Br6	x1	2.730(3)			
-Br7	x1	2.737(3)	Br3-Zr1-Br4	x1	166.0(1)
$\bar{d}$		2.713	Br2-Zr2-Br6	x1	166.3(1)
			Br2-Zr3-Br6	x1	166.1(1)
d(Zr-Br^a)			Zr1-Br5-Zr2	x1	131.4(1)
Zr3-Br8	x1	2.807(3)	Zr1-Zr2-Zr1	x2	89.78(7)
d(Zr-Br^{a-a})			Zr2-Zr1-Zr3	x1	60.45(6)
Zr1-Br5	x1	2.863(3)		x1	59.95(6)
Zr2-Br5	x1	2.857(3)	Zr1-Zr2-Zr3	x1	60.41(6)
$\bar{d}$		2.860		x1	59.60(6)

[a] Number of times the distances and angles occur per atom

Zr-Be bonds are mainly caused by the size difference between Br^- (1.82 Å) and Cl^- (1.67 Å). The $Zr-Br^a$ distance is 2.807(3) Å, shorter than that of $Zr-Br^{a-a}$, 2.863(3) Å and 2.857(3) Å.

$(Cs_4Br)Zr_6Br_{16}B$

Synthesis: This phase was first seen as a major product in the reaction loaded with $Cs_2Zr_6Br_9B$ stoichiometry, but it was not observed at all in the reaction loaded as $CsZr_6Br_9B$. $Cs_{3.4}Zr_6Br_{15}B$ appeared to be the dominant product in the second reaction, indicating that the phase found in the first reaction must contain more Cs than $Cs_{3.4}Zr_6Br_{15}B$ does. Therefore, another reaction was loaded as $Cs_4Zr_6Br_{15}B$. As expected, about 90% of the target phase was found in this reaction. Well grown crystals, however, were obtained from the reaction loaded as $Cs_8Zr_6Br_{20}B$, aimed at the synthesis of the face-centered-cubic phase $(Cs_4Br)_2Zr_6Br_{18}B$. It turned out that the limit is Rb^+ for this cubic phase, and $(Cs_4Br)_2Zr_6Br_{18}B$ does not form at all. Instead, the new 6-16 phase and Cs_2ZrBr_6 formed. The excess CsBr or the Cs_2ZrBr_6 probably served as flux to help the crystal growth. The Guinier powder pattern did not look like that of any known cluster phases, indicating the discovery of a new phase.

Structure Determination: Data collection was performed on an ENRAF NONIUS CAD4 diffractometer. The 25 reflections located by program SEARCH could be indexed in a primitive tetragonal cell. Two octants of data were collected with an ω-θ scan mode. Other information about data collection and structure refinement results is listed in Table 20. The only extinction condition

Table 20. Crystal data for $(Cs_4Br)Zr_6Br_{16}B$

space group, Z	$P\bar{4}2_1m$ (no. 113), 2
cell parameters[a]	
a (Å)	12.5482(7)
c	11.5610(9)
V (Å^3)	1820.4(2)
crystal dimens. (mm)	0.05 x 0.09 x 0.22
octants measured	h, k, ±l
2θ (max.), deg.	50
reflections	
measured	3496
observed ($I/\sigma(I)>3.0$)	1781
indep.	992
abs. coeff. (Mo Kα, cm^{-1})	240.36
transm. coeff. range	0.52-1.00
R_{ave}, % (obs.)	4.2
no. variables	77
sec. extinct. coeff.	2.5(3) x 10^{-8}
R, %	4.3
R_w, %	3.2

[a] Guinier data

found in the data set was k=2n+1 for 0k0. In tetragonal lattice symmetry, there are only two possible space groups fulfilling this extinction condition, namely $P\bar{4}2_1m$ (No. 113) and $P42_12$ (No. 90). Both of them are acentric. The space group $P\bar{4}2_1m$, was tried first, and its correctness was later proven by the successful refinement. An empirical absorption correction was applied according to three averaged ψ-scan measurements. The observed data ($I>3\sigma$) were merged in the corresponding point group $\bar{4}m2$ with R_{ave}=4.2%. The initial model was obtained by the direct methods provided by the SHELXS-86 package. The assignment of the atoms was done according to the peak heights and the corresponding bond distances. All the atoms could be located in the initial model. The isotropic refinement converged at R=6.8% and R_w=5.0%, and the anisotropic refinement went smoothly and converged with R=5.2% and R_w=3.8%. The other enantiomer was checked and the refinement converged with R=4.3% and R_w=3.2%. Since this enantiomer has the lower R factors, it is considered the correct one. The occupancy of the Cs position refined to 1.008(5) and was fixed at unity in the final refinement. According to the refinement, this phase has the empirical formula of $Cs_4Zr_6Br_{17}B$. The atom positions and the anisotropic thermal parameters are compiled in Table 21. In this compound, the interstitial element boron is at a (0, 1/2, z) type position. Since boron is very light and only contributes 5 out of 1060 electrons in the unit cell, the refined positional and thermal parameters have relatively large standard deviations, but it did not refine off the center of the cluster (0, 1/2, 0.163) by 2σ.

Table 21. Positional and thermal parameters for $(Cs_4Br)Zr_6Br_{16}B$

Atom	Psn.	x	y	z	$B_{eq}(Å^2)$
Zr1	4(e)	0.4064(2)	x + 1/2	0.6951(3)	1.09(9)
Zr2	4(e)	0.4065(2)	x + 1/2	0.9811(3)	1.05(8)
Zr3	4(e)	0.1314(1)	x + 1/2	0.1595(4)	1.05(7)
Br1	2(c)	0	1/2	0.8301(6)	1.5(1)
Br2	4(e)	0.2946(2)	x + 1/2	0.1636(4)	1.66(8)
Br3	8(f)	0.2437(2)	0.0451(2)	0.6776(3)	1.8(1)
Br4	8(f)	0.2932(2)	x + 1/2	0.5254(3)	1.8(1)
Br5	2(c)	0	1/2	0.4929(6)	1.8(1)
Br6	8(f)	0.2418(2)	0.0409(2)	0.0005(3)	1.6(1)
Br7	4(e)	0.2881(2)	x + 1/2	0.8383(4)	1.56(8)
Br8	2(b)	0	0	1/2	3.2(2)
Cs	8(f)	0.2206(1)	0.0229(1)	0.3371(2)	3.31(9)
B	2(c)	0	1/2	0.178(8)	3(1)

[a] U x 10^3

U_{11}[a]	U_{22}	U_{33}	U_{12}	U_{13}	U_{23}
15(1)	U_{11}	12(2)	2(2)	-1(1)	U_{13}
14(1)	U_{11}	12(2)	-2(2)	0(1)	U_{13}
12.8(9)	U_{11}	14(2)	-4(1)	2(1)	U_{13}
26(2)	U_{11}	6(3)	9(2)	0	0
22(1)	U_{11}	19(2)	-5(2)	-1(2)	U_{13}
21(1)	27(1)	20(2)	7(1)	-5(2)	-4(1)
28(2)	U_{11}	13(2)	-7(2)	-8(2)	U_{13}
27(2)	U_{11}	16(3)	7(3)	0	0
20(2)	19(2)	23(2)	1(1)	10(1)	4(1)
21(1)	U_{11}	17(2)	-10(2)	3(2)	U_{13}
42(2)	U_{11}	39(4)	0	0	0
51(1)	35(1)	40(1)	1(1)	15(1)	0(1)
40(10)					

Structure Description: This new 6-16 phase is very rich structurally in the sense that it contains an extraordinary polycation $[Cs_4Br]^{3+}$, puckered or wavy cluster layers, and one dimensional tunnels. Similar to the polycation $[K_4Br]^{3+}$ in $(K_4Br)_2Zr_6Br_{18}B$ (6-18 type), the Cs atoms are held together by an isolated Br atom (Br8) to form a distorted tetrahedral polyhedron as indicated in Figure 26. Therefore, this new phase can be more accurately expressed as $(Cs_4Br)Zr_6Br_{16}B$. Compared with the $[K_4Br]^{3+}$ polycation in the lattice of $(K_4Br)_2Zr_6Br_{18}B$, which has an ideal tetrahedral arrangement, $[Cs_4Br]^{3+}$ in $(Cs_4Br)Zr_6Br_{16}B$ has an S_4 point symmetry. The environments of these two polycations are different as well. As shown in Figure 12 (6-18 type), $[K_4Br]^{3+}$ has 4 tetrahedrally arranged $[Zr_6Br^i{}_{12}B]Br^a{}_6$ cluster units as neighbors. On the other hand, $[Cs_4Br]^{3+}$ in $(Cs_4Br)Zr_6Br_{16}B$ has eight $[Zr_6Br^i{}_{12}B]Br^a{}_2Br^{a\text{-}a}{}_{4/2}$ clusters around it (Figure 27). As mentioned earlier, the stoichiometric reaction failed to give $(Cs_4Br)_2Zr_6Br_{18}B$, that is to say, the $[Cs_4Br]^{3+}$ is apparently too big to fit in the cavity created by this face-centered lattice. However, what one should keep in mind is that the increase in the size of cavities is by no means proportional to the increase of the number of neighboring clusters (from 4 to 8) because the cluster units in $(K_4Br)_2Zr_6Br_{18}B$ are well separated, while the clusters in $(Cs_4Br)Zr_6Br_{16}B$ are connected to one another by shared $Br^{a\text{-}a}$.

Compared with the other two 6-16 phases, namely, $Cs_4Zr_6Br_{16}Be$ and $Na_3Zr_6Br_{16}B$, the formation of the polycation in $(Cs_4Br)Zr_6Br_{16}B$ is not the only difference; the layer stacking, the orientation, and the connectivity of the

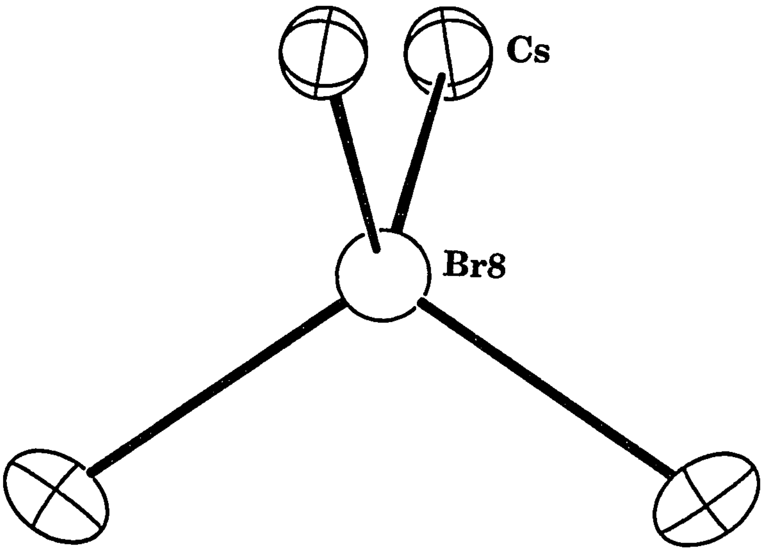

Figure 26. The polycation $[Cs_4Br]^{3+}$ in $(Cs_4Br)Zr_6Br_{16}B$. It has S_4 point symmetry. The picture is drawn with the $\bar{4}$ axis vertical (70% probability)

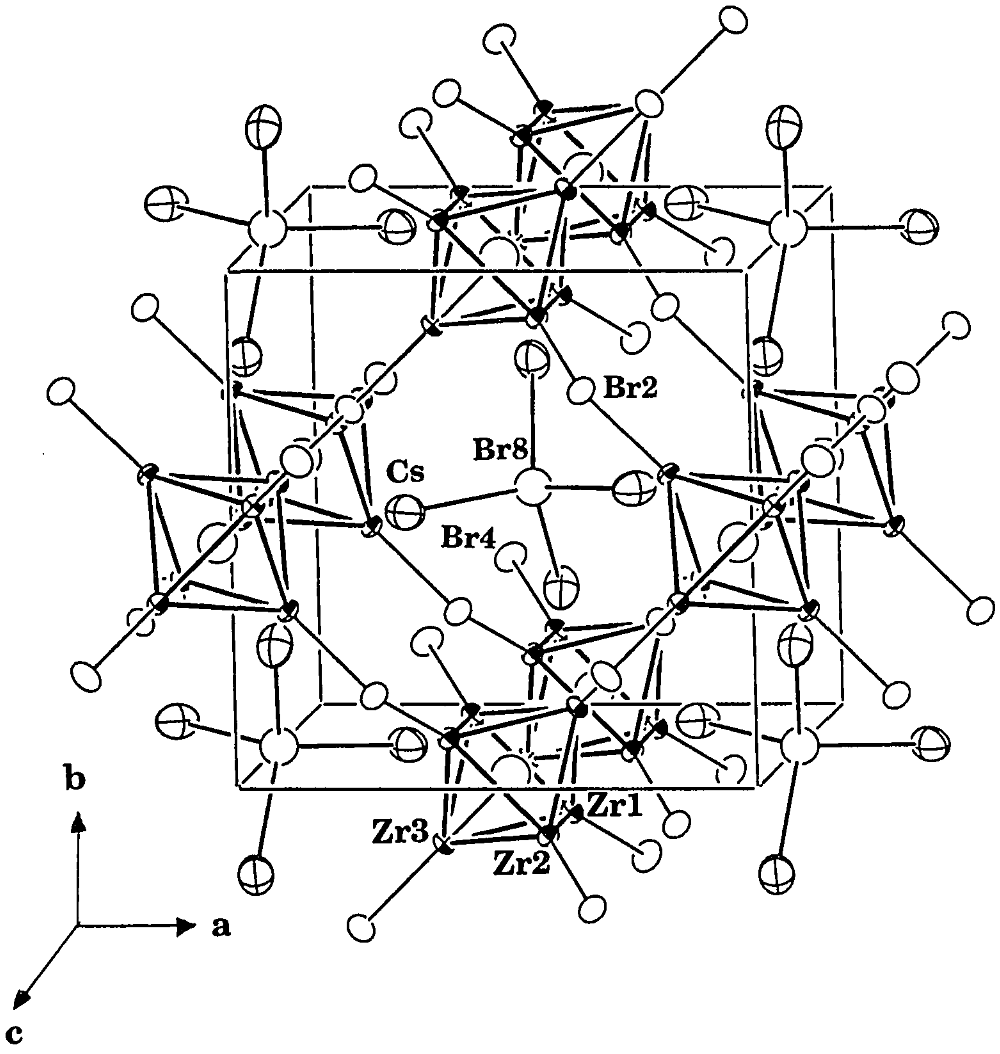

Figure 27. The tetragonal cell of $(Cs_4Br)Zr_6Br_{16}B$, showing that there are eight clusters around the central $[Cs_4Br]^{3+}$. The inner bromine atoms are omitted for clarity. The Cs^+ cations are drawn as crossed ellipsoids, and the Br^a and $Br^{a\text{-}a}$ as open circles (80% probability)

clusters as well as the relative positions of the clusters within the layers all show remarkable differences. In other words, it is a completely new type of 6-16 cluster phase. Within each cluster layer, there are still two kinds of columns of clusters along the b direction (Figure 28). Unlike those in $Na_3Zr_6Br_{16}B$ and $Cs_4Zr_6Br_{16}Be$, which are on the same level (Figures 21 and 24), the clusters in column A and B in the puckered layers in $(Cs_4Br)Zr_6Br_{16}B$ are 1.88 Å apart along the c direction. Owing to this kind of arrangement, the four $Br^{a\text{-}a}$ from the clusters in column A are shared by the clusters in column B in such a way that the two unshared Br^a atoms end up in the cis positions. On the contrary, the two terminal Br^a atoms in both $Na_3Zr_6Br_{16}B$ and $Cs_4Zr_6Br_{16}Be$ are in trans positions. As a result, the cluster layers in $(Cs_4Br)Zr_6Br_{16}B$ are very puckered or wavy. The clusters in the same column are not connected directly, but rather through the clusters in the adjacent columns. In $(Cs_4Br)Zr_6Br_{16}B$, the cluster layers are stacked in an eclipsed fashion, i.e., ...AAAA... (Figure 29), while those in $Na_3Zr_6Br_{16}B$ and $Cs_4Zr_6Br_{16}Be$ are staggered (Figure 23). As seen in Figure 30 the eclipsed stack of the cluster layers in $(Cs_4Br)Zr_6Br_{16}B$ creates one-dimensional tunnels perpendicular to the layers. More interestingly, these tunnels are occupied by $[Cs_4Br]^{3+}$ polycations. The picture in Figure 30 shows a very good space filling capability of the large $[Cs_4Br]^{3+}$ cations in the network of $(Cs_4Br)Zr_6Br_{16}B$. This could be one of the reasons why the tetragonal structure is preferred over the monoclinic one. Similar to the $[K_4Br]^{3+}$ polycation, the presence of the isolated Br8 in the center of the Cs_4 tetrahedron

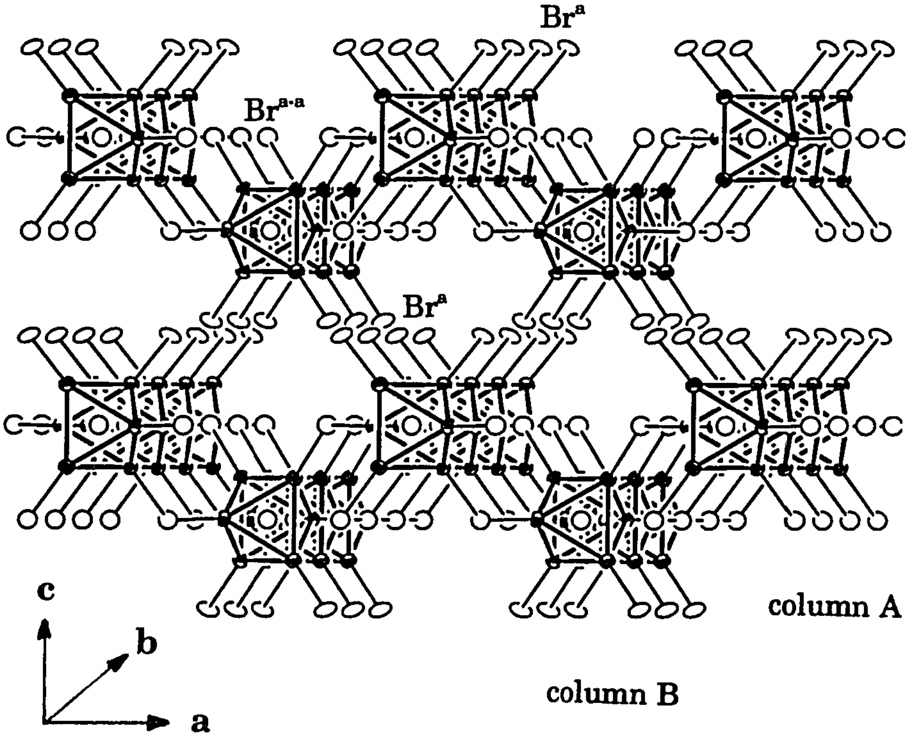

Figure 28. Two wavy cluster layers in $(Cs_4Br)Zr_6Br_{16}B$. The clusters in the same column are not connected directly, but rather through the clusters in the adjacent columns. Unlike those in $Na_3Zr_6Br_{16}B$ and $Cs_4Zr_6Br_{16}Be$, the terminal Br^a atoms are in cis positions in $(Cs_4Br)Zr_6Br_{16}B$ (90% probability)

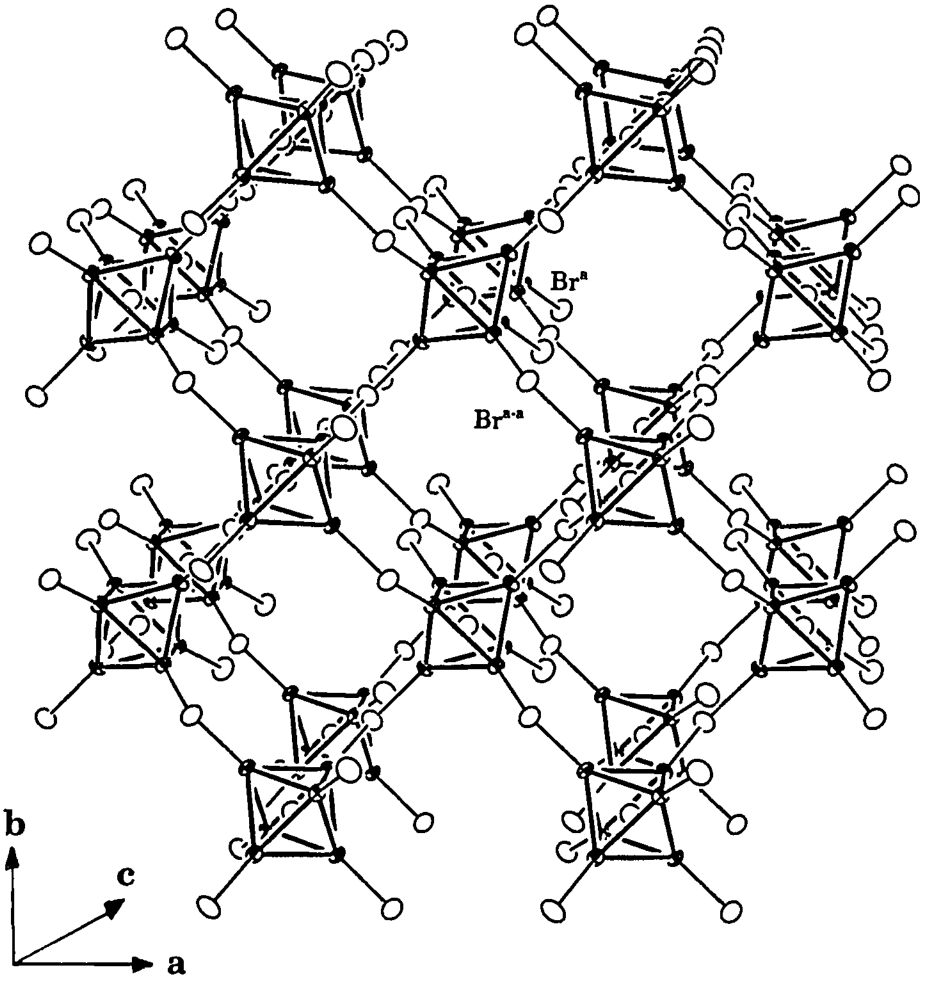

Figure 29. An approximately [001] projection of two cluster layers in ($Cs_4Zr_6Br_{16}B$), showing that the cluster layers are stacked along C in an eclipsed fashion, i.e., ...AA..., creating one-dimensional tunnels along the c direction. There are no connections between these layers, for the Br atoms between the layers are terminal ones (Br^a) (70% probability)

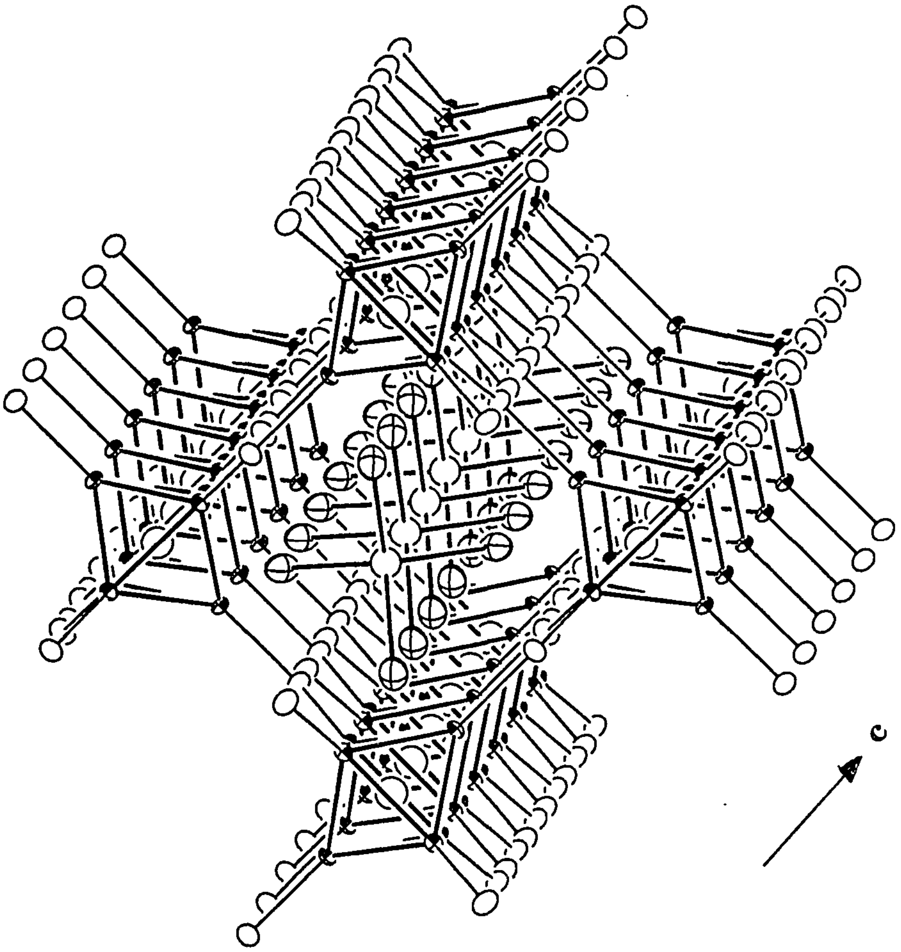

Figure 30. The extended view of the one-dimensional tunnel in $(Cs_4Br)Zr_6Br_{16}B$. The tunnel is normal to the cluster layer and occupied by the well separated $[Cs_4Br]^{3+}$ polycations as the nearest Cs-Cs distance is 4.552 Å (70% probability)

helps to reduce the repulsions among the Cs^+ cations, and it also takes one electron to give cluster units an optimal electron count, i.e., 14e.

Within 4.1 Å, there are 10 Br atoms around Cs, and the average Cs-Br distance in $(Cs_4Br)Zr_6Br_{16}B$ is 3.827 Å (Table 22), comparable to the sum of the corresponding crystal radii, 3.77 Å. As noted, the bond distance between the isolated Br (Br8) and Cs atom is only 3.360(2) Å. This feature rather than a problem is also observed in $(K_4Br)_2Zr_6Br_{18}B$. The less bonded Br (to Zr) usually have stronger interaction or shorter distances to the countercations. Since Br8 is not even bonded to a Zr atom and only has four Cs^+ neighbors, the Cs-Br8 distance should be expected to be short.

The cluster core has C_{2v} point symmetry. The average Zr-Zr distance is 3.308 Å and Zr-B distance is 2.34 Å. They are fairly comparable to those in $Na_3Zr_6Br_{16}B$, 3.290 Å and 2.326 Å, respectively. The Zr-Br^i distances are in the range of 2.670(5) Å–2.745(6) Å, shorter than that of Zr–Br^a, 2.807 Å. The longest distance is that between Zr and $Br^{a\text{-}a}$, 2.896(5) Å.

6-15 Type

Among the seven zirconium to bromine ratios in the framework, the 6-15 stoichiometry exhibits the richest structural versatility. The earlier investigations in the zirconium chloride system provided about twenty-five 6-15 type cluster phases.[16-17,30,39-41] Sharing the same local connectivity, $(Zr_6Z)Cl^i_{12}Cl^{a\text{-}a}_{6/2}$, they all form three dimensional networks. These 6-15 cluster phases can be classified into four distinctive structure types according to the

Table 22. Important bond distances (Å) and angles (°) in $(Cs_4Br)Zr_6Br_{16}B$

d(Zr-Zr)		
Zr1-Zr1	x1[a]	3.322(7)
-Zr2	x1	3.306(4)
-Zr3	x2	3.320(4)
Zr2-Zr2	x1	3.320(7)
Zr2-Zr3	x2	3.291(4)
$\bar{d}$		3.308
d(Zr-B)		
Zr1-B	x1	2.22(6)
Zr2-B	x1	2.47(7)
Zr3-B	x1	2.341(9)
$\bar{d}$		2.34
d(Zr-Br^{i})		
Zr1-Br3	x2	2.691(2)
-Br5	x1	2.731(6)
-Br7	x1	2.674(5)
Zr2-Br1	x1	2.745(6)
-Br6	x2	2.677(3)
-Br7	x1	2.670(5)
Zr3-Br3	x2	2.680(4)
-Br6	x2	2.691(5)
d(Zr-Br^{a})		
Zr1-Br4	x1	2.807(6)
d(Zr-Br$^{a\text{-}a}$)		
Zr2-Br2	x1	2.897(6)
Zr3-Br2	x1	2.896(5)
d(Cs-Br)		
Cs-Br8	x1	3.360(2)
-Br2	x1	3.619(4)
-Br4	x1	3.725(4)
-Br4	x1	3.749(4)
-Br7	x1	3.900(4)
-Br6	x1	3.908(4)
-Br3	x1	3.955(4)
-Br3	x1	4.008(4)
-Br1	x1	4.013(4)
-Br5	x1	4.032(4)
$\bar{d}$		3.827
d(Br-Br)[b]		
Br1-Br2	x2	3.646(4)
Br2-Br3	x2	3.662(4)
-Br6	x2	3.681(5)
	x2	3.733(5)
-Br7	x1	3.760(7)
Br3-Br3	x1	3.749(5)
-Br4	x1	3.670(4)
-Br6	x1	3.735(4)
-Br7	x1	3.764(4)
-Br8	x1	3.725(3)
Br4-Br5	x1	3.676(4)
-Br7	x1	3.619(6)
Br6-Br7	x1	3.637(4)
Br3-Zr1-Br3	x1	167.4(2)
Br1-Zr2-Br7	x1	165.3(2)
Br6-Zr2-Br6	x1	165.0(2)
Br3-Zr3-Br6	x1	165.7(1)
Zr2-Br2-Zr3	x1	132.3(2)
Zr1-Zr1-Zr2	x1	90.0(1)
Zr1-Zr1-Zr3	x2	59.99(6)
Zr3-Zr1-Zr3	x2	89.2(1)
Zr2-Zr1-Zr3	x1	59.6(1)
Cs-Br8-Cs	x2	111.85(9)
	x2	108.29(4)

---

[a] Number of times the distances and angles occur per atom

[b] d(Br-Br) < 3.8 Å

local geometry of the bridging bonds Zr-Cl^{a-a}-Zr, namely, the length of the shortest circular bonding path as well as the linkage among the six first-bonding-sphere cluster units.[18,69] Although they exhibit the same local connectivity around each cluster unit, these different structures cannot be interconverted without breaking and rearranging the bridge bonds. As noted in Table 23, these four types form a nice transition in terms of the local bridging arrangement. All the bridge bonds are linear in Nb_6F_{15}, whereas Ta_6Cl_{15} contains only nonlinear bridge atoms.

Earlier work in the zirconium bromide system provided one 6-15 type cluster phase, i.e., $CsZr_6Br_{15}Fe$ [16] which has the $CsNb_6Cl_{15}$ [39] parent structure. The recent investigations in the zirconium–bromide system, however, have not only offered seven more new 6-15 zirconium bromide cluster phases but have also contributed one more new structure type to the systems. Among these new 6-15 phases, $Rb_3Zr_6Br_{15}Be$ and $K_3Zr_6Br_{15}Be$ are isostructural with $K_3Zr_6Cl_{15}Be$ which has a distorted network of $K_2Zr_6Cl_{15}B$,[40] while $Cs_{3.4}Zr_6Br_{15}B$ and $Cs_3Zr_6Br_{15}C$ adopt the structural framework of $Cs_3(ZrCl_5)Zr_6Cl_{15}Mn$ with the replacement of $(ZrCl_5)^-$ by Cs^+ cations. $Rb_5Zr_6Br_{15}Be$, $Rb_4Zr_6Br_{15}B$ and $Cs_{4.6}Zr_6Br_{15}Be$ have their own structural framework that does not belong to any of the 6-15 structure types found in the zirconium or other early transition metal halide systems. This section will focus on the single crystal study of $Rb_3Zr_6Br_{15}Be$, $Cs_{3.4}Zr_6Br_{15}B$, $Cs_3Zr_6Br_{15}C$, $Rb_5Zr_6Br_{15}Be$, and $Cs_{4.6}Zr_6Br_{15}Be$.

Table 23. Distribution of $X^{a\text{-}a}$ bridges in $Zr_6X_{12}(Z)X_{6/2}$-type structures

		$X^{a\text{-}a}$ Bridge Type, %		Criteria		
Structure Type	Space Group	Linear	Bent	Ring Size[a]	no. of FBS[b] Clusters so Linked	Others
Nb_6F_{15}	Im3m	100	0	4	4	$Zr_6Cl_{15}Co$, $Zr_6Cl_{15}Ni$, $LiZr_6Cl_{15}Fe$, $Li_2Zr_6Cl_{15}Mn$, $Cs_3(ZrCl_5)Zr_6Cl_{15}Mn^*$ $Cs_3(ZrCl_5)Zr_6Cl_{15}B^*$, $Cs_3Zr_6Br_{15}C^*$, $Cs_{3.4}Zr_6Br_{15}B^*$, $Re_6S_7Br_4^*$,[13] $Re_6Se_7Br_4^{*}$[13]
$K_2Zr_6Cl_{15}B$	Cccm	33	67	4	2,3	$K_2Zr_6Cl_{15}Be$, $K_2Zr_6Cl_{15}B$, $K_3Zr_6Br_{15}Be^*$, $Rb_3Zr_6Br_{15}Be^*$, Nb_6I_{11},[9-10] $Ba_2Re_6S_{11}$,[70] $Sr_2Re_6Se_{11}$,[70]
$CsNb_6Cl_{15}$	Pmma	17	83	3	–	$KZr_6Cl_{15}C$, $RbZr_6Cl_{15}C$, $CsZr_6Cl_{15}C$, $CsKZr_6Cl_{15}B^*$, $Rb_2Zr_6Cl_{15}B^*$, $CsRbZr_6Cl_{15}B^*$, $KZr_6Cl_{15}N$, $CsZr_6Br_{15}Fe$,
Ta_6Cl_{15}	Ia3d	0	100	4	2	$Zr_6Cl_{15}N$, $Na_{0.5}Zr_6Cl_{15}C$, $Na_{0.8}Hf_6Cl_{15}B$,[71] $Na_{1.2}Hf_6Cl_{15}B^{*}$[71]
$Rb_5Zr_6Br_{15}Be$	$P6_322$	0	100	4	3	$Cs_{4.7}Zr_6Br_{15}Be$, $Rb_4Zr_6Br_{15}B$

a y in $(\text{—}Zr_6\text{—}X^{a\text{-}a})_y$.

b First bonding sphere (FBS) to a central cluster.

* The compounds with the structures related to, yet distorted from, the parent structure.

Furthermore, the similarities and the differences among these three 6-15 structure types will be discussed.

$RB_3ZR_6BR_{15}BE$

Synthesis: $Rb_3Zr_6Br_{15}Be$ was firstly observed in the reaction loaded with the $Rb_4Zr_6Br_{16}Be$ stoichiometry and carried out at 820°C. The Guinier powder pattern of the product of this reaction is very similar to that of $K_3Zr_6Cl_{15}Be$ and could be indexed accordingly. In fact, $(Rb_4Br)_2Zr_6Br_{18}Be$ (6-18 type) was seen in the powder pattern as well. A high yield (>95%) of $Rb_3Zr_6Br_{15}Be$ phase was obtained when the reaction was loaded stoichiometrically. The same structure type was also realized with K^+ as countercations with Guinier lattice constants a=17.143 Å, b=11.9115(7) Å, c=14.716(2) Å, β=92.424(9)°, and V=3002.2(5) Å^3.

Single Crystal Study: The single crystals of $Rb_3Zr_6Br_{15}Be$ were obtained in the reaction loaded as $Rb_4Zr_6Br_{16}Be$. Data collection was conducted on an ENRAF NONIUS CAD4 diffractometer. The 25 peaks found in the random search could be indexed with a primitive cell which was transformed to the C-centered monoclinic cell by the cell reduction program TRANS. A hemisphere of data were collected accordingly. An empirical absorption correction was made by using three averaged ψ-scan measurements. The intensity statistics indicated the existence of a centric symmetry. Moreover, the extinction conditions observed (h,l=2n+1 for h0l and k=2n+1 for 0k0) were the same as those required for the isostructural $K_3Zr_6Cl_{15}Be$. After the systematically absent and weak reflections ($I<3\sigma$) were rejected, data were averaged in the point group 2/m with R_{ave}=5.2%.

The positional parameters refined for $K_3Zr_6Cl_{15}Be$ were utilized as the initial model. The isotropic refinement was carried out for all the positions except for that of interstitial element Be and converged at R=7.0% and R_w=6.8%. The secondary extinction coefficient and the isotropic thermal ellipsoid of Be were refined after anisotropic refinement was conducted for all Zr, Br and Rb atoms. The final refinement converged with R=4.6% and R_w=4.2%. The occupancies of the two Rb positions refined to 0.982(8) and 0.982(6), therefore, they were fixed at unity in the final refinement. The final difference Fourier map was basically flat with the largest peak as 1.88 e/Å^3, 1.6 Å from Br1 position. The other important data collection and structure refinement results are compiled in Table 24. The refined positional and anisotropic thermal parameters are listed in Table 25.

Structure Description: As mentioned earlier, $Rb_3Zr_6Br_{15}Be$ is isostructural with $K_3Zr_6Cl_{15}Be$. Its structure can be described as a pseudo two-dimensional network along b and c directions. As illustrated in Figure 31, cluster units with the same x coordinate for Be form rectangular layers on the bc plane by sharing the bridge Br atoms ($Br^{a\text{-}a}$) around the waist. The stacking of the neighboring layers is staggered so that each cluster sits in the cavity created by the clusters in the layers above and below. In other words, the layer packing is ...ABAB.... The structure features described so far are rather similar to those found in $Cs_4Zr_6Br_{16}Be$ (6-16 type). Due to the relative positions and the orientations of the cluster units within the layers, the Zr-$Br^{a\text{-}a}$-Zr bonds are bent

Table 24. Crystal data for $Rb_3Zr_6Br_{15}Be$

space group, Z	C2/c (no. 15), 4
cell parameters[a]	
a (Å)	17.232(1)
b	12.0407(6)
c	14.7067(8)
β (deg.)	92.834(6)
V (Å^3)	3047.8(3)
crystal dimens. (mm)	0.11 x 0.12 x 0.16
octants measured	±h, k, ±l
2θ (max.), deg.	50
reflections	
measured	6052
observed (I/σ(I)>3.0)	2958
indep.	1961
abs. coeff. (Mo Kα, cm^{-1})	260.64
transm. coeff. range	0.54–1.00
R_{ave}, % (obs.)	5.2
no. variables	113
sec. extinct. coeff.	1.170(4) x 10^{-7}
R, %	4.6
R_w, %	4.2

[a] Guinier data

Table 25. Positional and thermal parameters for $Rb_3Zr_6Br_{15}Be$

Atom	Psn.	x	y	z	B_{eq}(Å^2)
Zr1	8(f)	0.13742(9)	0.1391(1)	0.4989(1)	0.82(6)
Zr2	8(f)	0.30097(9)	0.1543(1)	0.6319(1)	0.80(6)
Zr3	8(f)	0.6901(1)	0.1174(1)	0.0949(1)	0.87(6)
Br1	8(f)	0.8106(1)	0.0310(1)	0.6019(1)	1.44(7)
Br2	8(f)	0.5504(1)	0.2254(1)	0.1030(1)	1.44(7)
Br3	8(f)	0.2670(1)	0.2172(1)	0.2452(1)	1.29(7)
Br4	8(f)	0.3777(1)	0.0047(1)	0.0427(1)	1.66(7)
Br5	4(a)	0	0	0	1.9(1)
Br6	8(f)	0.3754(1)	0.9570(1)	0.2882(1)	1.42(7)
Br7	8(f)	0.3230(1)	0.4828(1)	0.3526(1)	1.22(7)
Br8	8(f)	0.0665(1)	0.2231(1)	0.3459(1)	1.53(7)
Rb1	4(e)	0	0.9453(2)	1/4	3.3(1)
Rb2	8(f)	0.1165(1)	0.2427(2)	0.0624(1)	2.98(9)
Be	4(d)	1/4	1/4	1/2	1.8(6)

[a] U x 10^3

U_{11}[a]	U_{22}	U_{33}	U_{12}	U_{13}	U_{23}
7.7(9)	12.2(8)	11.1(7)	-3.2(6)	-0.9(6)	-0.2(6)
10.2(9)	10.7(7)	9.4(7)	-1.2(6)	-1.1(6)	0.8(6)
10.7(9)	11.0(8)	11.4(8)	1.0(7)	0.7(6)	1.8(6)
20(1)	15.7(9)	20(1)	-5.6(7)	3.6(7)	-6.6(7)
13(1)	20.0(9)	22.2(9)	2.4(7)	4.9(7)	3.5(7)
23(1)	15.3(8)	10.4(8)	1.4(7)	-0.7(7)	1.8(6)
28(1)	20(1)	15.4(9)	-11.1(8)	-1.6(8)	0.3(7)
15(1)	23(1)	33(1)	11(1)	-1(1)	-3(1)
19(1)	19(1)	16.1(9)	2.8(7)	-1.2(7)	-7.5(6)
17(1)	13.9(8)	14.8(8)	-3.4(7)	-2.4(7)	5.2(6)
15(1)	24(1)	18.3(8)	-5.9(7)	-6.5(7)	7.3(7)
43(2)	43(2)	40(2)	0	16(1)	0
41(1)	26(1)	45(1)	-0(1)	-5(1)	2.2(9)
23(8)					

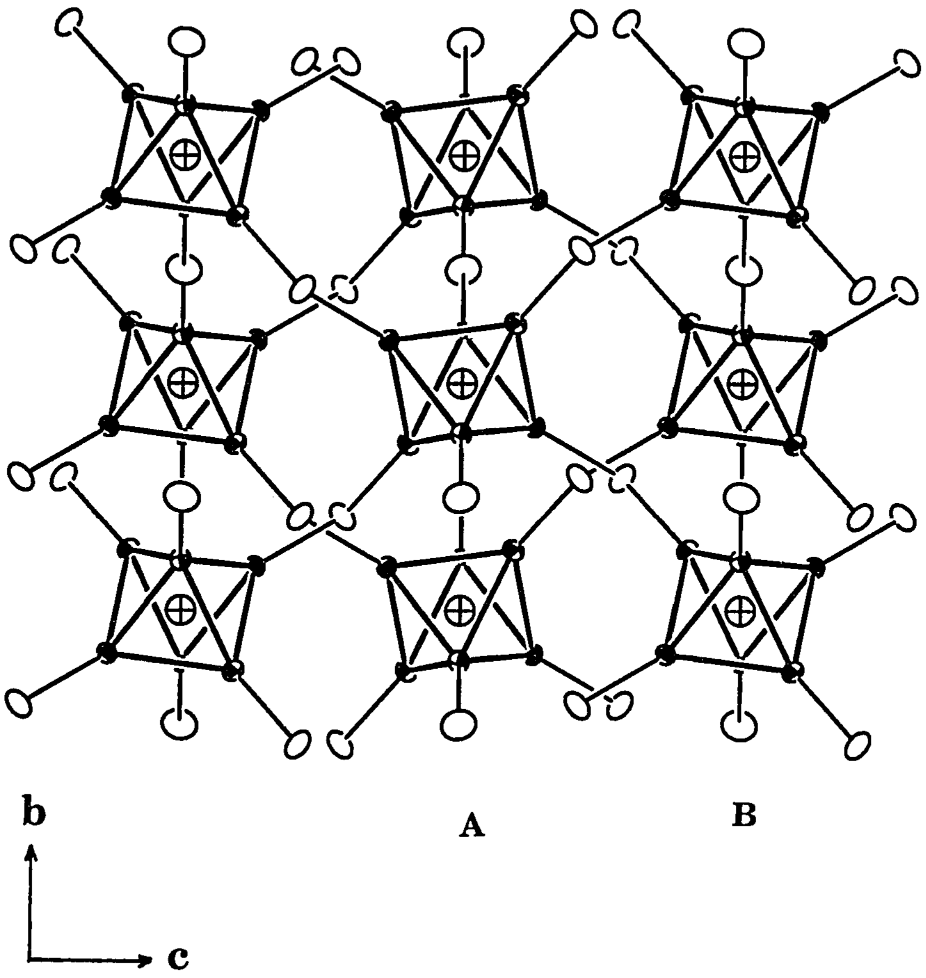

Figure 31. An [100] view of the structure of $Rb_3Zr_6Br_{15}Be$ with Br^i and Rb atoms omitted for clarity. (Zr_6Be) clusters are outlined and $Br^{a\text{-}a}$ atoms are drawn as open ellipsoids. The staggered layer packing is clearly shown (90% probability)

at 128.08(7)° angles in $Rb_3Zr_6Br_{15}Be$ (Table 26). The major difference between these two structure types is that the layers in $Rb_3Zr_6Br_{15}Be$ are connected via two other bridge Br atoms (Figure 32). The cluster layers in $Cs_4Zr_6Br_{16}Be$, on the other hand, are isolated from each other. Unlike the Zr-Br^{a-a}-Zr bonds within the layer, the Zr-Br^{a-a}-Zr bonds in between the layers are linear.

Figure 33 gives an extended view along the c axis. As noted, there are two different kinds of one-dimensional tunnels along this direction. The larger tunnel with a dumbbell shape has the Rb atoms in it. Figure 34 shows that each of these large tunnel contains six one-dimensional Rb arrays. Rb1 lies about 0.6 Å above and below Br5 along the b direction, whereas, Rb2 atoms move towards the cluster units. Figure 35 and Figure 36 give the local environment about the two Rb positions. As seen, each has four cluster units around it. The number of adjacent Br atoms, however, is different. The view in Figure 35 shows that there are 8 Br^i and 2 Br^{a-a} around Rb1 with C_2 local symmetry. Rb2, on the other hand, resides on a general position with 6 Br^i and 2 Br^{a-a} as close neighbors. The average Rb1-Br distance is 3.683(2) Å, comparable to the sum of the corresponding crystal radii (Br^-(VI),1.82 Å; Rb^+(X), 1.80 Å). The average Rb2-Br distance is 3.571(2) Å which is rather ideal for an 8-coordinate Rb^+ (Rb^+(VIII), 1.75 Å).

In $Rb_3Zr_6Br_{15}Be$, the Zr_6Be cluster core has the optimal 14e⁻ in its bonding orbitals. The $(Zr_6Be)Br^i_{12}Br^{a-a}_{6/2}$ cluster unit has a C_i point symmetry. The average Zr-Be distance is 2.376(2) Å, comparable to the one found in

Table 26. Important bond distances (Å) and angles (°) in $Rb_3Zr_6Br_{15}Be$

d(Zr-Zr)					
Zr1-Zr2	x1[a]	3.356(2)	-Br5	x2	3.7353(6)
	x1	3.349(2)	-Br7	x2	3.499(2)
Zr1-Zr3	x1	3.359(2)	-Br8	x2	3.786(3)
	x1	3.348(2)	$\bar{d}$		3.683
Zr2-Zr3	x1	3.375(2)	Rb2-Br1	x1	3.771(3)
	x1	3.376(2)	-Br2	x1	3.694(3)
$\bar{d}$		3.360	-Br3	x1	3.656(2)
d(Zr-Be)			-Br4	x1	3.415(2)
Zr1-Be	x1	2.355(2)	-Br5	x1	3.638(2)
Zr2-Be	x1	2.386(2)	-Br6	x1	3.387(3)
Zr3-Be	x1	2.388(2)	-Br7	x1	3.510(2)
$\bar{d}$		2.376	-Br8	x1	3.499(3)
d(Zr-Br^i)			$\bar{d}$		3.571
Zr1-Br1	x1	2.706(2)	d(Br-Br)[b]		
-Br2	x1	2.735(2)	Br1-Br5	x1	3.678(2)
-Br7	x1	2.692(2)	-Br6	x1	3.663(3)
-Br8	x1	2.702(2)	-Br7	x1	3.686(2)
Zr2-Br3	x1	2.691(2)	Br3-Br6	x1	3.687(2)
-Br4	x1	2.703(2)	-Br7	x1	3.674(2)
-Br7	x1	2.718(2)	-Br7	x1	3.496(2)
-Br8	x1	2.725(2)	Br4-Br6	x1	3.658(2)
Zr3-Br1	x1	2.738(2)	Br5-Br7	x1	3.660(2)
-Br2	x1	2.743(2)	Br6-Br8	x1	3.608(2)
-Br3	x1	2.711(2)	Br8-Br8	x1	3.547(3)
-Br4	x1	2.717(2)			
d(Zr-Br^{a-a})			Zr2-Zr1-Zr2	x1	90.75(5)
Zr1-Br5	x1	2.901(2)	Zr2-Zr1-Zr3	x1	60.37(4)
Zr2-Br6	x1	2.904(2)	Zr3-Zr1-Zr3	x1	90.8(5)
Zr3-Br6	x1	2.856(2)	Zr1-Zr2-Zr1	x1	89.25(5)
d(Rb-Br)			Zr1-Zr2-Zr3	x1	59.87(4)
Rb1-Br1	x2	3.844(2)	Zr1-Br5-Zr1	x1	180.00
-Br2	x2	3.553(2)	Zr2-Br6-Zr3	x1	128.07(7)

---

[a] Number of times the distances and angles occur per atom

[b] d(Br-Br) < 3.70 Å

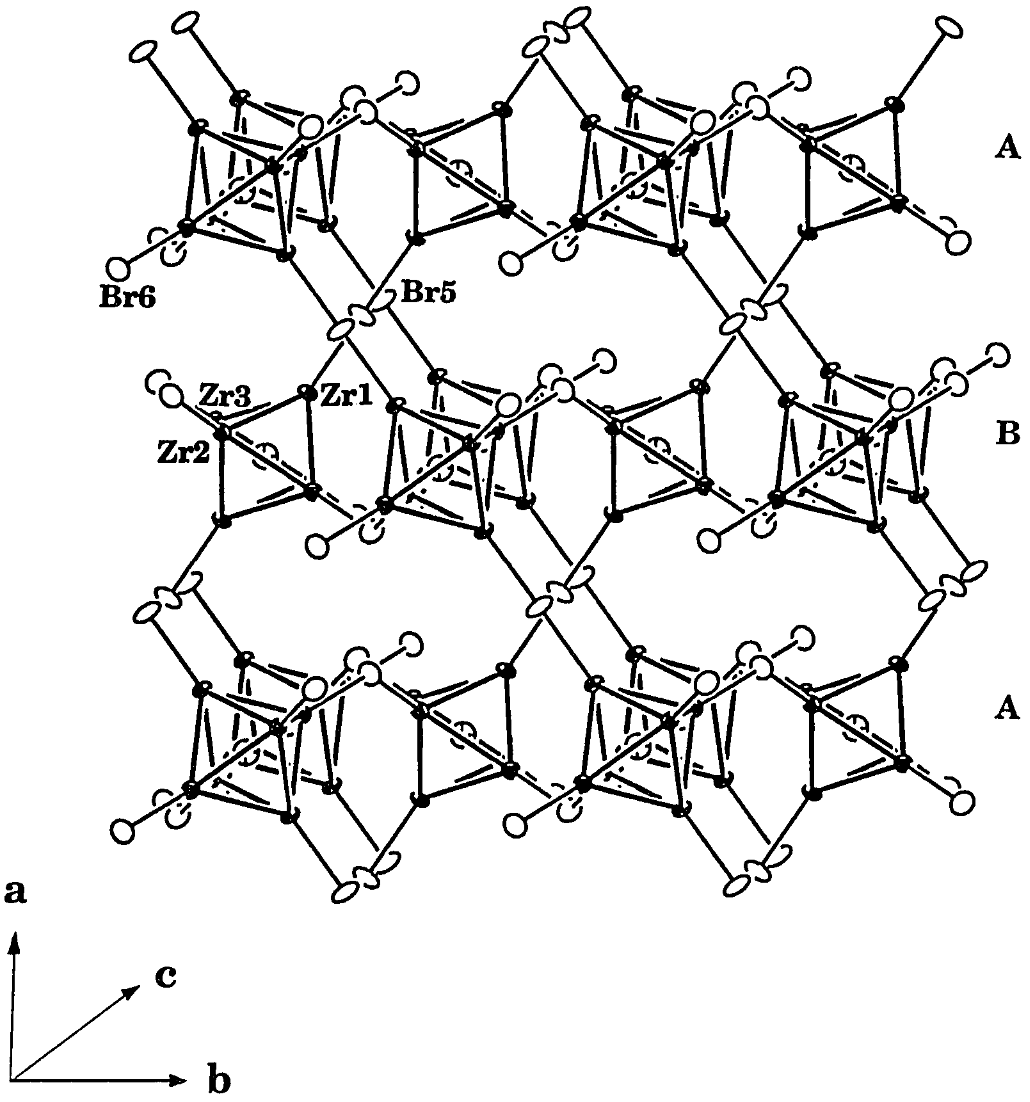

Figure 32. An approximately [001] view of the structure of $Rb_3Zr_6Br_{15}Be$ showing the layers are similar to those in $Cs_4Zr_6Br_{16}Be$, yet connected via linear $Br^{a\text{-}a}$ (90% probability)

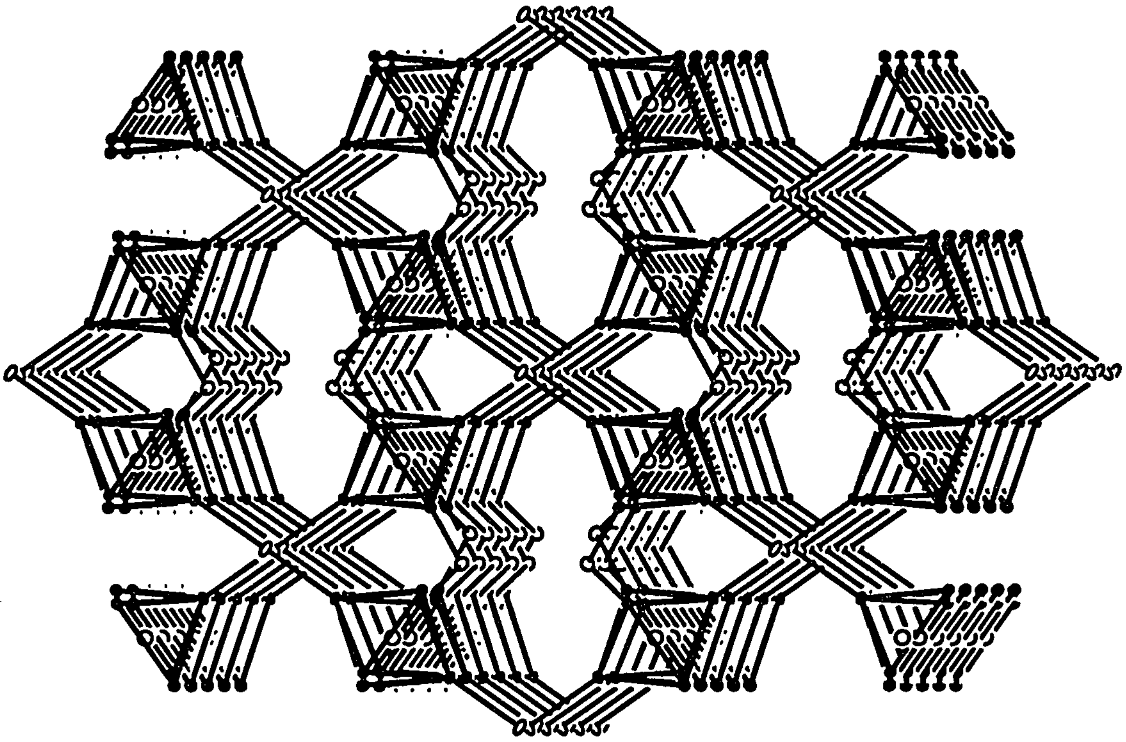

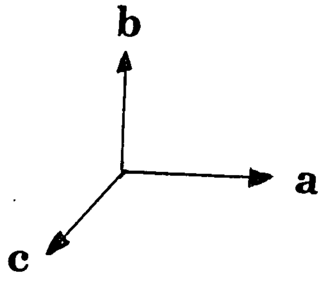

Figure 33. The extended view along the c direction showing two kind of tunnels in the three-dimensional framework of $Rb_3Zr_6Br_{15}Be$. The Br^i and Rb atoms are left out for clarity (50% probability)

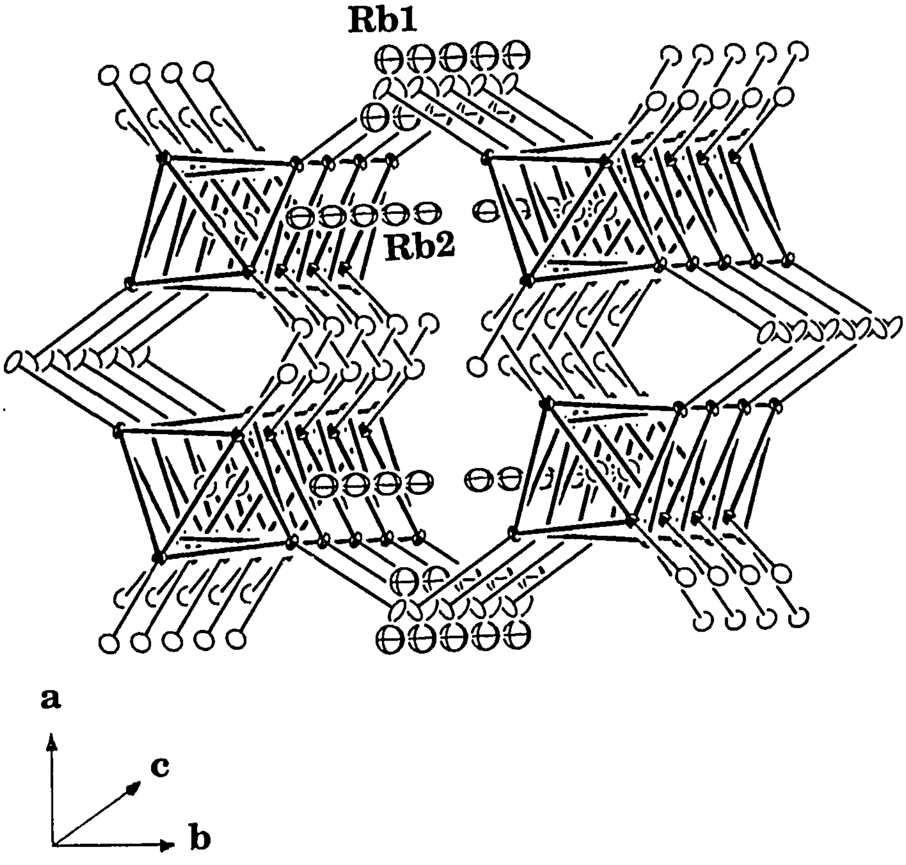

Figure 34. The dumbbell shaped tunnel occupied with Rb arrays. The Rb cations are drawn as crossed-ellipsoids (70% probability)

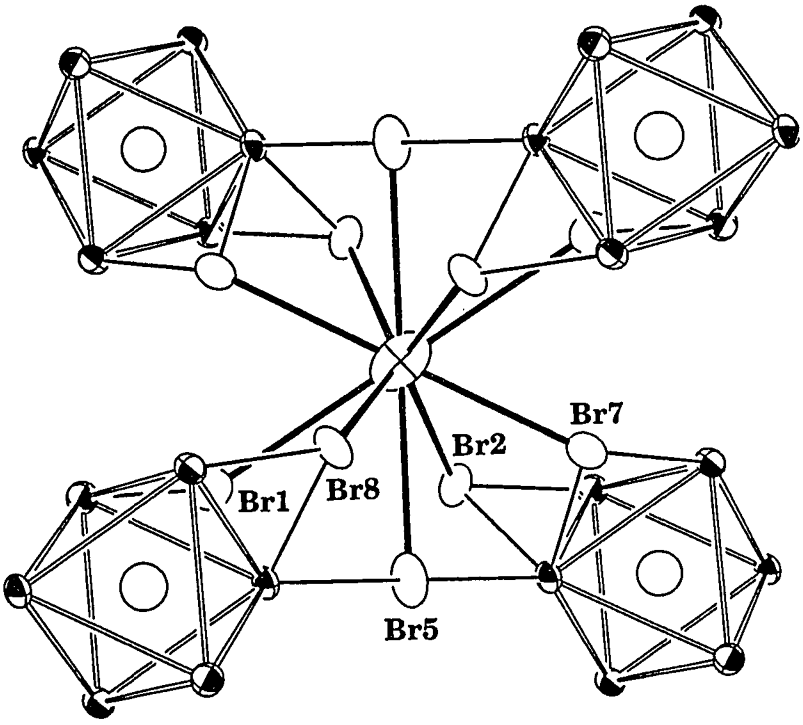

Figure 35. The local environment of Rb1 in $Rb_3Zr_6Br_{15}Be$. The picture is drawn with the 2-fold axis perpendicular to the paper (90% probability)

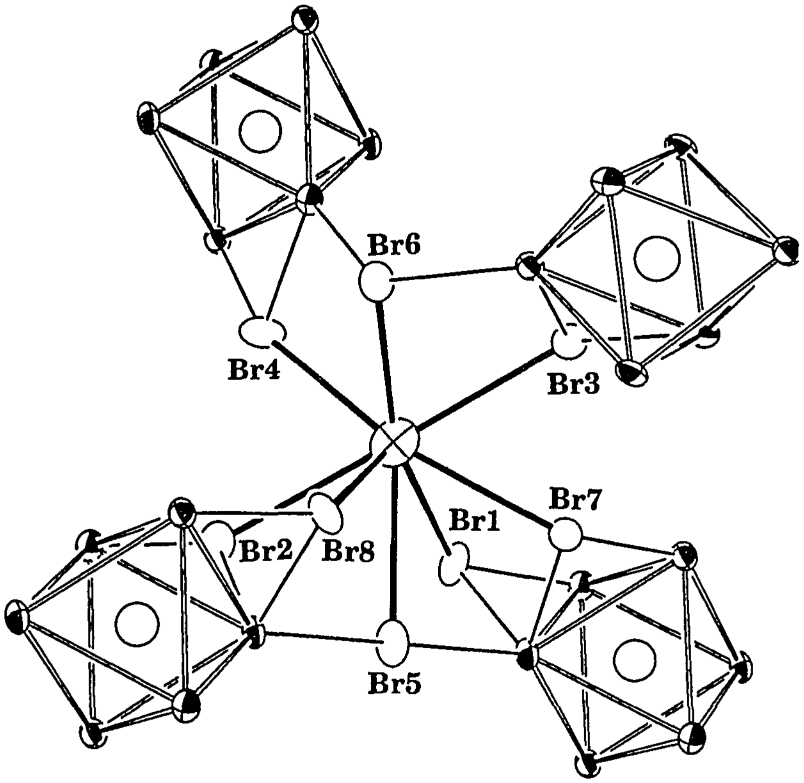

Figure 36. The local environment of Rb2 in $Rb_3Zr_6Br_{15}Be$. No symmetries are imposed at Rb2 site (90% probability)

$Cs_4Zr_6Br_{16}Be$, 2.372(2) Å, yet, 0.043 Å (21σ) longer than that in $K_3Zr_6Cl_{15}Be$. The average Zr-Zr distance is 3.360(2) Å, again fairly close to the average value in $Cs_4Zr_6Br_{16}Be$, 3.355(3) Å, and 0.060 Å (28σ) longer than the one in $K_3Zr_6Cl_{15}Be$, 3.2997(8) Å. The short Br-Br distances in $Rb_3Zr_6Br_{15}Be$, i.e., 3.496(2) Å and 3.547(3) Å, suggest that the differences in the Zr-Zr and Zr-Be distances are caused by the larger extent of the matrix effect in the bromide lattice. The Zr-$Br^{a\text{-}a}$ distances within each layer are 2.856(2) Å or 2.904(2) Å and the linear one connecting the layers is 2.901(2) Å. As expected, they are longer than the Zr-Br^i distances, which are in the range of 2.691(2)-2.738(2) Å.

$CS_{3.4}ZR_6BR_{15}B$ AND $CS_{3.0}ZR_6BR_{15}C$

Synthesis: $Cs_3Zr_6Br_{15}C$ was firstly observed in the reactions loaded as $CsZr_6Br_9C$ and $Cs_2Zr_6Br_{10}C$, aimed for the more reduced cluster phases. These reactions were carried out at 850°C for three weeks. After the single crystal study was done on the carbide, a reaction was loaded stoichiometrically, and a high yield (>85%) was realized therein. The refined stoichiometry for the carbide was also tried with boron as the interstitial. Again, a high yield (~85%) and good single crystals were obtained. The single crystal structure refinement gave the boride phase a $Cs_{3.4}Zr_6Br_{15}B$ empirical formula. The reactions loaded with the refined stoichiometry, however, yielded a different Cs-containing cluster phase, $(Cs_4Br)Zr_6Br_{16}B$ (6-16 type). In other words, a slightly lower Cs content is the key factor in order to prepare $Cs_{3.4}Zr_6Br_{15}B$. From the data listed in Table 27, one can see that the boride Guinier lattice constants did not change very

Table 27. The Guinier cell constants (Å) for $Cs_3Zr_6Br_{15}C$ and $Cs_{3.4}Zr_6Br_{15}B$

stoichiometry loaded	a	c	V (Å^3)
$CsZr_6Br_9C$	13.1031(6)	35.800(3)	5321.5(7)
$Cs_3Zr_6Br_{15}C$ (30% excess Zr)	13.1010(9)	35.819(5)	5324(1)
$Cs_3Zr_6Br_{15}C$ (15% excess Zr)	13.102(1)	35.784(4)	5320(1)
$Cs_3Zr_6Br_{15}C$	13.088(1)	35.746(5)	5303(1)
$Cs_4Zr_6Br_{15}C$	13.098(1)	35.756(4)	5312(1)
$CsZr_6Br_9B$	13.110(1)	35.96(1)	5351(2)
$Cs_2Zr_6Br_{15}B$	13.104(2)	35.966(4)	5348(1)
$Cs_3Zr_6Br_{15}B$	13.116(1)	35.980(6)	5360(2)

much when different Cs contents were loaded in the reaction. In other words, the phase breadth is rather narrow for $Cs_{3.4}Zr_6Br_{15}B$. The lattice constants of the carbide from the stoichiometric reaction are significantly smaller than those from the reactions with much more reducing conditions. It is possible that the phase from the stoichiometric reaction contains fewer (than 3) Cs as about 7-8% Cs_2ZrBr_6 was seen in the Guinier powder pattern as well.

Single Crystal Studies: The major features of the $Cs_3Zr_6Br_{15}C$ Guinier powder pattern looked similar to those of $Cs_3(ZrCl_5)Zr_6Cl_{15}Mn(B)$,[41] yet discrepancies were also observed. That is to say, the backbone of the bromide structure might be essentially the same as that of the chloride phase, and the differences could be in the cation or anion sites in the lattice. Therefore, more detailed structure study was done to reveal the possibly subtle differences. The single crystal study was firstly performed on the crystal found in the reaction loaded with the stoichiometry of $CsZr_6Br_9C$. The data were collected on an ENRAF NONIUS CAD4 diffractometer at room temperature. The reflections found during SEARCH could be indexed on the basis of a primitive triclinic cell. In fact, it was the non-standard setting of a rhombohedral cell that was transformed later to the R-centered hexagonal setting by the cell reduction program TRANS. Prior to the data collection, about 1000 reflections were collected without applying the R-centering reflection condition, $-h+k+l=3n$. Since none of the reflections with $-h+k+l\neq3n$ was observed, the centering symmetry was confirmed. Therefore, a hemisphere of data were collected up to 50° (2θ) with an ω-scan mode. The only two space groups that fulfill the reflection conditions found in the data set (h+l=3n for $h\bar{h}l$ type; l=3n for hhl type; l=6n for 00l type) are R3c (no.161) and $R\bar{3}c$ (no.167). Since the intensity statistics indicated the existence of the centric symmetry, space group $R\bar{3}c$ was chosen. All the observed reflections were merged in the corresponding point group $\bar{3}m$ with R_{ave}=5.5%. Up to this stage, the cell dimensions, lattice symmetry, and the possible space group all showed resemblances to those of $Cs_3(ZrCl_5)Zr_6Cl_{15}Mn$.

The initial model was obtained using the direct methods provided by the SHELXS-86 program package. Since the peak height of Zr is not significantly different from that of Br, the corresponding Zr and Br positions were recognized mainly by the bond distances around these peaks. All the Zr and Br positions could be located in the initial model and the ORTEP picture showed that the framework of this bromide was very similar to $Cs_3(ZrCl_5)Zr_6Cl_{15}Mn$. The differences came out after all the cation positions were located. After the isotropic refinements were carried out on all the Zr and Br atoms, the difference Fourier map was calculated. One large peak at about 20 e/Å^3 height showed up at the (1/2, 0, 0) position that is fully occupied by Cs^+ in $Cs_3(ZrCl_5)Zr_6Cl_{15}Mn$. The distances from this peak to the adjacent Br atoms were very reasonable for a Cs atom, whereas, the peak height indicated that this position could only be partially occupied by Cs atoms (Cs1). Moreover, the cavity hosting the $ZrCl_5^-$ polyanion in the chloride was still empty at this stage. After the anisotropic thermal parameters of the Cs1 position were refined, one more peak (~ 9.4 e/Å^3)

was found on the difference Fourier map, right in the cavity formerly occupied by the $ZrCl_5^-$. Since the closest Br atoms around this peak were at about 4 Å, this position was loaded with cesium (Cs2). The occupancy of Cs1 position refined as 76(1)% and Cs2 as 37(2)%. This result yielded the $Cs_{3.02(7)}Zr_6Br_{15}C$ empirical formula.

The secondary extinction coefficient and the isotropic thermal parameter of the interstitial C atom were refined after the anisotropic refinements were carried out for all the heavy atom positions. The final refinement converged at R=5.4% and R_w=5.9%. What is worth mentioning here is that the final difference Fourier map was not very flat, for two relatively distinct peaks were found 0.35 Å and 2.17 Å away from the oversized Cs2 site. The peak heights were 3.88 e/Å^3 and 3.51 e/Å^3, respectively, which were about 2.2 e/Å^3 and 1.9 e/Å^3 higher than the background. The same feature was also noticed in the boride structure, indicating that the Cs atoms are slightly disordered in the big cavity. Another noticeable feature was the diffuse ordering in both Cs positions indicated by their large thermal ellipsoids. The thermal displacement of the Cs atoms did get smaller when the structure was refined with the data set collected at lower temperature, -50°C, on the crystal from the reaction loaded as $Cs_2Zr_6Br_{10}C$. The errors in the positional and thermal parameters of all the atoms were also smaller. Besides, no leftover peaks higher than 0.6 e/Å^3 stood out from the background. As listed in Tables 28 and 29, these two refinements gave essentially the same Cs content even though the crystals on which the data

Table 28. Crystal data for $Cs_{3.02(7)}Zr_6Br_{15}C$ and $Cs_{3.18(5)}Zr_6Br_{15}C$

	$Cs_{3.02(7)}Zr_6Br_{15}C$	$Cs_{3.18(5)}Zr_6Br_{15}C$
space group, Z	$R\bar{3}c$ (no. 167), 6	$R\bar{3}c$ (no. 167), 6
cell parameters[a]		
a (Å)	13.1031(6)	13.0862(6)
c	35.800(3)	35.823(4)
V (Å^3)	5321.5(7)	5312.8(8)
crystal dimens.(mm)	0.06 x 0.06 x 0.25	0.05 x 0.11 x 0.23
octants measured	±h, k, ±l	±h, k, ±l
2θ(max), deg.	50	50
temperature, °C	23	-50
reflections		
measured	6483	6484
observed ($I/\sigma(I)>3.0$)	2282	3236
indep.	595	1121
abs. coeff. (Mo, Kα, cm^{-1})	214.20	214.61
transm. coeff. range	0.74-1.00	0.56-1.00
R_{ave}, % (obs.)	5.7	4.9
no. variables	46	46
sec. extinct. coeff.	1(2) x 10^{-9}	1.4(3) x 10^{-8}
R, %	5.4	7.1
R_w, %	5.9	7.5

[a] Guinier data

Table 29. Positional and thermal parameters for $Cs_{3.02(7)}Zr_6Br_{15}C$ and $Cs_{3.18(5)}Zr_6Br_{15}C$

Atom	Psn.	x	y	z	B_{eq}($Å^2$)
<u>$Cs_{3.02(7)}Zr_6Br_{15}C$</u>					
Zr	36(f)	0.1373(2)	0.1467(2)	0.03700(6)	1.2(1)
Br1	18(e)	0.3494(3)	0	1/4	1.9(2)
Br2	36(f)	0.1711(3)	0.0102(3)	0.08538(8)	2.0(1)
Br3	36(f)	0.3308(3)	0.1787(3)	0.0007(1)	2.0(1)
C	6(b)	0	0	0	2(1)
Cs1[b]	18(d)	1/2	0	0	12.3(5)
Cs2[c]	12(c)	0	0	0.2964(7)	17(2)
<u>$Cs_{3.18(5)}Zr_6Br_{15}C$</u>					
Zr	36(f)	0.1377(2)	0.1461(2)	0.03694(5)	0.85(6)
Br1	18(e)	0.3491(2)	0	1/4	1.4(1)
Br2	36(f)	0.1713(2)	0.0095(2)	0.08519(6)	1.50(7)
Br3	36(f)	0.3308(2)	0.1759(2)	0.00096(6)	1.40(7)
C	6(b)	0	0	0	4(1)
Cs1[d]	18(d)	1/2	0	0	6.9(2)
Cs2[e]	12(c)	0	0	0.3005(4)	4.4(5)

[a] $U \times 10^3$

[b] 76(1)% occupied

[c] 37(2)% occupied

[d] 86(1)% occupied

[e] 30(1)% occupied

U_{11}[a]	U_{22}	U_{33}	U_{12}	U_{13}	U_{23}
15(2)	14(2)	15(1)	6(1)	0(1)	0(1)
24(2)	22(2)	25(2)	$1/2U_{22}$	-20(4)	$2U_{13}$
30(2)	21(2)	23(1)	10(2)	-9(2)	1(2)
20(2)	28(2)	24(2)	8(2)	2(1)	-6(2)
20(20)					
44(4)	300(10)	129(7)	87(5)	46(4)	167(7)
180(20)	U_{11}	290(40)	$1/2U_{11}$	0	0
9(1)	9(1)	12.6(9)	4.0(9)	-1.0(8)	-1.1(8)
17(1)	16(2)	21(2)	$1/2U_{22}$	-2.4(7)	$2U_{13}$
22(1)	16(1)	18(1)	8(1)	-9(1)	-1(1)
15(1)	17(1)	19(1)	6(1)	2.4(8)	-4(1)
50(20)					
26(2)	167(5)	69(3)	48(2)	23(2)	86(3)
39(5)	U_{11}	90(10)	$1/2U_{11}$	0	0

collection were conducted were from the reactions loaded as $CsZr_6Br_9C$ and $Cs_2Zr_6Br_{10}C$ respectively. The relatively large R values for the refinement with the low-temperature data set could be due to the contributions of more weak reflections and a more serious absorption problem for a larger crystal. A single crystal structure study was also carried out on the same phase, yet with boron as interstitial. The refinement gave the $Cs_{3.39(5)}Zr_6Br_{15}B$ composition. The other important data collection as well as refined positional and anisotropic thermal parameters for the boride phase can be found in Tables 30 and 31, respectively.

Structure Descriptions and Discussions: The framework of $Cs_{3.4}Zr_6Br_{15}B$ and $Cs_3Zr_6Br_{15}C$ is very similar to that of $Cs_3(ZrCl_5)Zr_6Cl_{15}Mn$ in terms of the cluster linkage or the stacking sequence of the close packed layers. The most striking difference between the corresponding bromide and chloride phases is the replacement of $(ZrCl_5)^-$ by two Cs^+ cations (Cs2) in the bromide lattice (Figure 37). Each unit cell has twelve close packed layers along the c direction. The stacking sequence of these layers can be described as $(ABAC)_3$ or $(ch)_6$. Among these layers, B and C are pure bromine layers, while A layer contains bromine and cesium as well as the interstitial carbon or boron atoms. The layers are related either by R-centering or the c-glide perpendicular to a and b directions. Within the unit cell, each layer has twelve close packed sites. In the lattice of $Cs_3(ZrCl_5)Zr_6Cl_{15}Mn$, all these twelve positions within each layer are occupied. On the contrary, none of these layers in the corresponding bromide lattice is saturated. The removal of $(ZrCl_5)^-$ leaves four vacancies (3Cl + 1Zr) in the B

Table 30. Crystal data for $Cs_{3.39(5)}Zr_6Br_{15}B$

space group, Z	$R\bar{3}c$ (no. 167), 6
cell parameters[a]	
a (Å)	13.116(1)
c	35.980(6)
V (Å^3)	5360(2)
crystal dimens. (mm)	0.03 x 0.05 x 0.17
octants measured	±h, k, l
2θ (max.), deg.	50
reflections	
measured	3380
observed (I/σ(I)>3.0)	1369
indep.	551
abs. coeff. (Mo Kα, cm^{-1})	212.70
transm. coeff. range	0.77-1.00
R_{ave}, % (obs.)	4.1
no. variables	46
sec. extinct. coeff.	9.2(9) x 10^{-9}
R, %	5.4
R_w, %	4.4

[a] Guinier data

Table 31. Positional and thermal parameters for $Cs_{3.39(5)}Zr_6Br_{15}B$

Atom	Psn.	x	y	z	$B_{eq}(Å^2)$
Zr	36(f)	0.1406(2)	0.1481(2)	0.03754(6)	0.86(8)
Br1	18(e)	0.3469(4)	0	1/4	1.6(3)
Br2	36(f)	0.1702(3)	0.0084(3)	0.08504(8)	1.6(1)
Br3	36(f)	0.3304(3)	0.1752(3)	0.0007(1)	1.5(1)
C	6(b)	0	0	0	2(1)
Cs1[b]	18(d)	1/2	0	0	7.8(3)
Cs2[c]	12(c)	0	0	0.3021(5)	6.6(7)

[a] U x 10^3

[b] 93.1(9)% occupied

[c] 30(1)% occupied

U_{11}[a]	U_{22}	U_{33}	U_{12}	U_{13}	U_{23}
11(1)	10(1)	10(1)	4(1)	-1(1)	-1(1)
27(5)	16(2)	20(2)	$1/2U_{22}$	-4(1)	$2U_{13}$
24(2)	17(2)	19(1)	10(2)	-9(1)	-3(1)
15(2)	21(2)	20(1)	7(2)	3(1)	-4(1)
30(20)					
33(3)	183(6)	80(4)	52(4)	21(2)	88(4)
72(9)	U_{11}	110(20)	$1/2U_{11}$	0	0

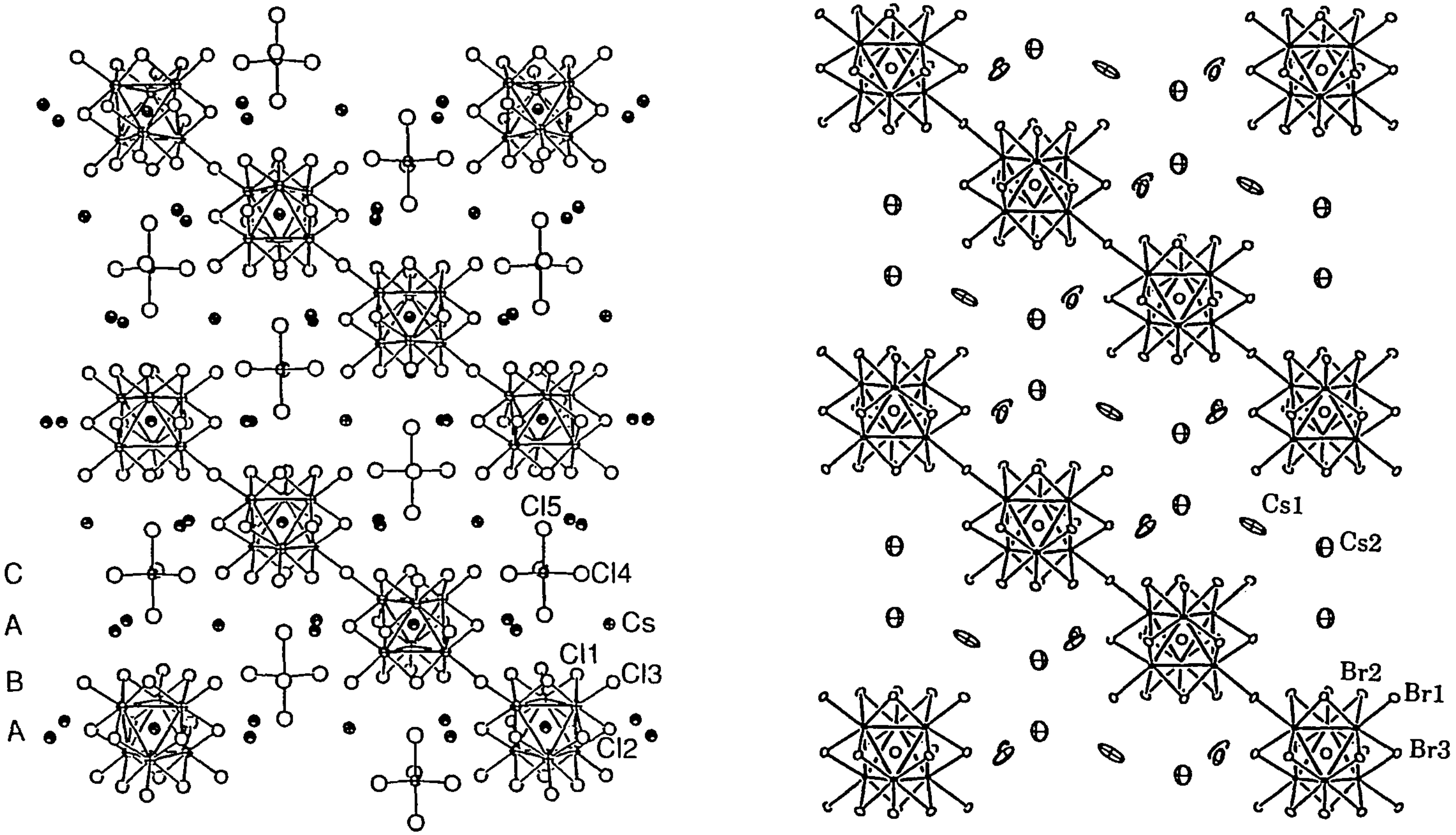

Figure 37. The comparison of the structure of $Cs_3(ZrCl_5)Zr_6Cl_{15}Mn$ (left, 90% probability [41]) and $Cs_{3.4}Zr_6Br_{15}B$ (right, 50% probability). The views are along the [110] direction showing the identical framework and the replacement of $(ZrCl_5)^-$ anion by Cs2 in the bromide lattice

layer and two (2Cl) in the A layer. The cavity created by these vacancies has about 10 Å diameter, which has more than enough room to host two Cs^+ cations.

The connectivity of the cluster units in $Cs_{3.4}Zr_6Br_{15}B$, $Cs_3Zr_6Br_{15}C$, and $Cs_3(ZrCl_5)Zr_6Cl_{15}Mn$ is essentially the same as in half of the Nb_6F_{15} framework.[5] Two major differences are noticed when these two structure types are compared. Firstly, there are two identical interpenetrating cluster nets in Nb_6F_{15}, while in $Cs_{3.4}Zr_6Br_{15}B$, $Cs_{3.0}Zr_6Br_{15}C$, and $Cs_3(ZrCl_5)Zr_6Cl_{15}Mn$, the second net is missing, leaving large cavities occupied by Cs^+ cations, or Cs^+ and $(ZrCl_5)^-$ as in the case of $Cs_3(ZrCl_5)Zr_6Cl_{15}Mn$. Secondly, the connections between the clusters are bent at Br^{a-a} (Figure 38), 134.0(2)° in $Cs_{3.4}Zr_6Br_{15}B$, 134.3(2)° in $Cs_3Zr_6Br_{15}C$ (Table 32), and 133.39(6)° in $Cs_3(ZrCl_5)Zr_6Cl_{15}Mn$, whereas, those in the cubic Nb_6F_{15} lattice are linear (Figure 38). The structure of $Cs_{3.4}Zr_6Br_{15}B$, $Cs_3Zr_6Br_{15}C$ as well as $Cs_3(ZrCl_5)Zr_6Cl_{15}Mn$ also undergoes a trigonal twist (30°) resulting in the doubling of the c axis. The same kind of twist has been seen in a series of structures derived from perovskite aristotype.[72] The large size Cs^+ cation or $(ZrCl_5)^-$ polyanion is the key factor in stabilizing the open framework of the corresponding bromide or chloride 6-15 phases. This structure type could not be realized with the smaller Rb^+ or K^+ cations. In other words, the large cations or anions act to help prop open the lattice.

As mentioned earlier, the cavity hosting the $(ZrCl_5)^-$ polyanion in the chloride phase is occupied by two Cs^+ cations in the bromide compounds (Figure 39). It is very unusual for a lattice to be able to accommodate oppositely charged

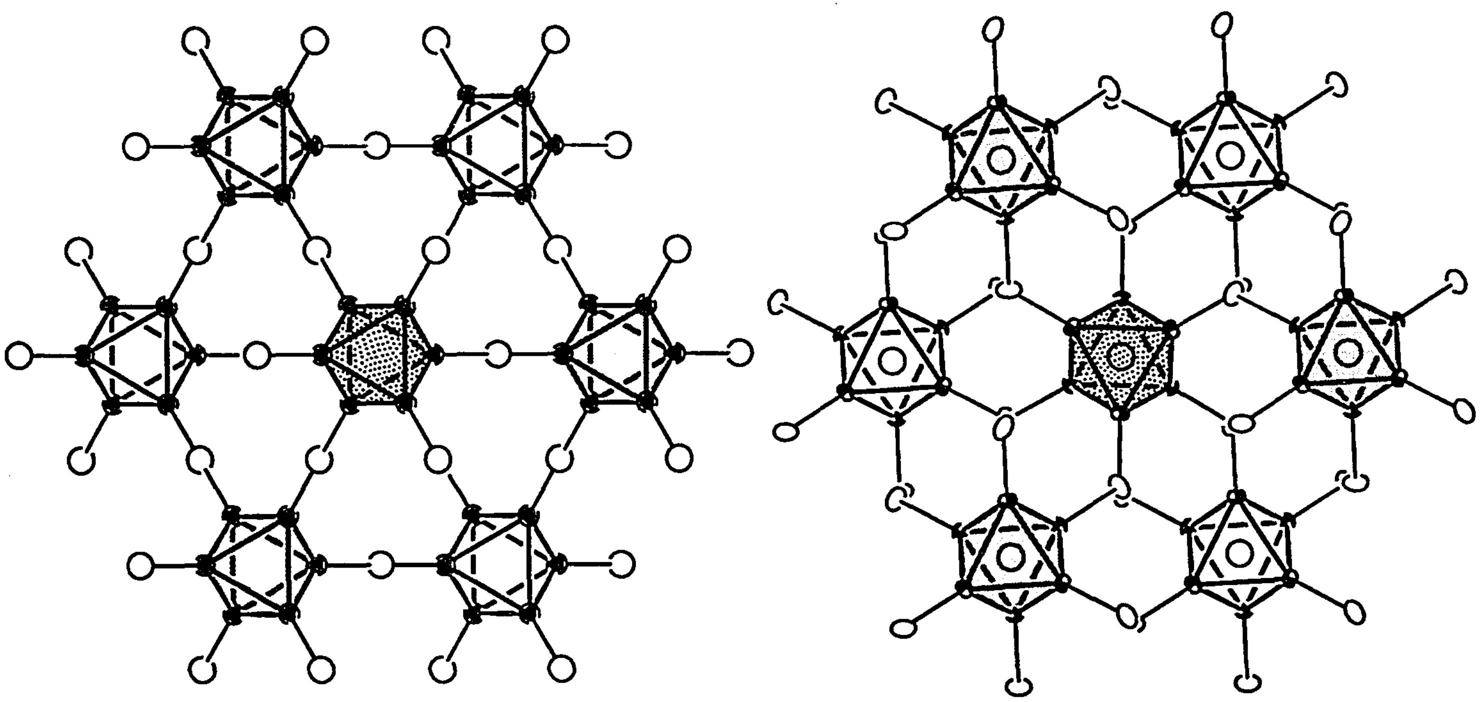

Figure 38. The comparison of the cluster linkages at the $X^{a\text{-}a}$ atoms. The view is along the [111] direction for Nb_6F_{15} (left) and along [001] direction for $Cs_3Zr_6Br_{15}C$ (right). The different shading indicates the clusters ar different levels (90% probability)

Table 32. Important bond distances (Å) and angles (°) for $Cs_{3.02(7)}Zr_6Br_{15}C$, $Cs_{3.18(5)}Zr_6Br_{15}C$, and $Cs_{3.39(5)}Zr_6Br_{15}B$

		$Cs_{3.02(7)}Zr_6Br_{15}C$	$Cs_{3.18(5)}Zr_6Br_{15}C$	$Cs_{3.39(5)}Zr_6Br_{15}B$
Distances				
d(Zr-Zr)	x2[a]	3.228(4)	3.221(3)	3.283(4)
	x2	3.239(4)	3.235(3)	3.300(4)
$\bar{d}$		3.234	3.228	3.292
d(Zr-C)	x1	2.286(2)	2.282(2)	2.327(2)
d(Zr-Br^{a-a})				
Zr-Br1	x1	2.920(3)	2.922(2)	2.904(3)
d(Zr-Br^{i})				
Zr-Br2	x1	2.671(4)	2.672(3)	2.669(4)
	x1	2.681(4)	2.677(3)	2.672(4)
Zr-Br3	x1	2.687(4)	2.682(3)	2.681(4)
	x1	2.688(4)	2.685(3)	2.682(4)
d(Cs-Br)				
Cs1-Br1	x2	3.765(2)	3.763(1)	3.767(2)
-Br2	x2	3.582(3)	3.590(2)	3.616(3)
-Br3	x2	3.648(3)	3.674(2)	3.690(3)
	x2	3.948(3)	3.912(2)	3.918(3)
$\bar{d}$		3.736	3.735	3.748
Cs2-Br3	x3	4.029(9)	3.977(5)	3.977(6)
Angles				
Zr-Zr-Zr	x2	60.00	60.00	60.00
	x2	60.11(5)	60.14(4)	60.17(4)
	x2	90.00	90.00	90.00
Zr-Br1-Zr	x1	134.3(2)	134.6(1)	134.0(2)
Br2-Zr-Br3	x2	164.0(1)	164.0(1)	165.8(1)
	x2	164.2(1)	164.1(1)	165.9(1)
Br1-Zr-Z	x1	178.6(1)	178.91(9)	178.8(1)

[a] Number of times the distances and angles occur per atom

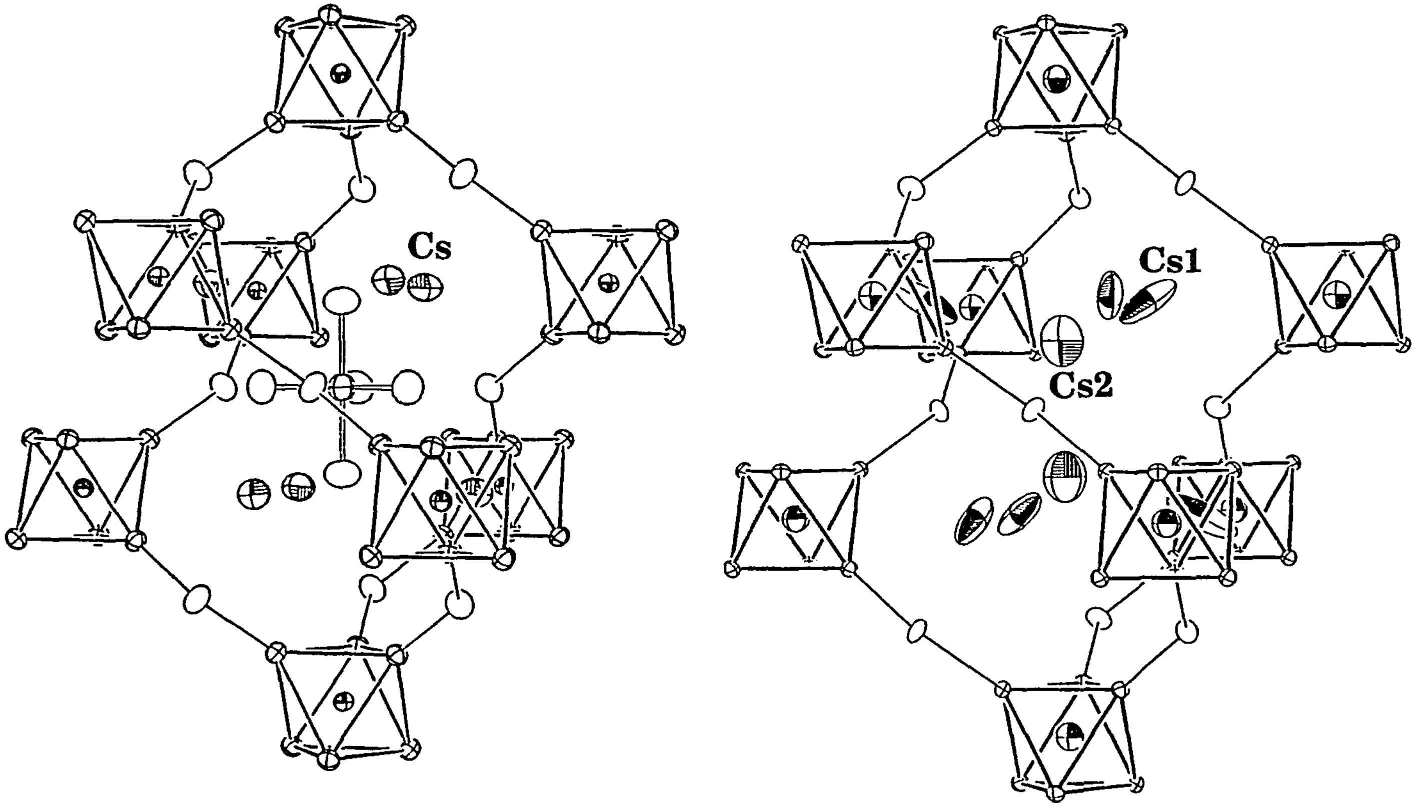

Figure 39. The comparison of the structure of $Cs_3(ZrCl_5)Zr_6Cl_{15}Mn$ [41] and $Cs_{3.4}Zr_6Br_{15}B$. The cavity containing $ZrCl_5^-$ and Cs^+ in the chloride lattice (left, 90% probability [41]) is now occupied only by Cs^+ cations in the bromide lattice (right, 80% probability)

atoms or atom groups without any noticeable modification in the framework. In this sense, the structure behaves rather like that of a zeolite which has both the cation and anion sites in the cavity. Figure 40 shows the environment of Cs2 in $Cs_{3.4}Zr_6Br_{15}B$, which replaces half the $(ZrCl_5)^-$ in the chloride lattice. As noted, there are only three bromine atoms at the distance 3.977(6) Å (Table 32), even longer than the distance between a twelve-coordinate Cs^+ and Br^- (3.84 Å). The other six bromine atoms shown in the picture are all at greater than 4.5 Å. This situation helps to understand why the Cs2 has large thermal displacement.

As illustrated in Figure 41, the vacancies in the close packed layers also create an anisotropic environment for the Cs1 site. Compared with the 12-coordinate Cs position in $Cs_3(ZrCl_5)Zr_6Br_{15}Mn$, the same position in the bromide lattice (Cs1) only has eight adjacent bromine atoms. In other words, four of the chlorine atoms around the Cs position are in the $(ZrCl_5)^-$ polyanions. Furthermore, six out of eight bromine atoms are around the waist of the Cs1 position, leaving most of the top and the bottom open. This explains why the Cs1 position in the bromide lattice has such a peculiar anisotropic thermal ellipsoid. The plot of the observed electron density on Cs1 site shows a similar electron density distribution (Figure 42). The average distance for Cs1-Br is 3.736(3) Å in $Cs_3Zr_6Br_{15}C$ and 3.748(3) Å in $Cs_{3.4}Zr_6Br_{15}B$. They are both slightly longer than the sum of the crystal radii of eight-coordinate Cs^+ and Br^-, 3.70 Å. A careful study of this structure reveals that there are also one-dimensional tunnels in the lattice along the b direction (Figure 43(a)). As Figure 43(b)

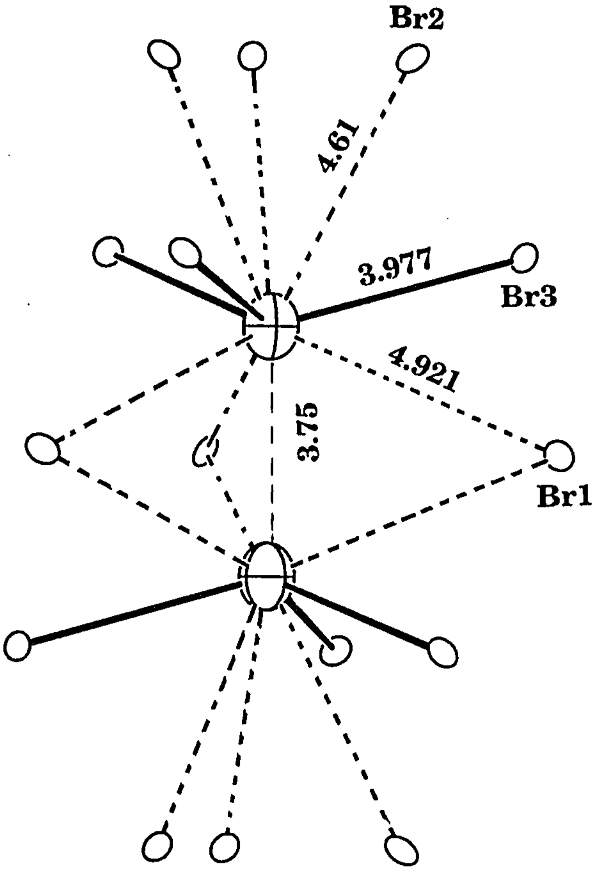

Figure 40. The local environment of Cs2 in $Cs_{3.4}Zr_6Br_{15}B$ with the C_3 axis vertical. The Br atoms connected by the dotted lines are at the distances larger than 4.5 Å (50% probability)

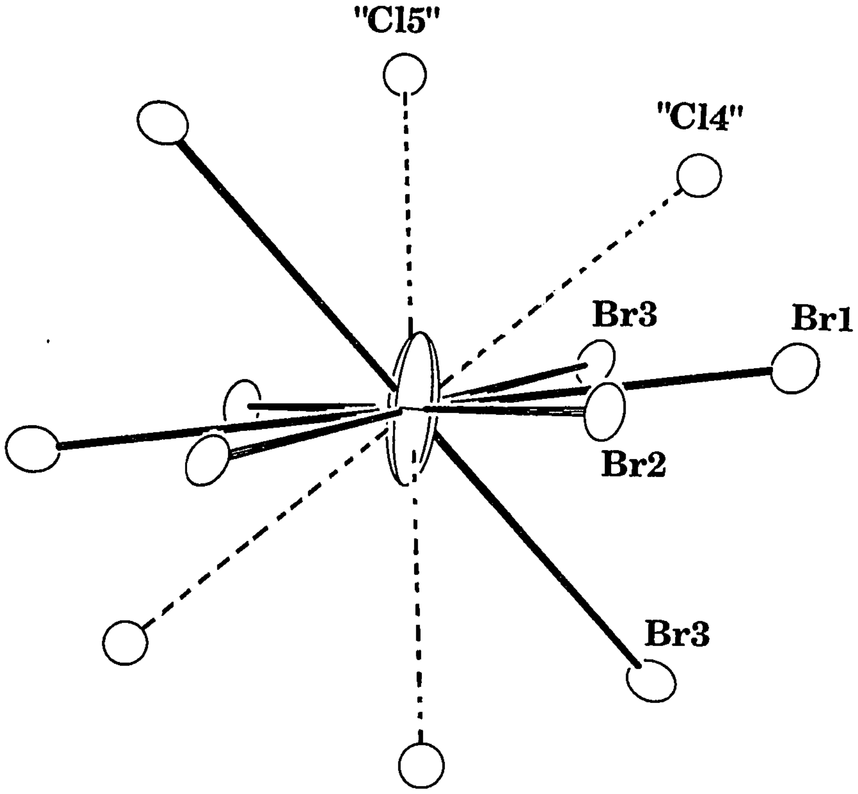

Figure 41. The local environment of Cs1 in the lattice of $Cs_{3.4}Zr_6Br_{15}B$ with $\bar{1}$ symmetry. The atoms connected by dotted lines are Cl4 and Cl5 positions in $Cs_3(ZrCl_5)Zr_6Cl_{15}Mn$, which are missing in the bromide (50% probability)

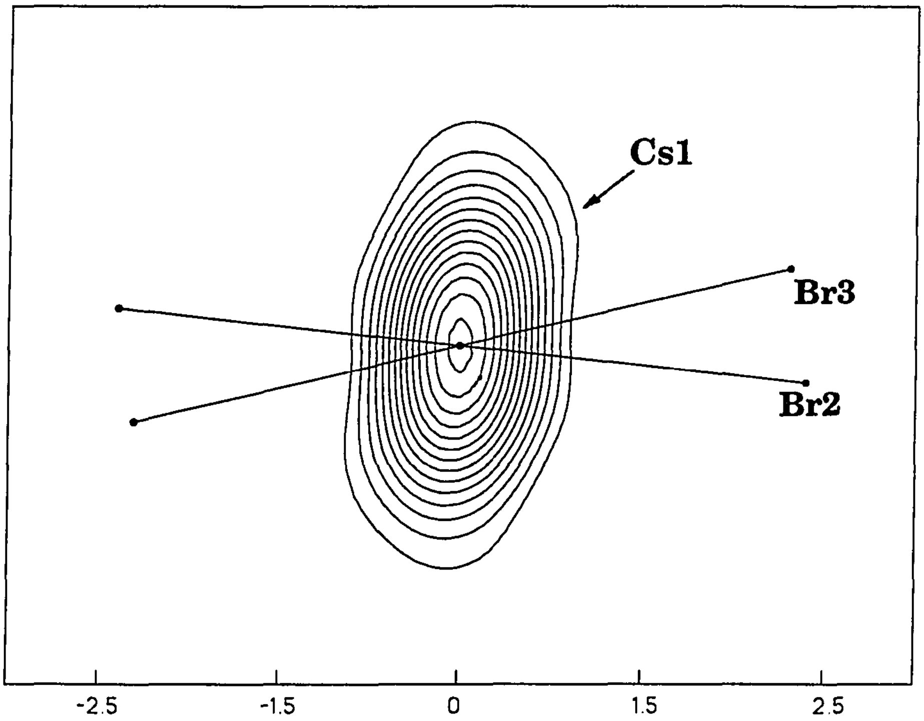

Figure 42. A plot (3.8 x 6.0 Å) of the electron density around Cs1 in $Cs_{3.4}Zr_6Br_{15}B$ calculated from F_{obs}. The orientation of this drawing is the same as the one in Figure 41. The contour interval is 5 e/Å^3

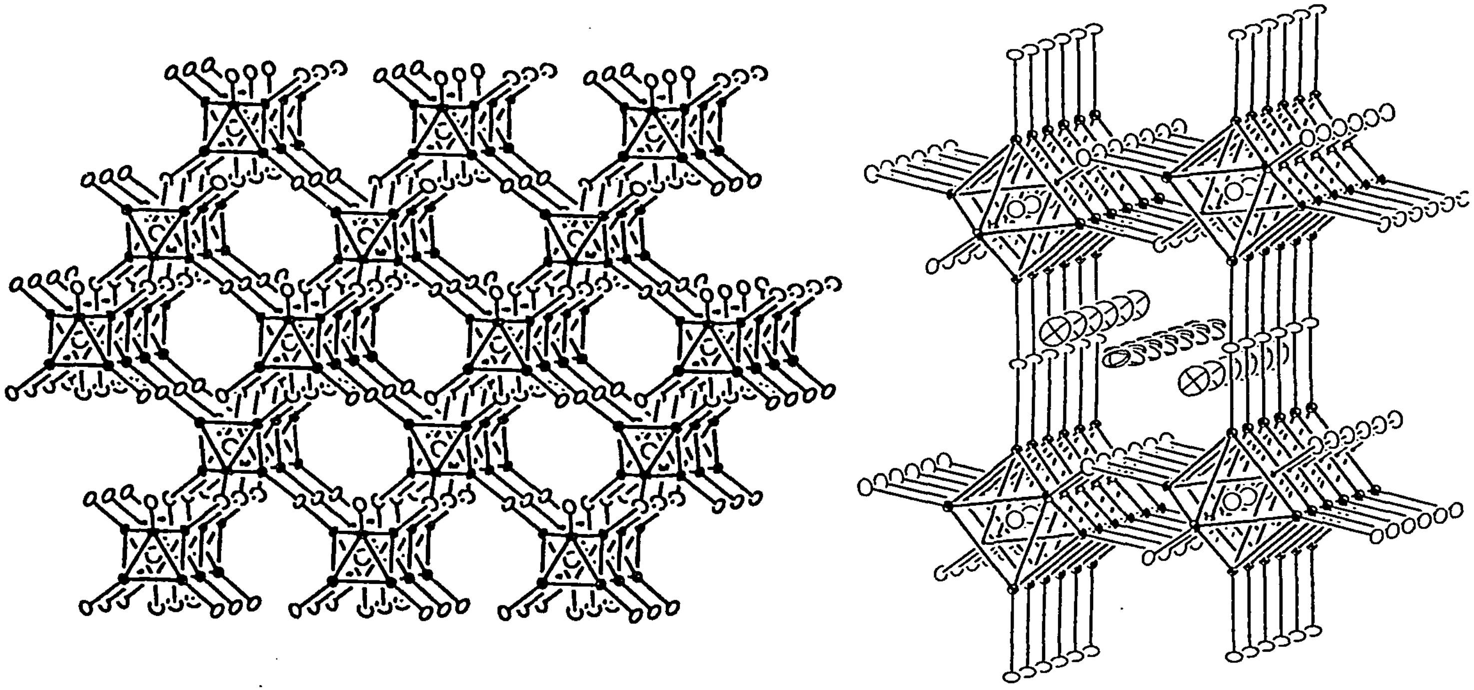

(a) (b)

Figure 43. Part (a) shows the one dimensional tunnels in $Cs_3Zr_6Br_{15}C$ approximately along [010] direction (90% probability). Part (b) shows that the tunnel is occupied by the Cs^+ arrays (70% probability)

shows, the tunnels are stuffed by Cs^+ arrays. The cesium position in $Cs_3(ZrCl_5)Zr_6Cl_{15}Mn$ is fully occupied so that the zirconium cluster unit has the 14 optimal electrons in its bonding orbitals. The cesium positions in either boride or carbide bromide phases, however, are only partially occupied. In the boride bromide phase the occupancies of Cs1 and Cs2 positions refined as 93.1(9)% and 30(1)%, respectively, to give a $Cs_{3.39(5)}Zr_6Br_{15}B$ empirical formula and 15.4e$^-$ to the (Zr_6B) cluster unit. This agrees with the magnetic susceptibility measurement carried out on the boride phase. When the interstitial element is changed from boron to carbon, the cesium content is reduced somewhat so that the zirconium cluster unit has about 16 electrons, the highest number found so far in the zirconium halide cluster compounds centered by main-group elements. The refined cesium occupancies correspond to $Cs_{3.02(7)}Zr_6Br_{15}C$ and $Cs_{3.18(5)}Zr_6Br_{15}C$, respectively.

The (Zr_6Z) cluster unit has a S_3 point symmetry. The average Zr-Zr distance in $Cs_3Zr_6Br_{15}C$ is 3.234(4) Å and the Zr-C distance is 2.287(2) Å. As expected, they are both shorter than those in $Cs_{3.4}Zr_6Br_{15}B$, which are 3.292(4) Å and 2.327(2) Å, respectively. The Zr-Br^i distances in the carbide are in the range of 2.671-2.688 Å, comparable to those in the boride, 2.669-2.682 Å. A slightly larger difference (4.2σ) is observed for the Zr-$Br^{a\text{-}a}$, 2.904(3) Å in $Cs_{3.4}Zr_6Br_{15}B$ and 2.920(3) Å in $Cs_{3.0}Zr_6Br_{15}C$.

Magnetic Susceptibility Study: Based on the refined cesium content, the cluster units in $Cs_{3.39(5)}Zr_6Br_{15}B$ have 15.39(5)e$^-$ in their bonding orbitals.

According to the discussions about the matrix effect in the previous sections, each cluster unit should contain 0.61(5) of an unpaired electron in the a_{2u} orbital. If it is true, the boride bromide phase should exhibit a temperature-dependent paramagnetic behavior with its μ_{eff} smaller than 1.73 μ_B, the value for one unpaired, spin-only and localized electron in the transition metal elements. As shown in Figure 44, $Cs_{3.39(5)}Zr_6Br_{15}B$ does have a temperature-dependent paramagnetic behavior with μ_{eff}=0.58(4) μ_B, calculated from the nonlinear least-square program.[62] The value is slightly lower than expected. The discrepancy is probably caused by the purity of the sample (about 85%) as well as the relatively large errors on the refined Cs occupancies. The quenching of the moment or the deviation from the Curie-Weiss behavior is evident at the temperature as high as 130K, but no ordering temperature is observed. The similar phenomenon has been observed in $CsZr_6I_{14}Mn$. The spin-orbit coupling in the octahedral crystal field may be responsible for the declining effective moment at lower temperatures.[33] The nonlinear least-squares program also yielded $5.41(2)\times10^{-4}$ (cgsu) as the value of the temperature-independent term, χ_{TIP} or χ^0. This value is very comparable to those obtained from the Nb and Ta halide cluster phases as well as their derivatives.[72] The temperature-independent term was referred as high frequency term by Van Vleck [73] in the susceptibility expression for it arises from a mixing of excited-state functions with the ground state in the presence of the magnetic field, when E_n-E_0>>kT.

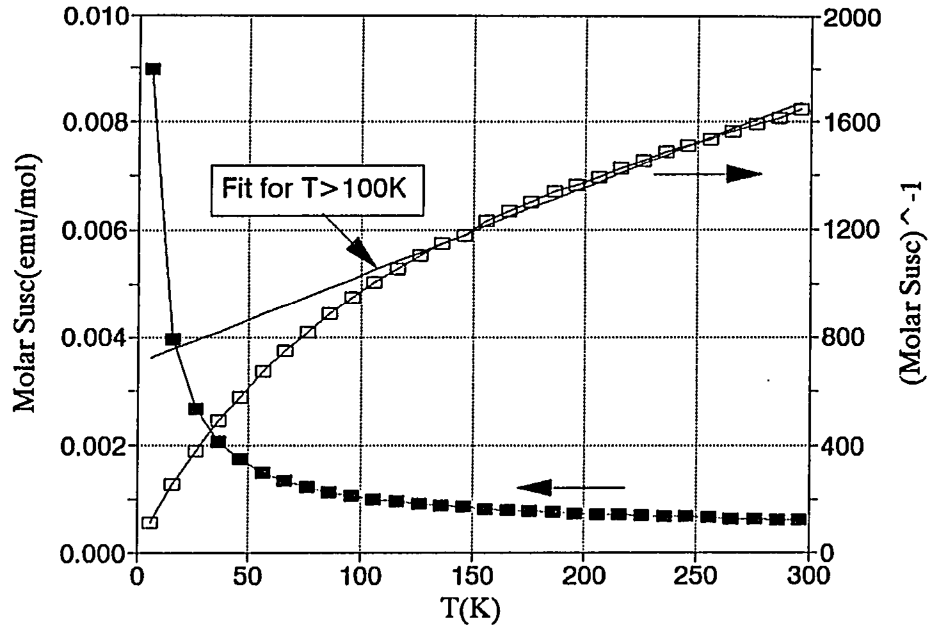

Figure 44. A plot of the magnetic susceptibility of $Cs_{3.4}Zr_6Br_{15}B$, corrected for ion core diamagnetism. It has the temperature-dependent paramagnetic behavior with μ_{eff}=0.58(4) μ_B, calculated from nonlinear Least Square program.

$\mathrm{RB_{5.0}ZR_6BR_{15}BE}$ AND $\mathrm{CS_{4.6}ZR_6BR_{15}BE}$

Synthesis: This new 6-15 structure was originally found in the reactions loaded with $\mathrm{Rb^+}$ as countercation and Be or B as interstitials. The Guinier powder patterns of these new phases did not look similar to that of any known zirconium halide cluster phase, indicating the possible discovery of a new structure type. Single crystals were found in the reactions loaded as $\mathrm{Rb_4Zr_6Br_{15}B}$ and $\mathrm{Rb_4Zr_6Br_{15}Be}$, carried out at 830°C for about four weeks. The single crystal structure refinements on the beryllide yielded the composition $\mathrm{Rb_{5.0(1)}Zr_6Br_{15}Be}$. Several reactions were purposely carried out with Cs as countercations. It turned out that the same structure type did form with $\mathrm{Cs^+}$ in a composition of $\mathrm{Cs_{4.60(8)}Zr_6Br_{15}Be}$ according to the structure refinement. Reactions with a lower Rb content, i.e., $\mathrm{Rb_2Zr_6Br_{15}Be}$, repeatedly yielded an unknown phase D, and those loaded as $\mathrm{Cs_2Zr_6Br_{15}Be}$ gave an unknown phase E.

Single Crystal Studies: Prior to the data collection, oscillation as well as Weissenberg film studies were conducted on the crystal from the reaction loaded as $\mathrm{Rb_4Zr_6Br_{15}B}$. The film data revealed that the lattice exhibits hexagonal symmetry with a=b=12.69 Å (Weissenberg data) and c=11.94 Å (oscillation axis). A mirror perpendicular to c was observed in the latter. Based on the zero and first layer Weissenberg films, no particular systematic extinction conditions were present in the a-b plane. After the orientation of the crystal was changed, the extinction l=2n+1 for 00l type was observed on the Weissenberg film. The possible space groups fulfilling the symmetry and the extinction conditions are $P6_3$, $P6_3/22$, and $P6_3/m$.

The study on the CAD4 diffractometer further confirmed the information provided by the film work. Therefore, two octants of data were collected up to 55° in 2θ. The ω-θ scan mode was chosen based on the peak profiles. A reasonable initial model was obtained in the space group $P6_322$ using the direct methods provided by SHELXS-86 program. An empirical absorption correction was applied to the raw data according to the ψ-scan measurements. The observed data were merged in the corresponding 622 point group with R_{ave}=4.8%. All the Zr and Br positions were successfully located and assigned by analyzing the initial model and rough ORTEP pictures. It turned out that the framework Zr to Br ratio was again 6 to 15 with all the terminal Br atoms shared between cluster units, $(Zr_6B)Br^i_{12}Br^{a\text{-}a}_{6/2}$. The long range cluster linkages, the cation sites, as well as the local symmetry around cluster units indicate that it is a new 6-15 structure type.

After the isotropic refinement of the Zr and Br atoms, two peaks stood out in a difference Fourier map. The distances from these peaks to the adjacent Br atoms were reasonable for Rb-Br bonds. The peak heights, however, were lower than what was expected for fully occupied Rb positions. Therefore, these two peaks were input as Rb atoms and their positional parameters and occupancies were refined simultaneously. One of the Rb peaks (Rb1) was at (0, 0, 0.2) which is close to the special position (0, 0, 1/4). Refining Rb1 at a general position yielded a very short Rb1-Rb1 distance, 1.32 Å. Nonetheless, the observed electron density was consistent with the refinement. The refinement yielded $Rb_{2.5}Zr_6Br_{15}B$ as its stoichiometry at this stage. Problems, however, appeared in the anisotropic refinement, as U_{33} of Rb1 was about 37 times bigger than U_{11} and U_{22}, and one of the Br atoms had a similar behavior as well. The anisotropic refinement yielded a composition of $Rb_{2.8}Zr_6Br_{15}B$ and converged with R=7.6% and R_w=6.6%. Lowering the symmetry of the space group to $P6_3$ did not solve the problems either.

More oscillation and Weissenberg photos were taken purposely for very long times. No evidence of a superlattice along any direction was observed. The problems could be intrinsic to the boride; the disorder of Rb cations in the beryllide, which contains more Rb cations, was much less serious than in the boride.

Data collection on the crystal of the Rb beryllide was performed on a CAD4 diffractometer. Two octants of data were collected up to 50° in 2θ. After an empirical absorption correction was applied according to the averaged ψ-scan measurements, all the observed reflections were averaged in the point group 622 with R_{ave}=5.0%. Other data collection parameters are compiled in Table 33. The Zr and Br positions from the boride refinement were used as an initial model in the beryllide refinement. Four cation positions were found in the difference Fourier map calculated after the isotropic refinements of Zr and Br atoms. As in the boride, the Rb1 position in the beryllide was on the general position (0,

Table 33. Crystal data for $Rb_{5.0(1)}Zr_6Br_{15}Be$ and $Cs_{4.60(8)}Zr_6Br_{15}Be$

	$Rb_{5.0(1)}Zr_6Br_{15}Be$	$Cs_{4.60(8)}Zr_6Br_{15}Be$
space group, Z	$P6_322$ (no. 182), 2	$P6_3$ (no. 173), 2
cell parameters[a]		
a (Å)	13.009(1)	13.105(1)
c	12.060(1)	12.156(1)
V (Å^3)	1767.6(4)	1808.1(4)
crystal dimens. (mm)	0.06 x 0.09 x 0.23	0.16 x 0.17 x 0.26
octants measured	±h, k, l	±h, k, ±l
2θ (max), deg.	50	50
reflections		
measured	3379	6613
observed ($I/\sigma(I)>3.0$)	1907	3512
indep.	769	1428
abs. coeff. (Mo, Kα,cm^{-1})	211.38	224.98
transm. coeff. range	0.35 - 1.00	0.58 - 1.00
R_{ave}, % (obs.)	5.0	5.5
no. variables	59	94
sec. extinct. coeff.	$5.5(2) \times 10^{-7}$	$5.6(3) \times 10^{-8}$
R, %	4.4	4.9
R_w, %	4.8	3.5

[a] Guinier data

0, z) instead of (0, 0, 1/4). Nonetheless, the U_{33} to U_{11} or U_{22} ratio was eight,which is more than four times smaller than for the boride. The refinement was consistent with the observed electron density distribution around Rb1 (Figure 45). Similar behavior was also observed on the Rb2 site. This site was not on, but was close to, the special position (x, 0, 0) (Table 34). The refinement of Rb2 fit fairly well with the observed electron density distribution about Rb2 (Figure 46). The structure solution in the lower symmetry space group $P6_3$ was not nearly as good as that in $P6_322$. Correlations made it very difficult to refine partially occupied and disordered Rb positions. All the positions except for the interstitial's were refined anisotropically, and the refinement converged at R=4.4% and R_w=4.8%. The final difference Fourier map was basically flat. The highest positive peak was 1.49 e/Å^3 which is essentially as high as the background, for the next five peaks range from 1.47 to 1.25 e/Å^3, and the lowest negative peak was -1.37 e/Å^3, comparable to the positive one. The other enantiomer was checked and discarded as it had slightly higher R and R_w values.

The crystal of the Cs-containing phase on which data collection was conducted was from the reaction loaded as $Cs_4Zr_6Br_{15}Be$. A hemisphere of data were collected on a CAD4 diffractometer. Other data collection parameters as well as data process results are listed in Table 33, together with those of $Rb_5Zr_6Br_{15}Be$. At first, the positional parameters refined for $Rb_5Zr_6Br_{15}Be$ were utilized as an initial model. After refinement, the observed electron density around Cs1, shown in Figure 47, was elongated along the tunnel direction

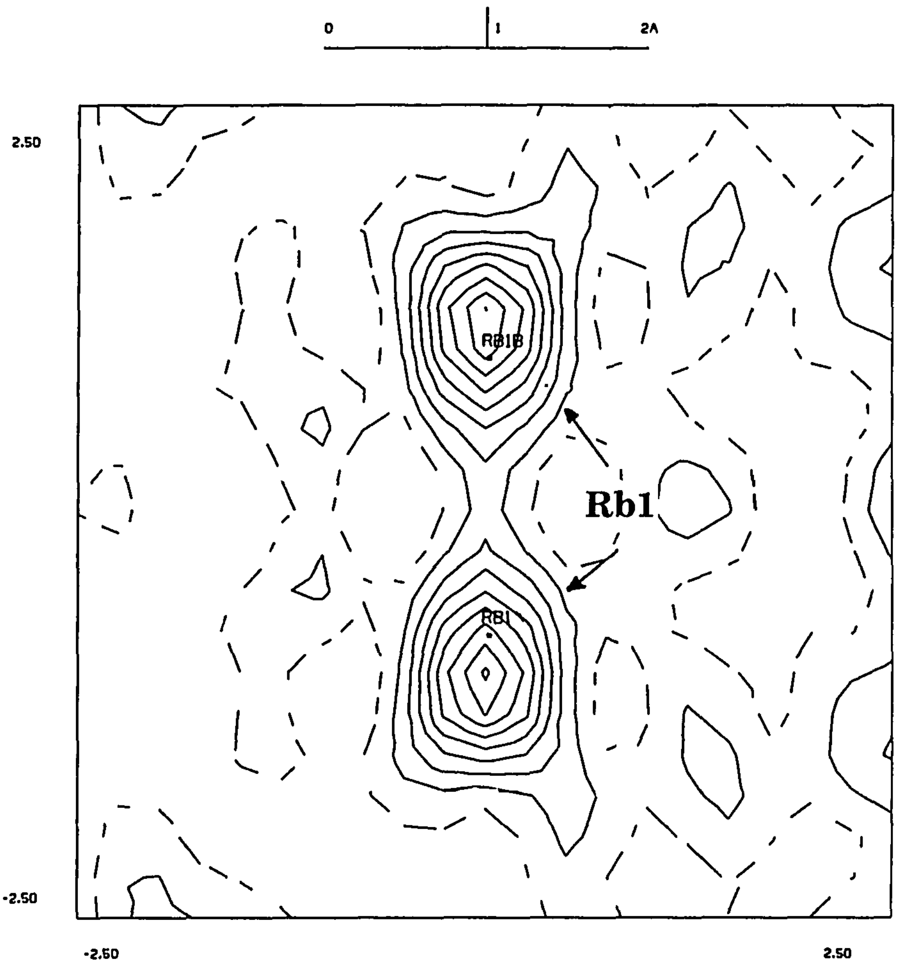

Figure 45. A plot of (5 x 5 Å) of the electron density around Rb1 in $Rb_5Zr_6Br_{15}Be$ calculated from F_{obs}. The plane is defined by Br3, Rb1, and one of Rb1's symmetry-equivalent position (0, 0, 0.321) designated as Rb1b. The contour interval is 5e/Å^3

Table 34. Positional and thermal parameters for $Rb_{5.0(1)}Zr_6Br_{15}Be$

Atom	Psn.	x	y	z	B_{eq}(Å^2)
Zr	12(i)	0.5184(2)	0.3353(2)	0.1359(1)	1.43(6)
Br1	6(g)	0.6713(3)	0	0	2.3(1)
Br2	12(i)	0.1669(2)	0.4966(2)	0.0088(2)	2.15(8)
Br3	6(h)	0.8353(2)	2x	1/4	2.5(2)
Br4	6(h)	0.4969(2)	2x	1/4	2.0(2)
Be	2(d)	2/3	1/3	1/4	1(1)
Rb1[b]	4(e)	0	0	0.179(2)	12(1)
Rb2[c]	12(i)	0.166(1)	-0.028(2)	0.054(1)	13(2)
Rb3[d]	6(h)	0.1575(4)	2x	1/4	6.0(5)
Rb4[e]	2(c)	1/3	2/3	1/4	2.5(5)

[a] U x 10^3

[b] 49(1)% occupied

[c] 31(1)% occupied

[d] 64(1)% occupied

[e] 29(1)% occupied

U_{11}[a]	U_{22}	U_{33}	U_{12}	U_{13}	U_{23}
17(1)	19(1)	19.0(8)	9(1)	-1(1)	1(2)
27(1)	25(2)	35(2)	1/2U22	-6.1(9)	$2U_{13}$
27(1)	30(1)	29(1)	17(1)	10(2)	9(1)
34(1)	19(2)	36(2)	$1/2U_{22}$	10(2)	0
31(1)	16(2)	24(2)	$1/2U_{22}$	1(1)	0
20(10)					
47(4)	U_{11}	370(30)	$1/2U_{11}$	0	0
100(10)	160(30)	250(30)	90(20)	-90(20)	-160(30)
53(4)	85(6)	100(7)	$1/2U_{22}$	12(4)	0
39(8)	U_{11}	20(10)	$1/2U_{11}$	0	0

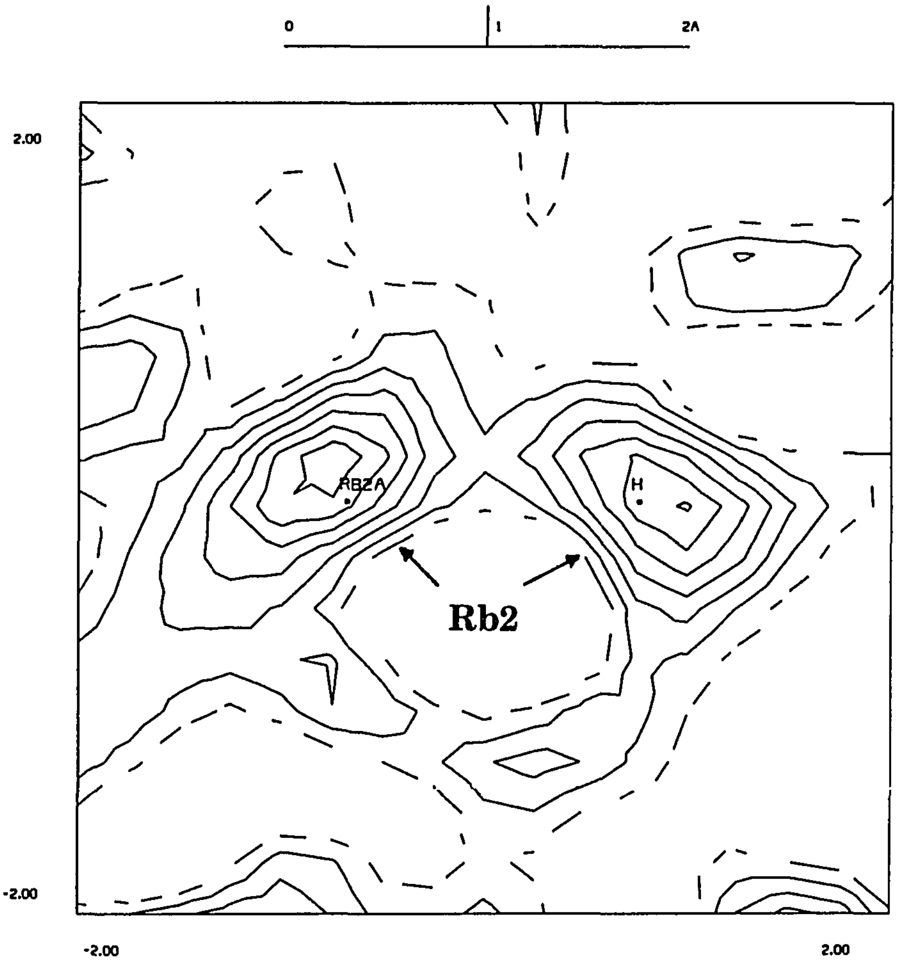

Figure 46. A plot (4 x 4 Å) of the observed electron density around Rb2 in $Rb_5Zr_6Br_{15}Be$. The plan is defined by Rb2, one of Rb2's symmetry equivalent position at (0.194, 0.166, 0.554), and one of Rb1's symmetry equivalent position at (0, 0, 0.321). The contour interval is 3 e/Å^3

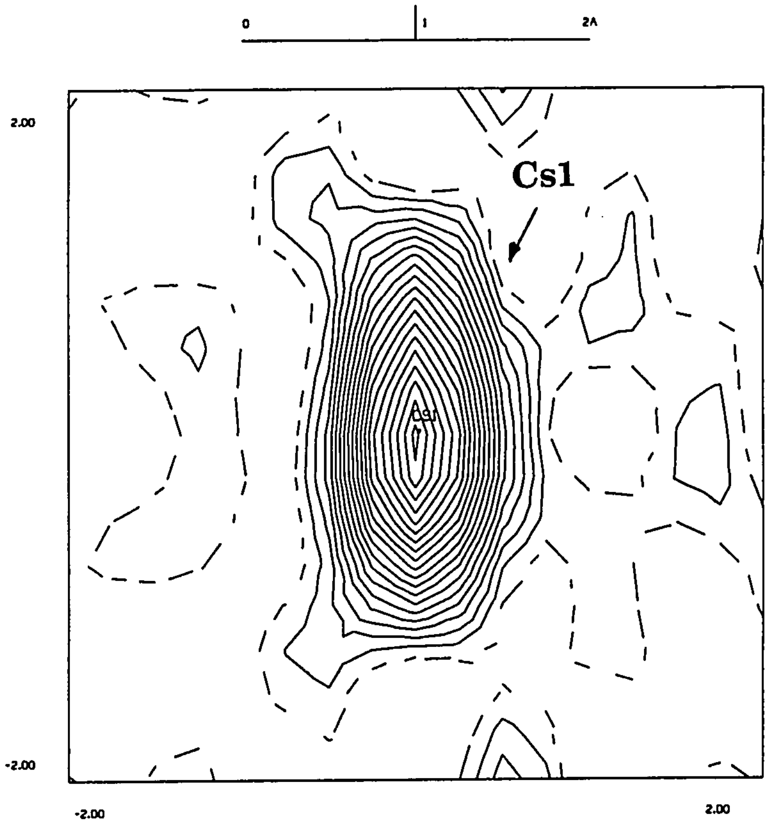

Figure 47. A 4 x 4 Å plot of the electron density around Cs1 in $Cs_{4.6}Zr_6Br_{15}Be$ calculated from F_{obs}. The plan is defined by Cs1, Br5, and a dummy atom at (0, 0, -0,01). The contour interval is 3 e/Å^3

as observed for Rb1, but there was no evidence for splitting, and the center of the electron density was right on the special position (0, 0, 1/4). However, the anisotropic refinement results indicated that one of the Br positions, Br4, which lay on the 2-fold axis, had a peculiar thermal ellipsoid. In other words, the symmetry for Br4 was too high and space group without that axis, i.e., $P6_3$, might be a better choice.

As expected, the refinement in $P6_3$ provided a better solution than in $P6_322$, for not only Br4 had a fairly spherical thermal ellipsoid but also the R and R_w values significantly decreased from 6.0% and 4.5% to 4.9% and 3.5%. As for Rb2 in $Rb_5Zr_6Br_{15}Be$, Cs2 was also on a general position which was close to (x, 0, 0) in the refinement in $P6_322$. In $P6_3$, however, the refined occupancies of unrelated Cs2a (18(1)%) and Cs2b (27(1)%) were different from each other by 6.4σ, which was more evidence for choosing the lower symmetry space group. As shown in the plot of the observed electron density around Cs2a and Cs2b (Figure 48), the electron density of Cs2a and Cs2b did overlap even though they preferred to be refined independently. Unlike the isotropic refinement, the anisotropically refined Cs2a and Cs2b positions were not on the electron density maximum but rather shifted off the maximum to an electron density valley between the real peak and a residual peak. Therefore, these two positions were isotropically refined. The final refinement converged at R=4.9% and R_w=3.5%. All the refined positional and thermal parameters are listed in Table 35. The final difference Fourier map was essentially flat with 1.8 e/Å^3 as its

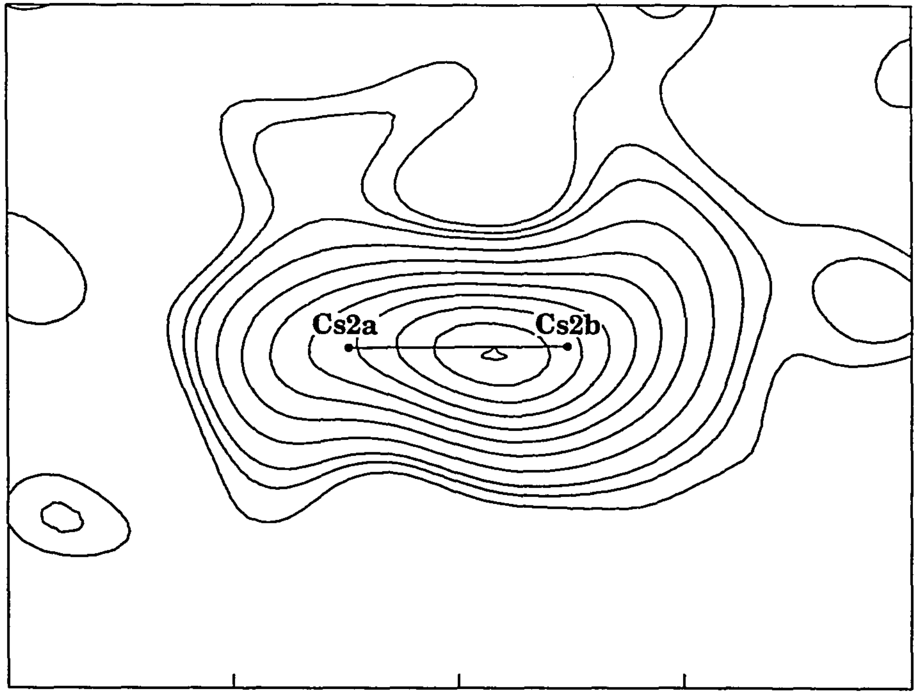

Figure 48. A 3 x 4 Å plot of the observed electron density around the two split Cs positions, Cs2a and Cs2b, in $Cs_{4.6}Zr_6Br_{15}Be$. The electron densities of Cs2a and Cs2b overlap with each other even though they prefer to be refined independently. The contour interval is 5 e/Å

Table 35. Positional and thermal parameters for $Cs_{4.60(8)}Zr_6Br_{15}Be$

Atom	Psn.	x	y	z	B_{eq}(Å^2)
Zra	6(c)	0.1844(2)	0.6648(2)	0.1367	1.06(8)
Zrb	6(c)	0.1845(2)	0.5196(2)	0.3635(2)	1.05(8)
Br1	6(c)	0.0002(2)	0.6669(2)	0.0022(7)	1.82(8)
Br2a	6(c)	0.4972(3)	0.3300(2)	0.4931(4)	1.6(1)
Br2b	6(c)	0.4976(3)	0.1674(2)	0.0052(4)	1.8(1)
Br3	6(c)	0.1664(3)	0.3333(2)	0.2475(5)	1.76(8)
Br4	6(c)	0.5018(3)	0.0038(2)	0.2477(4)	1.26(9)
Be	2(b)	1/3	2/3	0.272(4)	2(1)
Cs1[b]	2(a)	0	0	0.255(1)	10.7(5)
Cs2a[c]	6(c)	0.185(1)	0.031(2)	0.034(1)	5.6(5)
Cs2b[d]	6(c)	0.174(1)	0.153(1)	0.471(1)	7.6(4)
Cs3[e]	6(c)	0.3229(2)	0.1613(3)	0.2475(6)	4.0(1)
Cs4[f]	2(b)	2/3	1/3	0.252(1)	4.2(2)

[a] U x 10^3

[b] 60.0(9)% occupied

[c] 18(1)% occupied

[d] 27(1)% occupoed

[e] 76.1(3)% occupied

[f] 36.3(6)% occupied

U_{11}[a]	U_{22}	U_{33}	U_{12}	U_{13}	U_{23}
14(1)	16(1)	12(1)	9(1)	-4(1)	-3(1)
13(1)	12(1)	13(1)	6(1)	2(1)	-0(1)
22(1)	25(1)	21(1)	11(1)	-10(1)	6(1)
25(1)	17(1)	18(2)	10(1)	-5(1)	2(1)
30(2)	21(1)	20(2)	16(1)	5(1)	7(2)
23(1)	15(1)	28(1)	8.0(9)	7(1)	1(1)
22(1)	11(1)	11(2)	4.9(8)	2.3(8)	1(1)
20(10)					
37(2)	U_{11}	330(10)	$1/2U_{11}$	0	0
71(7)					
96(6)					
61(2)	37(1)	63(2)	30(1)	-6(2)	5(1)
67(4)	U_{11}	25(4)	$1/2U_{11}$	0	0

highest positive peak, 1.15 Å from Br5. The other enantiomer was checked, and discarded because of its higher R and R_w values (5.8% and 4.3%).

Structure Descriptions and Discussion: The most striking structural feature of this new 6-15 phase is the existence of huge one-dimensional tunnels in the lattice. Figure 49 is the projection of this hexagonal lattice on the ab plane of the Rb compound. As shown, the tunnel is created by six cluster units sharing the terminal bromine atoms, i.e., Br^{a-a}. The diameter of the tunnel is about 10 Å. One way to view this structure is to dissect it into close packed layers. Its c dimension corresponds to four layers stacked in ...ABCB... or $(hc)_2$. These layers are related to one another either by the 6_3 screw axis or the 2_1 screw axes perpendicular to the c direction. Each layer consists of twelve close packed sites within the unit cell. Layers A and C have nine Br and three Cs sites, while the B layer contains six Br, five Cs, and one interstitial sites. The Zr atoms sit in the octahedral site created by five Br and one interstitial atoms in the adjacent layers forming Zr_6Z cluster units. Moreover, the cluster units also form close packed layers which follow the ...ABAB... hexagonal packing sequence.

Figure 50 shows how the clusters from different layers are connected to form one-dimensional tunnels. Starting from the cluster in the center of Figure 50a, its three terminal Br atoms on the vertices of the top triangular face are shared by the three adjacent clusters from the B layer above it, and those three on the bottom triangle face are shared by the three neighboring cluster units

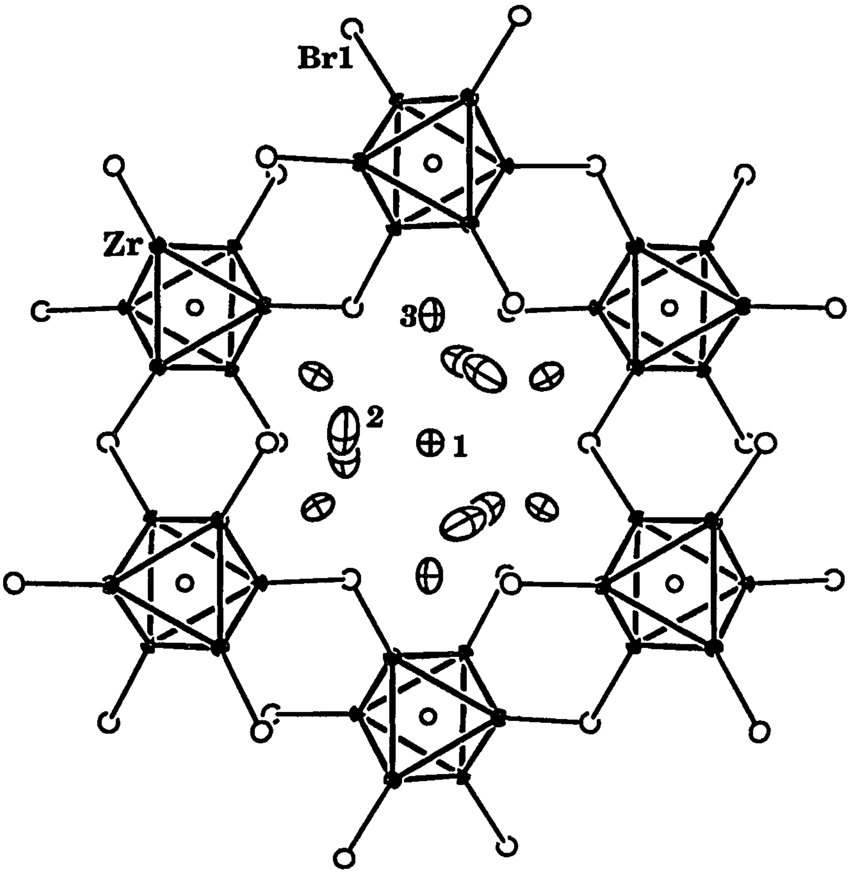

Figure 49. The [001] view of $Rb_5Zr_6Br_{15}Be$. The one-dimensional tunnel created by six clusters is stuffed by the Rb^+ cations (50% probability)

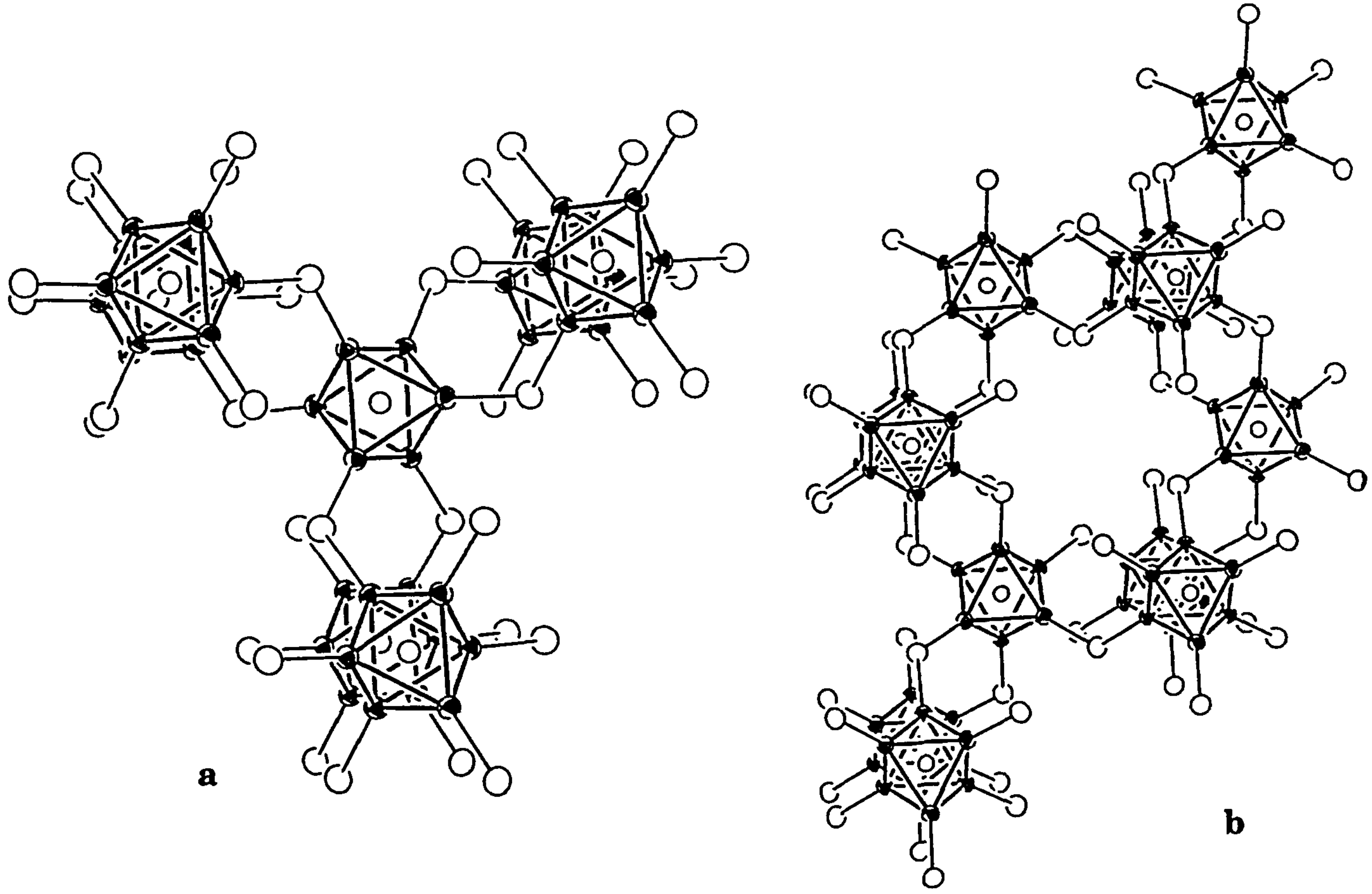

Figure 50. Part a shows the local environment around the cluster unit in $Rb_5Zr_6Br_{15}Be$. Such cluster connectivities create three half tunnels. Part b shows how the tunnel is created by the fragment in drawing a. The 3-fold axis is perpendicular to the page (90% probability)

from the B layer below it. All the Zr-Br^{a-a}-Zr bonds are bent with about 128° angles. One of the notable features here is that the three Zr-Br^{a-a}-Zr bonds on the top bend in the direction opposite to the bottom three. Such a cluster arrangement forms three half tunnels. As shown in Figure 50b, by connecting these half tunnels in the same fashion, a complete tunnel is created. Figure 51a demonstrates how the tunnels are linked on the ab plane. This is the first time such a cluster arrangement has been seen in any cluster halide.

If the cluster core $\{(Zr_6Z)Br^i_{12}\}$ is replaced by a single metal atom, the shape and the connectivity of the tunnels are similar to those in the hexagonal tungsten bronze, as shown in Figure 51b.[75] Yet, two major differences are noticed when these two structures are compared. Firstly, the orientations of the octahedra are different. In the hexagonal tungsten bronze, the 4-fold axes of WO_6 octahedron are lined up along the c axis or tunnel direction, while the 3-fold axes of $\{(Zr_6Z)Br^i_{12}\}Br^{a-a}_6$ are in the tunnel direction in this particular 6-15 phase. Secondly, the six WO_6 octahedra around the tunnel are in the same layer, whereas, the six $\{(Zr_6Z)Br^i_{12}\}$ clusters are positioned in two adjacent layers alternately.

In $Rb_5Zr_6Br_{15}Be$, Rb^+ atoms occupy four crystallographically different sites in the lattice with the symmetry best represented by $P6_322$. Three of them happen to be inside the tunnel. As illustrated in Figure 49, Rb1 occupies the site in the center of the tunnel. According to the refinement, the Rb1 position yields a short Rb1-Rb1 distance, 1.72 Å. Since Rb1 is 49(1)% occupied, the

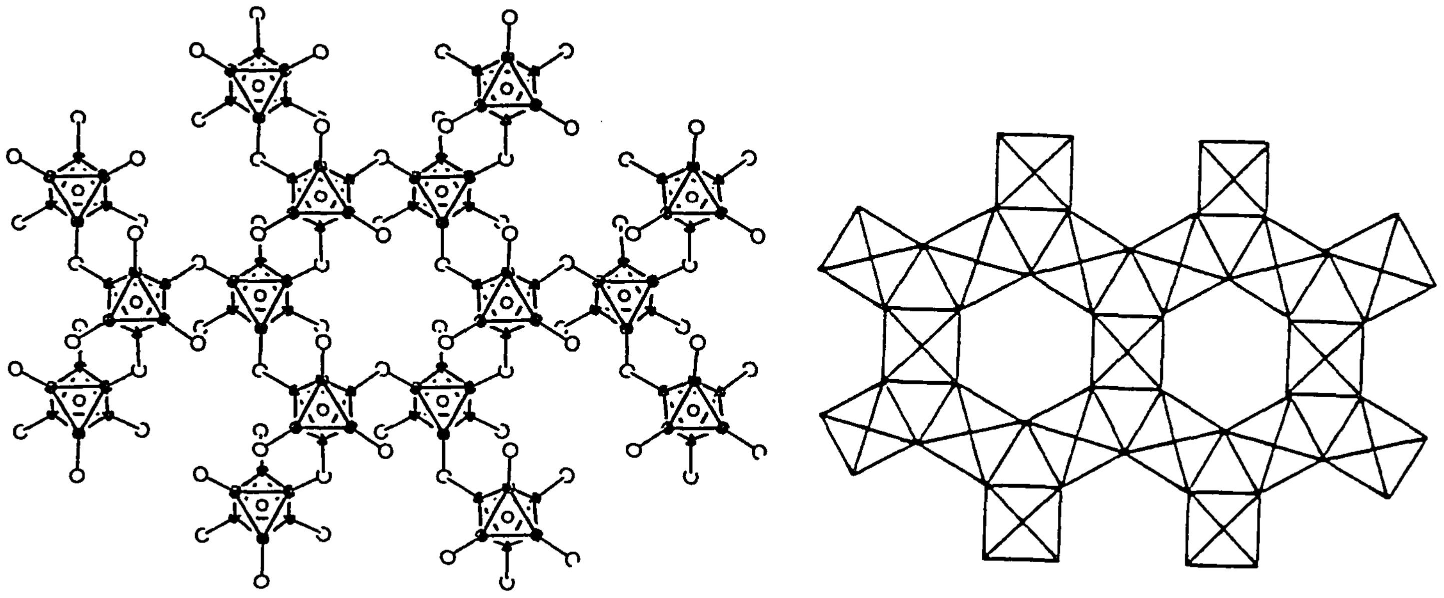

(a)

(b)

Figure 51. The comparison of the one-dimensional tunnels in $Rb_5Zr_6Br_{15}Be$ (a) and in hexagonal tungsten bronze WO_3 (b).[75] The views are along [001] directions

short Rb1-Rb1 distance could be the result of Rb1 hopping between those two sites or occupying half in a regular way over small region. Since Rb1 is far from the tunnel wall or far from the Br atoms bonded to the clusters, it has only three Br atoms (Br3) around its waist (Figure 52) at 3.808(7) Å (Table 36), which is equivalent to the tabulated distance for a fourteen-coordinate Rb^+.[76] Its particular coordination environment explains why Rb1 is disordered and has a very large thermal displacement along the tunnel direction ($U_{33}/U_{11} \sim 8$). More importantly, as mentioned earlier, the refined Rb1 position agrees very well with the observed electron density distribution around Rb1 (Figure 45).

As shown in Figure 49, the 31(1)% occupied Rb2 position is also disordered, which is similar to Rb1. It can also be accounted for by the bonding environment about Rb2. Since Rb2 is closer to the tunnel wall than is Rb1, in addition to the three Br atoms at $\bar{d}$=3.41 Å, it has a few more Br at relatively longer distances (one Br2 at 3.82(2) Å; one Br1 and one Br3 at 4.07 Å). The arrangement of these Br atoms, however, is rather unsymmetric. As shown in Figure 53, these Br atoms are only gathered on one side of the waist of Rb2, which illustrates why the ellipsoid of Rb2 is elongated. Again, the plot of the observed electron density distribution around Rb2 (Figure 46) indicates that the splitting or hopping is real. For both Rb1 and Rb2, the disorder could be caused by only having a few loosely bonded Br atoms in their neighborhood. Even though the disorder creates some short distances among the Rb atoms [d(Rb1-

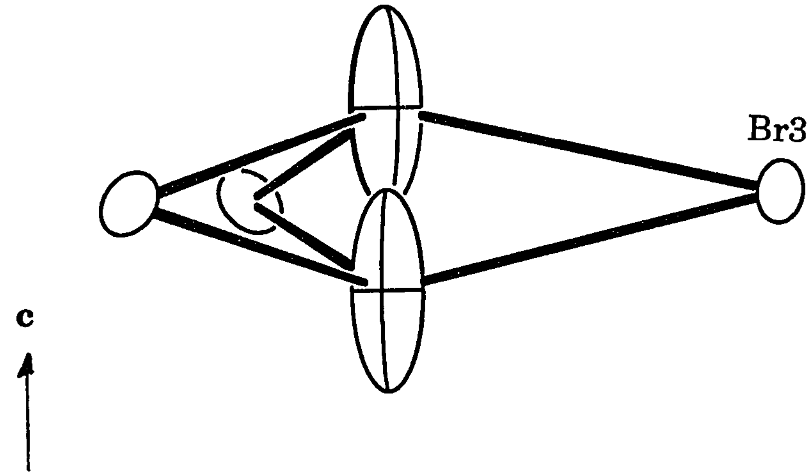

Figure 52. The local environment of Rb1 in $Rb_5Zr_6Br_{15}Be$ with C_3 symmetry. It only has three Br atoms at 3.81 Å. The loosely bonded Rb1 (50% occupied) is disordered between two symmetry-related sites (50% probability)

Table 36. Important bond distances (Å) and angles (°) for $Rb_{5.0(1)}Zr_6Br_{15}Be$

d(Zr-Zr)			d(Rb-Rb)[b]		
Zr-Zr	x2[a]	3.363(3)	Rb1-Rb1	x1	1.72(4)
	x1	3.345(4)		x3	3.67(2)
	x1	3.390(4)	-Rb2	x3	2.80(2)
$\bar{d}$		3.365	Rb1-Rb3	x3	3.652(9)
d(Zr-Be)	x1	2.380(2)	Rb2-Rb2	x1	1.44(4)
			-Rb3	x1	2.87(2)
d(Zr-Br^i)					
Zr-Br2	x2	2.703(3)	d(Br-Br)[c]		
	x2	2.722(3)	Br1-Br2	x2	3.850(4)
-Br3	x2	2.722(4)		x2	3.717(3)
-Br4	x2	2.710(4)	-Br3	x2	3.696(1)
d(Zr-Br^{a-a})			-Br4	x2	3.750(2)
Zr-Br1	x1	2.928(2)	Br2-Br2	x1	3.766(5)
d(Rb-Br)				x2	3.791(3)
Rb1-Br3	x3	3.808(7)	-Br3	x1	3.797(3)
Rb2-Br1	x1	3.46(3)	-Br4	x1	3.608(3)
-Br2	x1	3.46(1)		x1	3.849(3)
-Br3	x1	3.32(2)	Br3-Br4	x2	3.813(2)
$\bar{d}$		3.41			
Rb3-Br1	x2	3.699(1)	Zr-Zr-Zr	x1	60.00
-Br2	x2	3.711(5)		x1	59.39(8)
-Br3	x2	3.633(3)		x1	59.91(6)
-Br4	x2	3.831(4)		x1	89.61(5)
$\bar{d}$		3.718	Zr-Br1-Zr	x1	128.3(1)
Rb4-Br2	x6	3.641(2)	Br2-Zr-Br3	x2	167.4(1)
-Br4	x3	3.686(4)	Br2-Zr-Br4	x2	165.8(1)
$\bar{d}$		3.656			

[a] Number of times the distances and angles occur per atom

[b] d(Rb-Rb) < 3.65 Å

[c] d(Br-Br) < 3.85 Å

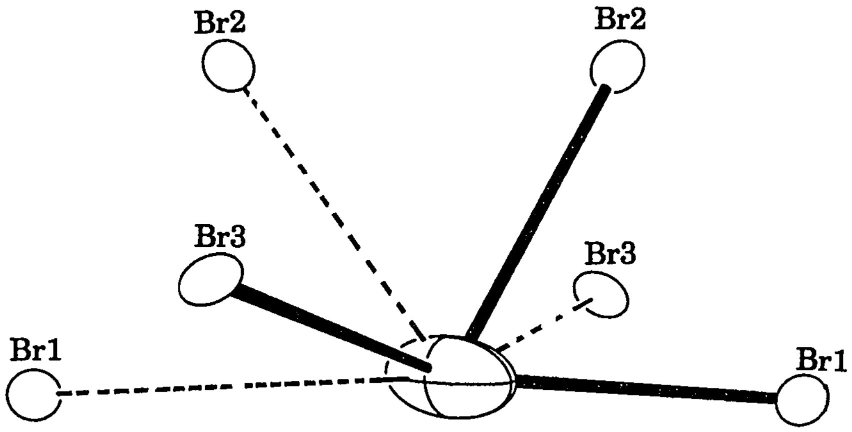

Figure 53. The local environment of Rb2 in $Rb_5Zr_6Br_{15}Be$, which is on a general position. As shown, the arrangement of the Br neighbors are very asymmetric. The disordered Rb2 only has three close Br neighbors. The other three joined by dotted lines are at > 3.8 Å (50% probability)

Rb2)=2.80(2) Å, d(Rb2-Rb3)=2.87(2) Å], the situation is not very critical, as all of the Rb positions in $Rb_5Zr_6Br_{15}Be$ are partially occupied.

The best behaved Rb^+ cation inside the tunnel is Rb3 which lies closest to the tunnel wall. It has a C_2 point symmetry and eight Br atoms symmetrically around it (Figure 54). The average Rb3-Br distance is 3.718 Å which is 0.15 Å longer than the summation of the corresponding Rb^+ and Br^- crystal radii (Rb^+(VIII), 1.75 Å; Br^-(VI), 1.82 Å). The occupancy of Rb3 refined as 64(1)%.

Rb4 is the only Rb position that is not inside the tunnel but rather embedded in the tunnel wall. As indicated in Figure 55, it is right in between the clusters from the same type of layers (AA or BB), serving as a binding force to hold together negatively charged cluster units. To share the terminal Br atoms ($Br^{a\text{-}a}$) is another effective way to "glue" negatively charged clusters into the lattice. Rb4 has a D_3 point symmetry and six Br atoms at the distance 3.641(2) Å plus three more at a slightly longer distance, 3.686(4) Å. The average Rb4-Br distance is 3.656 Å which is longer than expected for a nine-bonded Rb^+ (Rb^+(IX), 1.77 Å; Br^-(VI), 1.82Å). The refined occupancy of Rb4 is 29(1)%. Based on the refined occupancies of all the Rb sites, this phase has a composition of $Rb_{5.0(1)}Zr_6Br_{15}Be$, which yields a 16e$^-$ cluster phase.

The cluster unit has D_3 symmetry. The average Zr-Zr distance is 3.365 Å, and that of Zr-Be is 2.380 Å, which are both very comparable with those in $Rb_3Zr_6Br_{15}Be$, 3.360 Å and 2.376 Å, respectively. The Zr-$Br^{a\text{-}a}$ distance is 2.928(2) Å, longer than those of Zr-Br^i, which range from 2.703(3) Å to 2.722(3) Å.

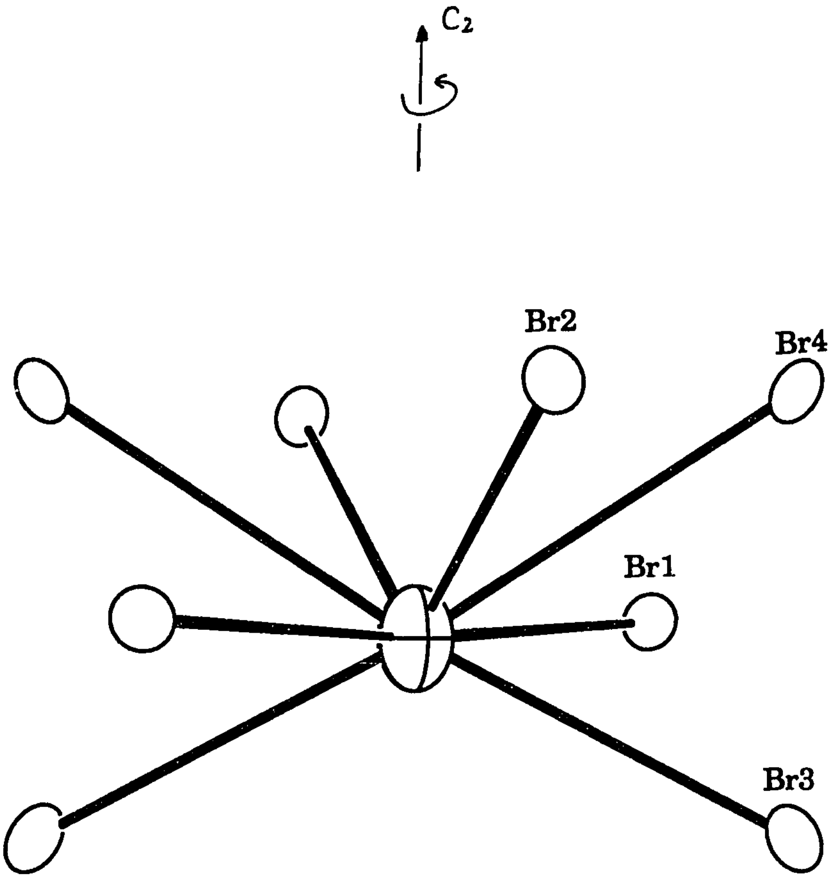

Figure 54. The local environment of Rb3 in $Rb_5Zr_6Br_{15}Be$. It has C_2 point symmetry and eight Br neighbors (50% probability)

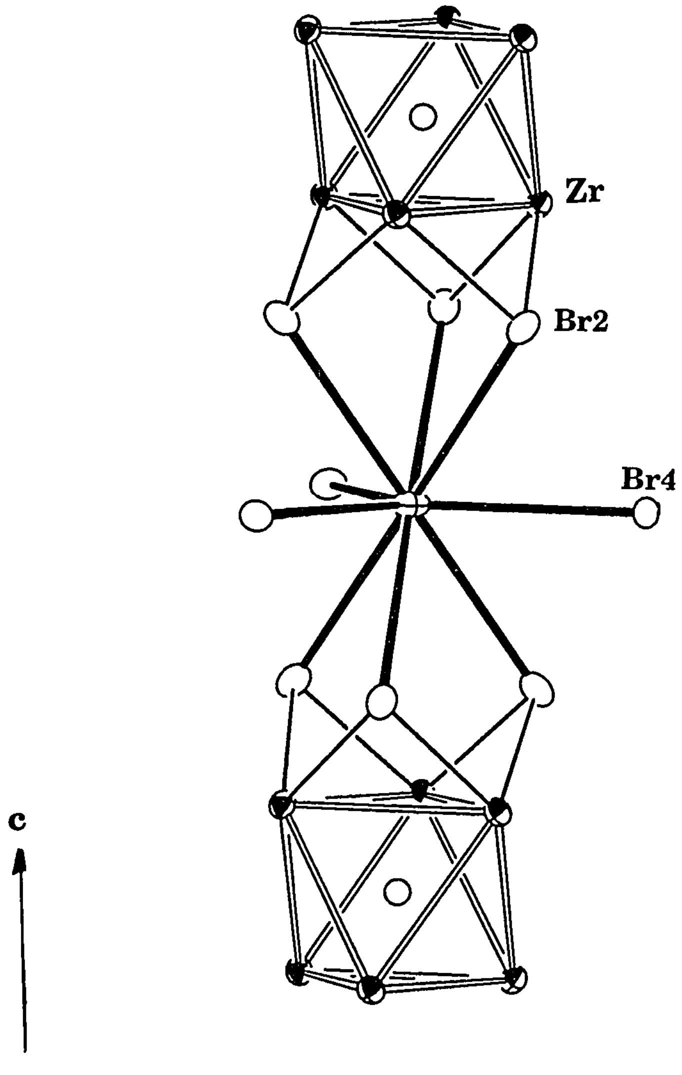

Figure 55. The environment around Rb4 in the lattice of $Rb_5Zr_6Br_{15}Be$. It is right in between the clusters from the same type of layers (50% probability)

As mentioned before, the structure refinement in space group $P6_3$ provided a better solution for the Cs-containing phase. The Zr-Br framework is essentially the same as that of $Rb_5Zr_6Br_{15}Be$. The differences are on some of the cation sites, i.e., Cs1 and Cs2. As demonstrated by the observed electron density distribution (Figure 47) as well as the refinement (Table 35), the thermal displacement of Cs1 along the tunnel direction is also bigger than that in the other directions ($U_{33}/U_{11} \sim 9$); however, it does not split as Rb1 does. Cs1 has three Br atoms (Br3) around its waist at 3.783(2) Å which distance is equivalent to a ten-coordinate Cs^+ (Table 37). The arrangement of these three Br3 atoms explains why Cs1 has an elongated thermal ellipsoid along the tunnel direction. The occupancy of Cs1 refined as 60.0(9)%.

Cs2a and Cs2b, which correspond to Rb2 in $Rb_5Zr_6Br_{15}Be$, are disordered cation sites (Figure 48). The disorder of these sites is one of the major reasons for lowering the symmetry of the Cs-containing phase from $P6_322$ to $P6_3$. According to the refinement, Cs2a and Cs2b are indeed not related by a 2-fold axis anymore, for their positional x positional parameters differ from each other by 7.8σ, and their refined occupancies, 18(1)% and 27(1)%, respectively, are also different by 6.4σ. The bonding environment, or the arrangement of the adjacent Br atoms around Cs2a and Cs2b is very similar to that of Rb2. The fine scale variation is that the average distance between Cs2b and three adjacent Br atoms is 3.63 Å, slightly longer than that for Cs2a, 3.54 Å.

Table 37. Important bond distances (Å) and angles (°) for $Cs_{4.60(8)}Zr_6Br_{15}Be$

d(Zr-Zr)		
Zra-Zra	x2[a]	3.359(4)
-Zrb	x1	3.350(2)
	x1	3.391(2)
Zrb-Zrb	x2	3.359(4)
$\bar{d}$		3.365
d(Zr-Be)		
Zra-Be	x1	2.54(3)
Zrb-Be	x1	2.24(3)
$\bar{d}$		2.39
d(Zr-Br^i)		
Zra-Br2a	x1	2.709(4)
		2.725(4)
-Br3	x1	2.696(4)
-Br4	x1	2.700(4)
Zrb-Br2b	x1	2.693(4)
	x1	2.709(4)
-Br3	x1	2.725(5)
-Br4	x1	2.730(4)
d(Zr-Br^{a-a})		
Zra-Br1	x1	2.927(5)
Zrb-Br1	x1	2.960(5)
d(Cs-Br)		
Cs1-Br3	x3	3.783(2)
Cs2a-Br1	x1	3.45(2)
-Br2b	x1	3.58(2)
-Br3	x1	3.59(2)
$\bar{d}$		3.54
Cs2b-Br3	x1	3.56(1)
Cs2b-Br2a	x1	3.68(1)
-Br3	x1	3.64(1)
$\bar{d}$		3.63
Cs3-Br1	x1	3.701(6)
	x1	3.789(6)
-Br2a	x1	3.738(6)
-Br2b	x1	3.707(6)
-Br3	x1	3.721(6)
	x1	3.729(6)
-Br4	x1	3.821(6)
	x1	3.826(6)
$\bar{d}$		3.754
Cs4-Br2a	x3	3.67(1)
-Br2b	x3	3.72(1)
-Br4	x3	3.740(2)
$\bar{d}$		3.71
d(Cs-Cs)[b]		
Cs1-Cs2a	x3	3.50(2)
-Cs2b	x3	3.40(2)
Cs3-Cs2a	x1	3.13(2)
-Cs2b	x1	3.31(2)
Cs2a-Cs2b	x1	0.98(1)
	x1	3.56(1)
Zra-Zra-Zra	x1	60.00
Zra-Zra-Zrb	x1	90.36(7)
	x1	59.51(7)
Zra-Br1-Zrb	x1	130.4(1)
Br2a-Zra-Br3	x2	167.0(2)
Br2a-Zra-Br4	x2	165.3(1)
Br2b-Zrb-Br3	x2	168.1(2)
Br2b-Zrb-Br4	x2	166.3(1)

[a] Number of times the distances and angles occur per atom

[b] d(Cs-Cs) < 3.65 Å

The environment of Cs3 is similar to that of Rb3 which has a C_2 point symmetry, but not exactly the same. As reflected by the Cs3-Br distances (Table 37), the Cs3 site shows significant distortion from C_2 symmetry. The average distance between Cs3 and its eight Br neighbors is 3.754 Å, slightly longer than the sum of the corresponding crystal radii of Cs^+(VIII) and Br^-(VI), 3.70 Å. Cs4 has a D_3 symmetry and the average Cs4-Br distance is 3.71 Å which is nearly ideal for a nine-coordinate Cs^+. In contrast, all the cation sites in $Rb_5Zr_6Br_{15}Be$ are too large for Rb^+. The occupancies of Cs3 and Cs4 refined as 76.1(3)% and 36.3(6)%, respectively. The refined occupancies of all the Cs sites yield a composition of $Cs_{4.60(8)}Zr_6Br_{15}Be$. Considering the relatively large errors on the refined cation occupancies, it is virtually a 16e$^-$ cluster phase. The magnetic study also suggests that the cluster unit (Zr_6Be) has about 16 electrons in its cluster bonding orbitals.

The cluster core (Zr_6Be) in $Cs_{4.6}Zr_6Br_{15}Be$ has a D_3 symmetry. It indicates once again that the lattice distortion (from $P6_322$ to $P6_3$) is caused by the Cs cations. The average Zr-Zr distance is 3.365 Å, and that of Zr-Be is 2.39 Å, almost identical to those in $Rb_5Zr_6Br_{15}Be$, 3.365 Å and 2.380 Å, respectively. The relatively large error on the distance of Zr-Be was the result of refining the z parameter of Be in $P6_3$. The refinement on the light atom in a heavy network as Zr-Br always has large standard deviations. The same phenomenon has been observed in(Cs_4Br)$Zr_6Br_{16}B$.

Magnetic Susceptibility Study: Magnetic susceptibility measurements were performed on the sample from which the data crystal was found. The loaded stoichiometry was $Cs_4Zr_6Br_{15}Be$. A large chunk of the target phase could be easily separated from the rest. As shown in Figure 56, its magnetic moment is essentially independent of temperature. Since these cluster phases are not electric conductors, the temperature-independent behavior indicates that there are no unpaired, localized electrons in the cluster bonding orbitals. In other words, $Cs_{4.60(8)}Zr_6Br_{15}Be$ is practically a 16e cluster phase. After the diamagnetic core correction was applied, the temperature-independent χ_{TIP} was calculated as $4.68(1)x10^{-4}$ (cgsu), which is not what is expected for diamagnetic materials. This kind of phenomenon, however, has been observed for other cluster phases as well.[73] As discussed for $Cs_{3.4}Zr_6Br_{15}B$, the temperature-independent paramagnetism is caused by a mixing of excited-state wave functions with those of the ground state in the presence of the magnetic field, the so called Van Vleck paramagnetism. The χ_{TIP} value of $Cs_{4.60(8)}Zr_6Br_{15}Be$ is comparable with that of $Cs_{3.4}Zr_6Br_{15}B$, $5.41(2)x10^{-4}$ (cgsu), and also with those of Nb and Ta halide cluster compounds.[73]

Structure Comparisons: Even though the seven bromide 6-15 type cluster phases discussed in this section belong to three different structure types, they exhibit several noticeable structural similarities. Firstly, the cluster units in these 6-15 phases all share the same local connectivity which can be expressed as $(Zr_6Z)Br^{i}_{12}Br^{a\text{-}a}_{6/2}$. Secondly, none of the clusters in the first bonding

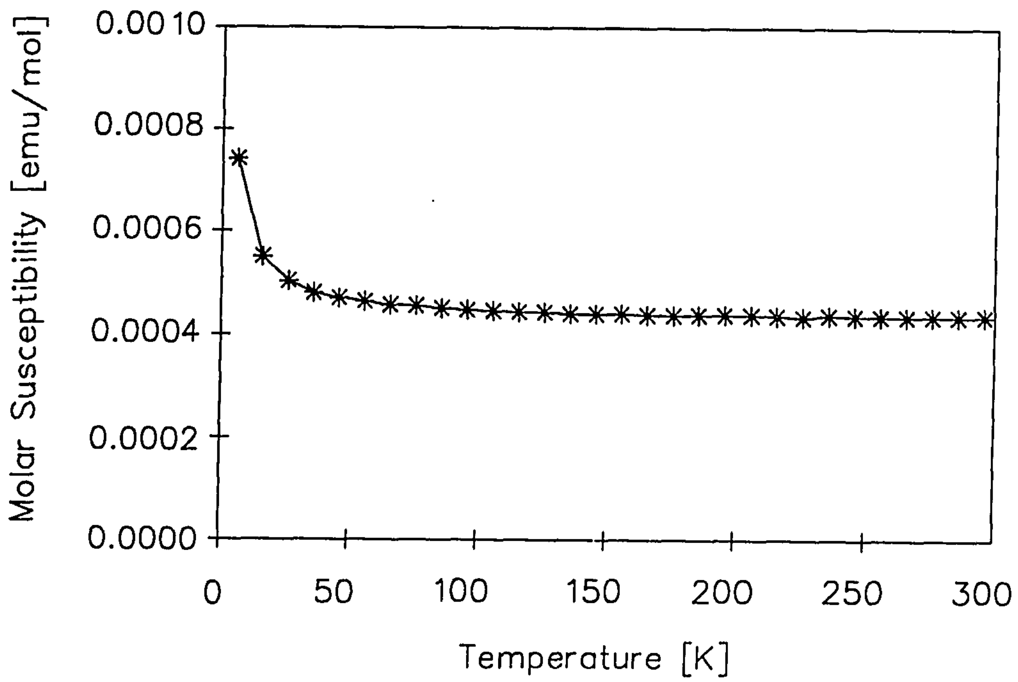

Figure 56. A plot of the magnetic susceptibility of $Cs_{4.60(8)}Zr_6Br_{15}Be$, corrected for ion core diamagnetism. It has a temperature-independent paramagnetic behavior with χ_{TIP} as 4.68(1)x10^{-4} (cgsu)

sphere (defined as the six clusters which are connected to the same central cluster unit) is directly linked to each other (Table 23). Finally, the connections among the clusters all lead to the formation of one-dimensional tunnels in three-dimensional frameworks, and these one-dimensional tunnels are all occupied by alkali-metal countercations.

Their structural differences, on the other hand, are at least as distinctive as the similarities mentioned above. First of all, these three structure types exhibit different lattice symmetries and different kinds of one-dimensional tunnels. Also, the local geometries of the bridge bonds (Zr-$Br^{a\text{-}a}$-Zr) are different as well, for $Rb_3Zr_6Br_{15}Be$ and $K_3Zr_6Br_{15}Be$ have 33% linear and 67% bent bridge bonds, whereas the other two structure types contain only bent bridge bonds. More importantly, the indirect linkages among the six clusters in the first bonding sphere (FBS) for these three structure types are not the same either. Each FBS cluster in $Cs_3Zr_6Br_{15}C$ is connected to four other FBS clusters through one additional cluster as in Nb_6F_{15}.[69] In $Rb_3Zr_6Br_{15}Be$, however, one finds the number of clusters indirectly connected is dependent on whether the chosen cluster is connected to the central cluster through a linear $Br^{a\text{-}a}$ bridge or a bent bridge. Clusters linearly bridged to the central cluster are indirectly connected to two other FBS clusters, while clusters connected through a bent $Br^{a\text{-}a}$ bridge are indirectly joined to three others.[69] As shown in Figure 57, each FBS cluster in $Rb_5Zr_6Br_{15}Be$ is indirectly connected to three other FBS clusters. In fact, the indirect linkage among the clusters in the first bonding

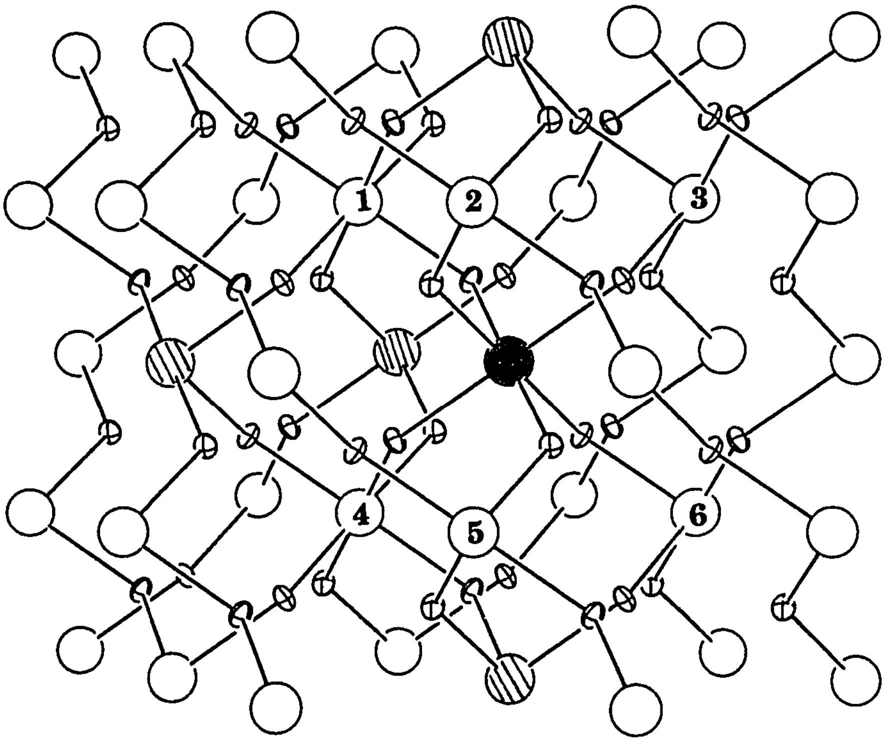

Figure 57. A schematic representation of the cluster connectivity in the lattice of $Rb_5Zr_6Br_{15}Be$. The large filled circle stands for the central $Zr_6Br^{i}_{12}Be$ cluster, and small hatched spheres, bridging $Br^{a\text{-}a}$. First bonding sphere (FBS) clusters are represented by the large open circles labeled 1-6, and the large cross-hatched spheres indirectly connect FBS clusters

sphere is the most important criterion by which to identify $Cs_{4.6}Zr_6Br_{15}Be$ and $Rb_5Zr_6Br_{15}Be$ as members of a new 6-15 structure type. Comparing $Rb_3Zr_6Br_{15}Be$ with $Rb_5Zr_6Br_{15}Be$, the only difference appearing in the formula is the Rb content. In other words, the choice of the phase formation is determined by the amount of the countercations loaded in the reactions. The same is true for $Cs_{3.4}Zr_6Br_{15}B$ and $(Cs_4Br)Zr_6Br_{16}B$. In addition, the size of countercations plays an important role, for the structure type of $Cs_3Zr_6Br_{15}C$ could not be realized with smaller cations, e.g. Rb^+ or K^+, and Cs^+ could not be incorporated into the lattice of $Rb_3Zr_6Br_{15}Be$ either. Therefore, the formation of these phases is cation directed.

6-14 Type

Up to now, two different kind of 6-14 structure types have been found in the early transition-metal and rare-earth metal halide cluster systems. The one found in the La-I system recently has a layered network with the cluster connectivities expressed as $[(La_6Z)I^{i}_{8}I^{i-a}_{4/2}]I^{a-i}_{4/2}I^{a}_{2}$.[77] The other one is the well known Nb_6Cl_{14} or MNb_6Cl_{14} type. Three Nb_6Cl_{14} or Mnb_6Cl_{14} type zirconium bromide cluster compounds, i.e., $Zr_6Br_{14}C$, $CsZr_6Br_{14}C$, and $Zr_6Br_{14}Fe$, had been prepared in the previous studies.[35] This type of 6-14 structure has been one of the most diverse structure types, as it can be realized in the zirconium chloride, bromide as well as iodide systems with a wide range of interstitial elements.[19,20,33] With two of the inner bromine and four terminal bromine atoms involved in cluster connections, the unique three-dimensional network is formed,which can be precisely expressed as $[(Zr_6Z)Br^{i}_{10}Br^{i\text{-}a}_{2/2}]Br^{a\text{-}i}_{2/2}Br^{a\text{-}a}_{4/2}$. It has been noticed that countercations with different sizes prefer different sites in the lattice of Nb_6Cl_{14} type compounds. According to the results in the zirconium–chloride systems,[78] the smaller cations favor the octahedral sites between the halogen layers, while the larger cations tend to occupy the 12-coordinate positions within the anion layers.

Recent investigations in the zirconium bromide system provided eight more cluster phases with the Nb_6Cl_{14} type of structure Their Guinier lattice parameters are compiled in Table 38. Single crystal structure refinements were carried out on $CsZr_6Br_{14}Mn$ to study how the bromide lattice affects the metal-metal bonds in the clusters. Furthermore, it is also the first single crystal structure refinement on a transition-metal stabilized bromide cluster compound.

$CsZr_6Br_{14}Mn$

Syntheses: A high yield (>95%) of $CsZr_6Br_{14}Mn$ was prepared from a stoichiometric reaction carried out at 850°C for three weeks. The single crystal of this phase studied, however, was found in the reaction loaded as $Cs_4Zr_6Br_{16}Mn$. In order to study the cation preference in the lattice of 6-14 bromide phases centered by main-group elements, a series of $MZr_6Br_{14}B$, where M=Li, Na, K, Rb, or Cs, was prepared from stoichiometric reactions. The rest of the 6-14 bromide phases listed in Table 38 were synthesized with high yields as well.

Table 38. Guinier lattice parameters (Å) and volumes (Å^3) for $MZr_6Br_{14}Z$[a]

	a	b	c	V	cation site[b]
$Zr_6Br_{14}C$ [35]	14.690(3)	13.229(3)	11.991(3)	2330(1)	–
$NaZr_6Br_{14}C$	14.6876(9)	13.2266(8)	11.9864(8)	2328.6(2)	b
$RbZr_6Br_{14}C$	14.719(1)	13.287(1)	12.043(1)	2355.2(4)	b
$CsZr_6Br_{14}C$ [35]	14.737(1)	13.297(2)	12.108(1)	2372.7(5)	b
$LiZr_6Br_{14}B$	14.954(1)	13.2904(9)	12.0531(9)	2395.5(3)	a
$NaZr_6Br_{14}B$	14.789(1)	13.311(1)	12.045(1)	2371.2(4)	b
$KZr_6Br_{14}B$	14.7906(9)	13.2961(8)	12.0576(8)	2371.2(3)	b
$RbZr_6Br_{14}B$	14.807(2)	13.297(1)	12.117(1)	2385.6(4)	b
$CsZr_6Br_{14}B$	14.827(2)	13.306(2)	12.184(2)	2403.6(5)	b
$Zr_6Br_{14}Fe$ [35]	14.988(3)	13.408(2)	12.232(2)	2458.1(7)	–
$CsZr_6Br_{14}Mn$	15.062(1)	13.483(2)	12.387(1)	2515.6(5)	b

[a] Guinier powder diffraction data, space group Cmca.

[b] a denotes the Li position in $LiZr_6Cl_{14}Mn$ [77] and b, that for Cs in $CsZr_6Br_{14}Mn$.

Single Crystal Structure Studies: Prior to the data collection, an oscillation photo was taken on a Weissenberg camera to check the quality of the crystal. Data collection was conducted on an ENRAF NONIUS CAD4 diffractometer. The 25 peaks located during SEARCH could be indexed on the basis of a primitive triclinic cell which was transformed to the expected C-centered orthorhombic cell. Two octants (±h,k,l)of data were collected with an ω-θ scan mode. Besides the C-centered extinction h+k=2n+1, others, i.e., h,l=2n+1 for h0l; h,k=2n+1 for hk0; and l=2n+1 for 00l were observed in the data as well. Under these extinctions, the only possible space groups are C2cb (no.41) and Cmca (no.64). Since $CsZr_6Br_{14}Mn$ is presumably isostructural with $CsNb_6Cl_{14}$, the Cmca known for the latter, was chosen. After Lorentz and polarization corrections were performed, an empirical absorption correction was applied to the data based on three averaged ψ-scan measurements. The data set thus prepared was averaged in the corresponding point group mmm with R_{ave}=4.4% (all data).

The atom positions obtained from $Zr_6Cl_{14}B$ were utilized as an initial model, and the origin of the cell was filled with Cs as in the case of $CsNb_6Cl_{14}$. The isotropic refinements converged at R=6.8% and R_{ave}=7.6%, and the anisotropic refinements went smoothly and converged at R=3.4% and R_{ave}=3.7%. The occupancy of Cs refined to 102.4(7)% and was fixed at unity in the final refinement. A secondary extinction coefficient was refined at the final stage of the refinement, and the difference Fourier map was calculated as well. The largest positive peak on the map was 1.8 e/Å^3, 1.2 Å from Br4. The other important data collection and structure refinement results can be found in Table 39, and the refined atom positions as well as anisotropic thermal parameters are listed in Table 40.

Structure Description: The description of 6-14 (Nb_6Cl_{14}) structure can be found elsewhere.[6] An alternative way to describe this structure is that it contains two-dimensional cluster slabs stacking in a staggered way, or in ...ABAB..., along the c direction (Figure 58). Interestingly, the clusters within each layer are not connected directly, rather linked through the clusters in the layers above and below, via $Br^{a\text{-}a}$ and $Br^{a\text{-}i}$. The cluster units in $CsZr_6Br_{14}Mn$ have a C_{2h} point symmetry for the differences of the symmetry inequivalent bond distances are within 1.1σ. The distortion from an ideal octahedron is caused by the asymmetric environment, namely two different kind of inner Br atoms, i.e., Br^i and $Br^{i\text{-}a}$. The Zr-Zr bonds bridged by $Br^{i\text{-}a}$ are 3.535(3) Å, significantly longer (about 23σ) than those bridged by Br^i, 3.443(2)-3.448(2) Å (Table 41). Since Br4 ($Br^{i\text{-}a}$ and $Br^{a\text{-}i}$) are three-bonded, the Zr-Br4 distances, 2.773(2) Å and 3.058(3) Å, are noticeably longer than $\bar{d}(Zr\text{-}Br^i)$ and $d(Zr\text{-}Br^{a\text{-}a})$, which are 2.701 Å and 2.844(2) Å, respectively.

The average Zr-Zr and Zr-Mn distances are 3.459 Å and 2.446 Å in $CsZr_6Br_{14}Mn$, about 0.062 Å and 0.044 Å longer than those in $LiZr_6Cl_{14}Mn$. The lengthening of the bonds, again, is caused by the different matrix effect between the bromide and the chloride lattices for the average trans $Br^i\text{-}Zr\text{-}Br^i$ angle in

Table 39. Crystal data for $CsZr_6Br_{14}Mn$

space group, Z	Cmca (no. 64), 4
cell parameters[a]	
a (Å)	15.062(1)
b	13.483(2)
c	12.387(1)
V (Å^3)	2515.6(5)
crystal dimens. (mm)	0.16 x 0.16 x 0.30
octants measured	±h, k, l
2θ (max.), deg.	50
reflections	
measured	2735
observed (I/σ(I)>3.0)	1372
indep.	778
abs. coeff. (Mo Kα, cm^{-1})	262.63
transm. coeff. range	0.82-1.00
no. variables	59
R_{ave}, % (all data)	4.4
sec. extinct. coeff.	7.2(2) x 10^{-8}
R, %	3.4
R_w, %	3.7

[a] Guinier data

Table 40. Positional and thermal parameters for $CsZr_6Br_{14}Mn$

Atom	Psn.	x	y	z	B_{eq}(Å^2)
Zr1	16(g)	0.38299(8)	0.07163(9)	0.8848(1)	0.65(5)
Zr2	8(f)	0	0.3524(1)	0.8908(2)	0.76(7)
Br1	16(g)	0.1249(1)	0.0866(1)	0.2498(1)	1.18(6)
Br2	16(g)	0.1248(1)	0.2545(1)	0.0052(1)	1.23(6)
Br3	8(e)	1/4	0.3442(2)	1/4	1.4(1)
Br4	8(e)	0	0.1611(1)	0.7581(2)	1.1(1)
Br5	8(d)	0.2465(1)	0	0	1.3(1)
Mn	4(b)	1/2	0	0	0.7(2)
Cs	4(a)	0	0	0	2.1(1)

[a] U x 10^3

U_{11}[a]	U_{22}	U_{33}	U_{12}	U_{13}	U_{23}
8.7(6)	9.9(6)	7.7(6)	0.8(5)	-0.8(7)	0.6(6)
10(1)	9.7(9)	9(1)	0	0	-1(1)
16.8(8)	15.2(7)	13.0(7)	2.1(6)	5.1(7)	3.8(6)
16.5(7)	12.0(7)	18.2(7)	5.2(6)	-4.2(6)	-1.9(5)
16(1)	17(1)	20(1)	0	-9(1)	0
13(1)	17(1)	13(1)	0	0	-7(1)
9(1)	23(1)	16(1)	0	0	5(1)
10(2)	10(2)	7(2)	0	0	1(2)
26(1)	33(1)	22(1)	0	0	3(1)

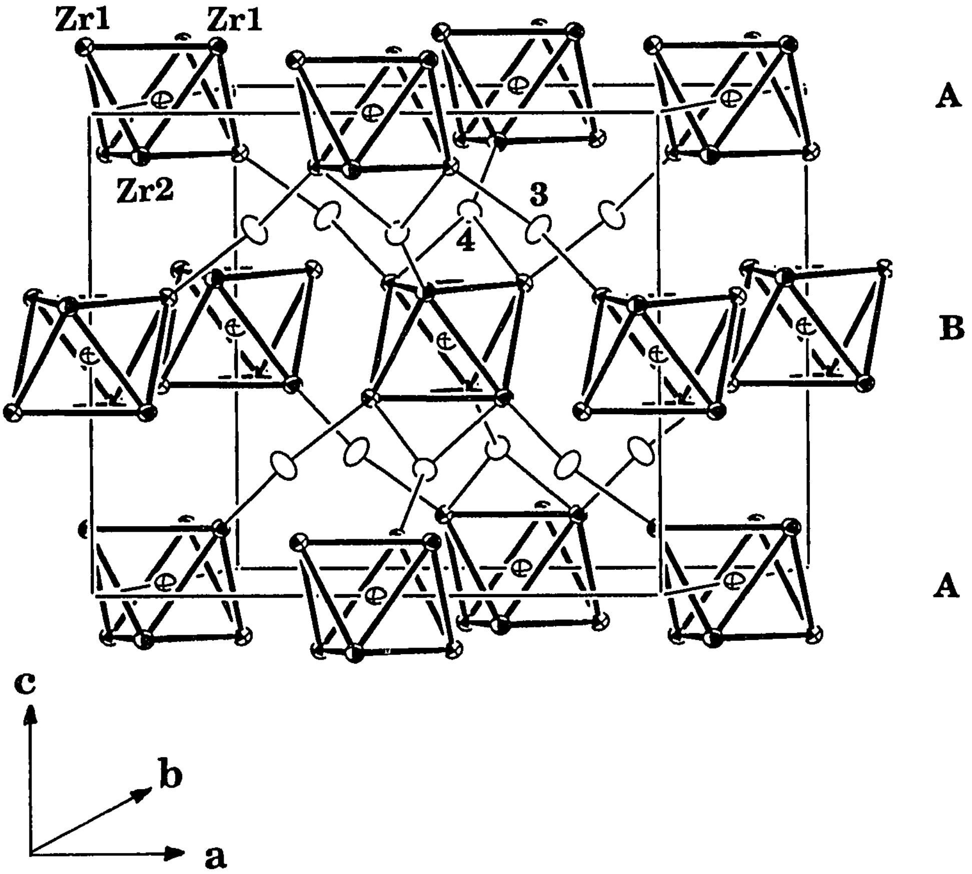

Figure 58. The unit cell of $CsZr_6Br_{14}Mn$, emphasizing the cluster connectivities. All the Cs atoms which are on the origin and the face centers are omitted in the picture. The open and shaded circles represent B and Zr, respectively, and crossed ellipsoids for Mn atoms. The cluster slabs are normal to the c direction, stacking in ...ABAB... (90% probability)

Table 41. Important bond distances (Å) and angles (°) in $CsZr_6Br_{14}Mn$

d(Zr-Zr)					
Zr1-Zr1	x1[a]	3.447(2)	d(Cs-Br)		
	x1	3.525(3)	Cs-Br1	x4	3.805(2)
Zr1-Zr2	x1	3.443(2)	-Br2	x4	3.914(2)
	x1	3.448(2)	-Br4	x2	3.701(2)
$\bar{d}$		3.459	-Br5	x2	3.714(2)
d(Zr-Mn)			$\bar{d}$		3.809
Zr1-Mn	x1	2.465(1)	d(Br-Br)[b]		
Zr2-Mn	x1	2.407(2)	Br1-Br1	x1	3.764(4)
$\bar{d}$		2.446	-Br1	x1	3.768(4)
d(Zr-Br^i)			-Br2	x1	3.781(2)
Zr1-Br1	x1	2.714(2)	-Br3	x1	3.773(2)
-Br2	x1	2.714(2)	-Br5	x1	3.780(2)
-Br5	x1	2.682(2)	Br2-Br2	x1	3.761(3)
Zr2-Br1	x2	2.696(2)		x1	3.775(3)
-Br2	x2	2.699(2)	-Br3	x1	3.769(2)
d(Zr-$Br^{i\text{-}a}$)			Br3-Br4	x2	3.7676(4)
Zr1-Br4	x1	2.773(2)	-Br5	x2	3.743(1)
d(Zr-$Br^{a\text{-}i}$)					
Zr2-Br4	x1	3.058(3)	Br1-Zr1-Br2	x1	170.63(7)
d(Zr-$Br^{a\text{-}a}$)			Br4-Zr1-Br5	x1	169.43(6)
Zr1-Br3	x1	2.844(2)	Br1-Zr2-Br1	x1	167.32(9)
			average		169.13

[a] Number of times the distances and angles occur per atom

[b] d(Br-Br) < 3.8 Å

$CsZr_6Br_{14}Mn$ is 169.13°C, 3.31°C smaller than that in $LiZr_6Cl_{14}Mn$, 172.44°C. Owing to the larger size of Mn, the average value of trans Br^i-Zr-Br^i angle is about 3° larger than that in the other bromide cluster units centered by the smaller main-group elements. Nonetheless, the Zr atoms in $CsZr_6Br_{14}Mn$ are still more than 10° off the square plane of Br^i and Br^{i-a}. The relatively short Br-Br distance, e.g., 3.743(1) Å, is more evidence for the matrix effect presented in $CsZr_6Br_{14}Mn$.

As shown in Figure 59, the Cs cation occupies a 12-coordinate position within the Br layer defined by Br1 and Br5, and is surrounded by six cluster units. The Cs position has a C_{2h} point symmetry. The 2-fold axis is collinear with two Br5, and the mirror, normal to the 2-fold axis, contains two Br4. The average Cs-Br distance is 3.809 Å, slightly shorter than the summation of the corresponding crystal radii of Cs(XII) and Br(VI), 3.84 Å.

As indicated in Table 38, the compound with Li in the lattice has a fairly large cell volume, even greater than that of $RbZr_6Br_{14}B$, indicating that lithium atoms occupy the alternate six-coordinate site between the Br layers as in $LiZr_6Cl_{14}Mn$ (Figure 60).[78] Assuming r_{Br} = 1.89 Å, which is half of the average Br-Br distance in $CsZr_6Br_{14}Mn$ [$\bar{d}$(Br-Br) in $MZr_6Br_{14}B$ might be shorter, but should be very close to this value], the radius of an octahedral site in the closest packed anion lattice is 0.79 Å. The incorporation of the Li^+ [r(CN=6) = 0.90 Å] into such an octahedral site causes the lattice expansion. As the R_+/R_- increases, the six-coordinate position becomes less favored, and the larger cations prefer to

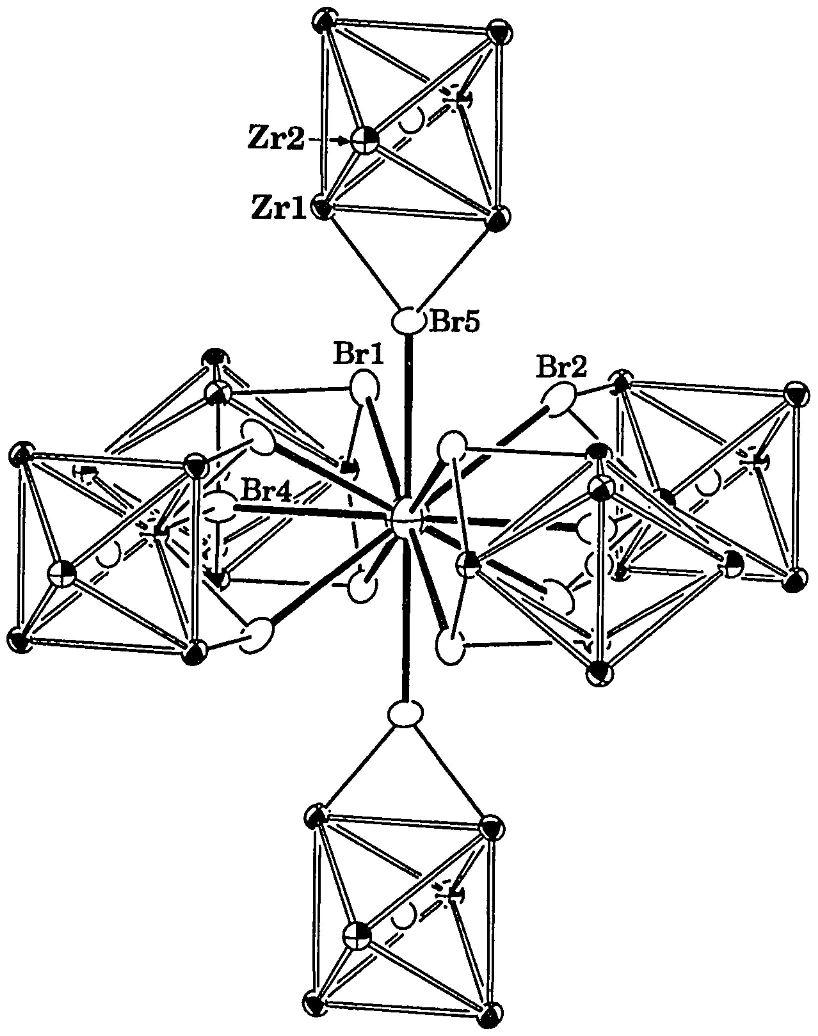

Figure 59. The 12-bonded Cs site in $CsZr_6Br_{14}Mn$, which is surrounded by six cluster units. It is in the Br layer defined by Br1 and Br5, and has C_{2h} point symmetry. The 2-fold axis is collinear with two Br5, and the mirror, normal to the 2-fold axis, contains two Br4 (90% probability)

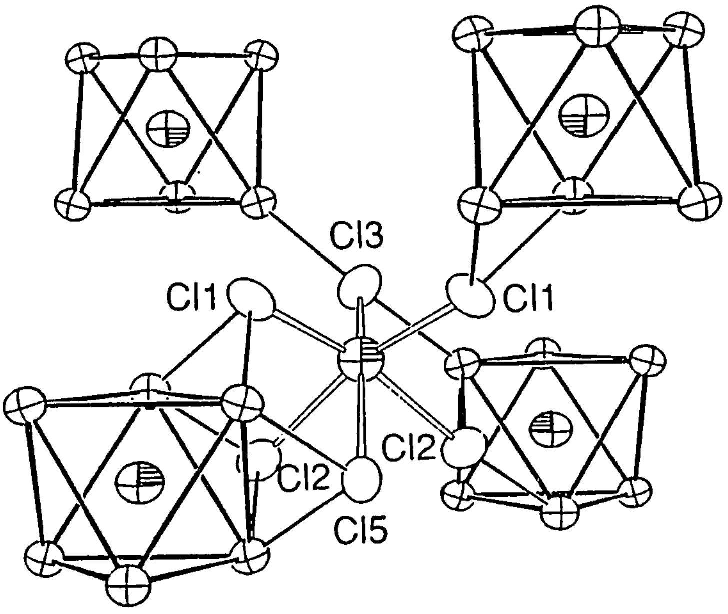

Figure 60. The chlorine environment around lithium in $LiZr_6Cl_{14}Mn$ (90%).[78] All other chlorine atoms have been left out

occupy the twelve-coordinate site in the Br layer as indicated in Figure 59. The cell volumes of $NaZr_6Br_{14}B$, $KZr_6Br_{14}B$, and $RbZr_6Br_{14}B$ are all smaller than that of $LiZr_6Br_{14}B$, indicating that they are indeed the larger, twelve-coordinate cation sites. Therefore, it is reasonable to conclude that cations with radii larger than that of Li^+ occupy the twelve-coordinate site in the lattice of $Mzr_6Br_{14}B$. In other words, the cation preference in $Mzr_6Br_{14}B$ follow the same trend as found in $Mzr_6Cl_{14}B$.[78]

6-12 Type

The first 6-12 zirconium bromide cluster phase, namely $Zr_6Br_{12}H$[44] ($Zr_6I_{12}C$ type), was serendipitously prepared by the thermal decomposition of ZrBr in a H_2 stream. After the presence of interstitial elements in the group III and IV transition metal halide cluster phases was confirmed, another compound, $Zr_6Br_{12}B$ [35] was synthesized by purposely adding an appropriate amount of amorphous boron into the reaction. This investigation provided one more 6-12 bromide cluster phases, i.e., $Zr_6Br_{12}Be$. In the previous studies, however, no single crystal structure studies were carried out on any of the zirconium bromide cluster compounds. In other words, there was no knowledge about the metal-metal and metal-interstitial bonding details in the zirconium bromide system, or about how the bromine lattice affect the Zr-Zr and Zr-Z distances. Therefore, single crystal structure refinements were performed on $Zr_6Br_{12}B$ and $Zr_6Br_{12}Be$ to gain the insight about the important bonding features in the zirconium bromide cluster compounds.

$ZR_6BR_{12}B$ AND $ZR_6BR_{12}BE$

Synthesis: Both $Zr_6Br_{12}Be$ (14e) and $Zr_6Br_{12}B$ (15e) could be prepared with high yields from stoichiometric reactions carried out at 850°C for about two weeks. A stoichiometric reaction ($Zr_6Br_{12}C$) and one loaded with more reducing condition, i.e., $Zr_6Br_{10}C$, both yielded $Zr_6Br_{14}C$ (14e), instead. Well faceted, gemlike, black crystals of $Zr_6Br_{12}B$ were obtained in the reaction loaded as Zr_6Br_7B and carried out at 850°C for about two weeks. Nicely formed hexagonal cross section rod-shaped crystals of $Zr_6Br_{12}Be$ were found in the reaction loaded as $Na_8Zr_6Br_{20}Be$ and run at 850°C for four weeks. The major product was $(Na_{>4}Br)_2Zr_6Br_{18}Be$ with distorted $(K_4Br)_2Zr_6Br_{18}B$ structure (6-18 type).

Single Crystal Structure Studies: The quality or singularity of the crystals of $Zr_6Br_{12}B$ and $Zr_6Br_{12}Be$ was checked on Weissenberg camera prior to the data collections. A RIGAKU AFC6R diffractometer was utilized to collect data on the crystal of $Zr_6Br_{12}B$. The 25 reflections located during SEARCH could be indexed in a rhombohedral cell which was transformed to a standard hexagonal setting by DELAUNAY. A hemisphere of data was collected without omitting the extinct reflections ($-h+k+l\neq3n$) due to the R-centering. As indicated in the data set, $Zr_6Br_{12}B$ did have a rhombohedral lattice symmetry, for none of the $-h+k+l\neq3n$ type of reflections was observed.

Space group $R\bar{3}$ was chosen according to the Laue symmetry, the statistical analysis as well as extinction conditions. Data preparation involved the Lorentz and polarization correction followed by an empirical absorption correction using three averaged ψ-scan measurements. After the weak reflections ($I<3\sigma$) were rejected, data were averaged in the corresponding point group $\bar{3}$ with R_{ave}=6.1%. Other important data collection and structure refinement parameters are listed in Table 42. The positional parameters obtained in $Zr_6I_{12}C$ were used in the initial refinement. The isotropic refinements were carried out on all the atoms except for interstitial boron and converged with R=5.2% and R_w=4.6%. The anisotropic refinement went smoothly and converged at R=3.0% and R_w=2.7%. The secondary extinction coefficient and isotropic thermal displacement parameters of boron were refined at the final stage. The final difference Fourier map was basically flat with the largest positive peak as 1.5 e/Å^3 at (0, 0, 1/2), a special position with $\bar{3}$ symmetry. The refined positional and anisotropic thermal parameters are compiled in Table 43.

The single crystal x-ray diffraction study of $Zr_6Br_{12}Be$ was carried out on an ENRAF NONIUS CAD4 diffractometer. Data were collected on two octants (±h,k,l). The data collection on the first octant went quite smoothly; however, a lot of reflections collected on the second octant were off center, indicating that the crystal, somehow, moved during the data collection. The situation did not get better after the crystal was recentered. Because of this, the ψ-scan reflections could not measured very well. Thus, the structure was refined with the reflections collected only in the first octant and without the empirical absorption correction applied. It turned out that the refinement results were rather satisfactory in terms of the shapes of the anisotropic thermal ellipsoids

Table 42. Crystal data for $Zr_6Br_{12}B$ and $Zr_6Br_{12}Be$

	$Zr_6Br_{12}B$	$Zr_6Br_{12}Be$
space group, Z	$R\bar{3}$(h) (no. 148), 3	$R\bar{3}$(h) (no. 148), 3
cell parameters[a]		
a (Å)	13.6348(6)	13.7094(6)
c	9.3057(6)	9.3242(5)
V (Å^3)	1498.2(2)	1517.7(2)
crystal dimens.(mm)	0.05 x 0.13 x 0.16	0.13 x 0.16 x 0.28
octants measured	±h, k, ±l	-h, k, l
2θ (max.), deg.	50	50
reflections		
measured	2483	456
observed (I/σ(I)>3.0)	604	369
indep.	403	345
abs.coeff. (Mo Kα, cm^{-1})	267.4	263.9
transm. coeff. range	0.32-1.00	not applied
no. variables	30	30
R_{ave}, % (obs.)	6.1	4.2
sec. extinct. coeff.	4.4(5) x 10^{-8}	1.9(2) x 10^{-7}
R, %	3.0	3.9
R_w, %	2.7	4.6

[a] Guinier data

Table 43. Positional and thermal parameters for $Zr_6Br_{12}B$ and $Zr_6Br_{12}Be$

Atom	Psn.	x	y	z	B_{eq}(Å^2)
<u>$Zr_6Br_{12}B$</u>					
Zr	18(f)	0.15313(7)	0.04289(7)	0.1437(1)	0.66(3)
Br1	18(f)	0.35459(8)	0.10257(8)	0.3316(1)	1.21(4)
Br2	18(f)	0.12813(7)	0.17882(7)	0.3279(1)	1.17(4)
B	3(a)	0	0	0	1.2(5)
<u>$Zr_6Br_{12}Be$</u>					
Zr	18(f)	0.1561(1)	0.04401(9)	0.1479(1)	0.52(5)
Br1	18(f)	0.3557(1)	0.1034(1)	0.1479(1)	1.02(6)
Br2	18(f)	0.1282(1)	0.1786(1)	0.3287(2)	1.02(6)
Be	3(a)	0	0	0	1.1(7)

[a] U x 10^3

U_{11}[a]	U_{22}	U_{33}	U_{12}	U_{13}	U_{23}
8.3(5)	10.0(4)	7.0(5)	4.8(4)	-0.9(5)	-0.3(5)
10.9(4)	15.6(5)	15.6(9)	3.6(4)	-2.5(5)	3.4(5)
15.1(5)	18.2(6)	12.9(8)	9.6(4)	-5.0(4)	-7.0(5)
15(6)					
5.5(7)	7.2(6)	7.4(8)	3.5(5)	-0.9(5)	-0.7(5)
8.8(7)	13.0(7)	13(1)	2.7(5)	-2.1(5)	2.4(5)
13.7(7)	15.8(8)	12(1)	9.1(6)	-3.6(5)	-5.0(5)
14(9)					

of the atoms as well as the standard deviations of the positional parameters. Therefore, no further data collection was attempted. The data collection parameters and the structure refinement results are compiled in Table 42 and their positional and anisotropic thermal parameters are listed in Table 43, together with those of $Zr_6Br_{12}B$.

Structure Descriptions and Comparisons: According to the cell dimensions, lattice symmetry, and atom positions, $Zr_6Br_{12}Be$ and $Zr_6Br_{12}B$ are isostructural with $Zr_6I_{12}C$. Figure 61 gives the $[1\bar{1}0]$ projection. As shown, the building blocks are $(Zr_6Z)Br_{12}$ octahedral cluster units, and they form two-dimensional slabs normal to the $\bar{3}$ axis. These cluster layers stack in the cubic-close-packed fashion as ...ABCABC..., which yields a rhombohedral lattice. The edge-bridging Br atoms around the waist of the octahedra also serve as more distant terminal Br atoms in the neighboring cluster units. Owing to this kind of cluster connectivity, the cluster layers are pulled together more, resulting in a much squashed rhombohedral cell (~107° rhombohedral angle) and a three dimensional network. Figure 62 gives the projection on the ab plane, which shows the cluster connectivities from a different direction. The three-bonded Br atoms ($Br^{i\text{-}a}$ and $Br^{a\text{-}i}$) can be clearly seen in the picture. According to the cluster connectivities and the functions of the Br atoms, the formula of the 6-12 phase can be explicitly expressed as $[(Zr_6Z)Br^{i}_{6}]Br^{i\text{-}a}_{6/2}Br^{a\text{-}i}_{6/2}$.

In fact, the lattice of $Zr_6Br_{12}B$ and $Zr_6Br_{12}Be$ can be alternatively described as cubic-close-packed Br^- anion layers with half of the octahedral sites between

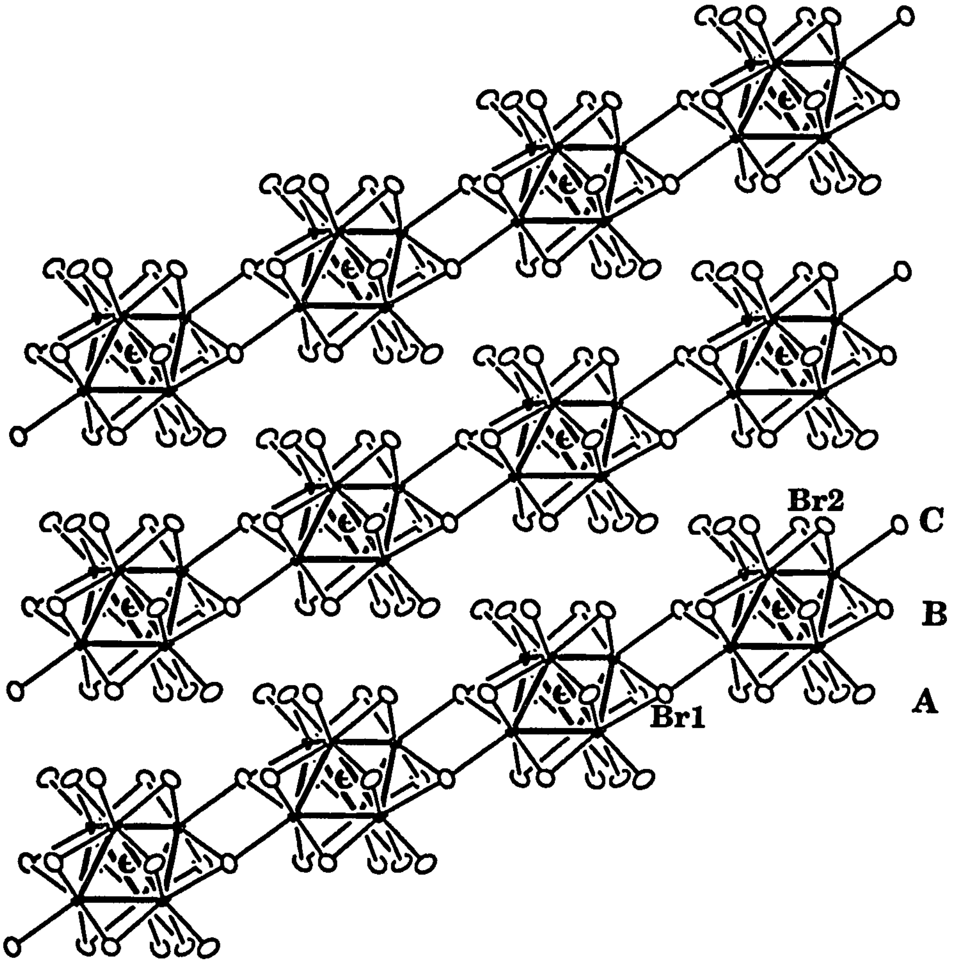

Figure 61. A [1$\bar{1}$0] projection of the rhombohedral structure of $Zr_6Br_{12}B$, showing that the Br atoms around the waist of a Zr_6 octahedron serve as the terminal Br atoms for the neighboring clusters (90% probability)

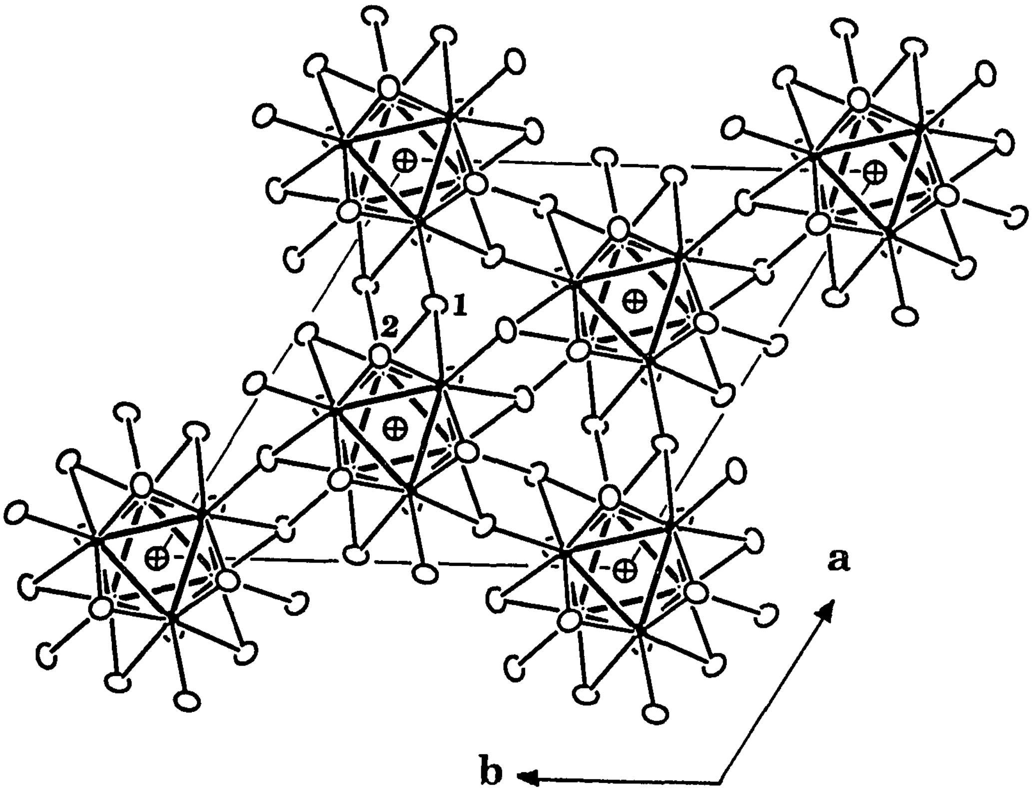

Figure 62. A [001] projection of the rhombohedral structure of $Zr_6Br_{12}B$ in the standard hexagonal setting. It shows the cluster connectivities from another direction (90% probability)

the anion layers occupied by the Zr atoms. These Zr atoms congregate to form a trigonal antiprismatic cluster around the interstitial atom that substitutes in one of the Br sites. In both $Zr_6Br_{12}B$ (15e) and $Zr_6Br_{12}Be$ (14e), the interlayer Zr-Zr distances, 3.261(1) Å and 3.356(2) Å, are longer than the intralayer ones which are 3.231(1) Å and 3.313(2) Å, respectively (Table 44). In other words, the Zr_6 trigonal antiprisms are elongated along the $\bar{3}$ axis (Figure 63), which is similar to the Zr_6 in $Cs_2ZrI_6{\cdot}Zr_6I_{12}C$ (16e),[79] but opposite to those in $Zr_6I_{12}C$ (16e).[15] The distortion of the Zr_6 antiprisms could be a net effect of the electronic configuration of cluster units, the matrix effect caused by different halogen anions as well as different interstitial elements, and the bonding environment around the clusters.

The average Zr-Zr and Zr-Z distances are 3.246 Å and 2.2956(9) Å in $Zr_6Br_{12}B$, and 3.335 Å and 2.358(1) Å in $Zr_6Br_{12}Be$. They are all longer than the corresponding ones in $Zr_6I_{12}C$, 3.195 Å and 2.259(1) Å, respectively. It appears that the size of the interstitial atoms has a better control over the Zr-Zr and Zr-Z distances than the halide ligands. However, when it comes to the situation where the electron counts for the Zr_6Z core are more than the optimal number, i.e., 14, the size of the halide ligands or the matrix effect of the anion lattice plays a very important role in stabilizing the cluster phases. The evidences are that $Zr_6Cl_{12}B$ (15e) could not be synthesized, while a high yield of $Zr_6Br_{12}B$ could be prepared from a stoichiometric reaction, indicating that the 15e phase is stabilized by the larger matrix effect in the bromide lattice. Similarly, the

Table 44. Important bond distances (Å) and angles (°) in $Zr_6Br_{12}B$ and $Zr_6Br_{12}Be$

		$Zr_6Br_{12}B$	$Zr_6Br_{12}Be$
d(Zr-Zr)			
intra-layer	x2[a]	3.231(1)	3.313(2)
inter-layer	x2	3.261(2)	3.356(2)
d(Zr-Z)	x1	2.2956(9)	2.358(1)
d(Zr-Br^i)			
Zr-Br2	x1	2.658(1)	2.664(2)
		2.668(1)	2.665(2)
d(Zr-Br^{i-a})			
Zr-Br1	x1	2.730(1)	2.730(2)
		2.759(1)	2.763(2)
d(Zr-Br^{a-i})			
Zr-Br1	x1	3.004(1)	2.976(2)
d(Br-Br)[b]			
Br1-Br1	x1	3.718(2)	3.733(3)
Br1-Br2	x1	3.718(1)	3.743(2)
	x2	3.746(1)	3.783(2)
	x1	3.771(2)	3.790(2)
	x1	3.779(2)	
	x1	3.803(1)	
Br2-Br2	x2	3.770(1)	3.788(2)
	x1	3.800(2)	
Zr-Zr-Zr	x1	60.00	60.00
	x2	90.00	90.00
	x2	60.30(2)	60.43(2)
	x1	59.39(4)	59.14(5)
Br1-Zr-Br2	x1	163.22(6)	165.58(7)
	x1	164.34(5)	166.55(7)

[a] Number of times the distances and angles occur per atom

[b] d(Br-Br) ≤ 3.803 Å

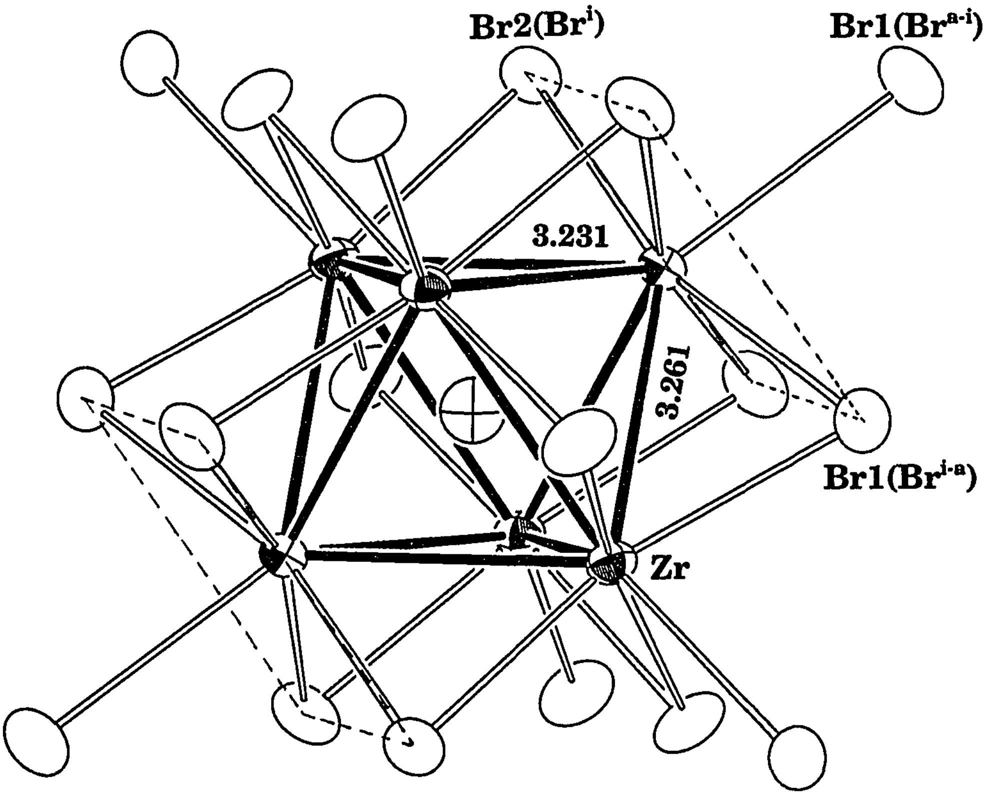

Figure 63. The elongated Zr_6 cluster unit in $Zr_6Br_{12}B$, emphasizing the withdrawal of the Zr atom from the square face formed by the edge-bridging Br^i atoms (90% probability)

reactions loaded with either $Zr_6Br_{12}C$ or more reduced stoichiometry, $Zr_6Br_{10}C$, always produced $Zr_6Br_{14}C$ (14e), instead of the 16e target phase $Zr_6Br_{12}C$. The 16e 6-12 carbide, on the other hand, could be easily made in the zirconium iodide system. Since the interstitial elements are different in $Zr_6I_{12}C$, $Zr_6Br_{12}B$, and $Zr_6Br_{12}Be$, the direct comparison of the matrix effect in the bromide and iodide lattice is less meaningful. The results in the syntheses, however, clearly demonstrate that the extent of matrix effect increases in the order of Cl-Br-I.

For $Zr_6Br_{12}B$ and $Zr_6Br_{12}Be$, the matrix effect caused by different interstitial atoms can be very well compared by the trans Br^i-Zr-Br^i angles. The average value is 163.8° in the boride and 166.1° in the beryllide, indicating that the Zr atoms in the boride are pulled in from the Br^i rectangular plane more than in the beryllide, or the 15e boride has a larger extent of matrix effect. Because of this, the Zr-$Br^{a\text{-}i}$ distance in $Zr_6Br_{12}B$, 3.004(1) Å, is longer than that in $Zr_6Br_{12}Be$, 2.976(2)Å (12.5σ). The average Zr-Br^i and Zr-$Br^{i\text{-}a}$ distances in $Zr_6Br_{12}B$ (2.663 Å and 2.745 Å), on the other hand, are very comparable with those in $Zr_6Br_{12}Be$, which are 2.665 Å and 2.747 Å, respectively. The slightly shorter Br^i-$Br^{a\text{-}i}$ and $Br^{i\text{-}a}$-$Br^{a\text{-}i}$ distances, 3.718(2) Å, in $Zr_6Br_{12}B$ (3.743(2) Å and 3.733(3) Å in the beryllide) are more supportive evidence for the larger matrix effect in the boride.

General Observations

Electron counts and matrix effects

In the zirconium halide systems, the (Zr_6Z) cluster cores in the cluster phases centered by main-group elements tend to have optimal 14e in their bonding orbitals, and 18e in those stabilized by a transition-metal element. The violations of the electron-count rule are very rare in the zirconium chloride system. In the bromide system however, many more cluster phases with higher than optimal number of electrons have been prepared and characterized, e.g., $(K_4Br)_2Zr_6Br_{18}Mn$ (19e), $(K_4Br)_2Zr_6Br_{18}B$ (15e), $Cs_{3.4}Zr_6Br_{15}B$ (15.4e), $Cs_3Zr_6Br_{15}C$ (16e), $Rb_5Zr_6Br_{15}Be$ (16e), and Zr_6Br_{12} (15e), and so on. In this sense, the bromide systems resemble more to the iodide systems which also have very flexible electron counts for (Zr_6Z). This trend is consistent with the extent of the matrix effect discussed in the previous sections.

According to the molecular orbital diagrams obtained from extended Hückel calculations, the 14e cluster unit centered by main-group element has a_{2u} as the lowest unoccupied orbital or LUMO. It has a slightly bonding character between the metal atoms and is antibonding between the metal and the edge-bridging X^i. In order to have appropriate M-M bonding in the halogen anion network, the Zr atoms usually deviate from the rectangular plane of X^i to get close to each other, which pulls the halide ligands towards each other and into increasingly repulsive interaction. Because of this, the M-M bonding is compromised and forced to be less than optimal, the so called matrix effect. It can be measured or compared by the value of trans X^i-Zr-X^i angles. The bigger the halogen anions, the more withdrawal of the Zr atoms from the X^i_4 plane and the smaller the trans X^i-Zr-X^i angles or the larger the matrix effect. As one can see, the larger matrix effect helps to reduce the antibonding character of a_{2u} orbital, and this, in turn, helps to stabilize 15e or 16e cluster phases. Some meaningful trans X^i-Zr-X^i angles are 156-163° in $(Zr_6I_{12}C)I_2$, 164-166° in $(Zr_6Br_{12}C)Br_n$, and 167-171° in $(Zr_6Cl_{12}Z)Cl_n$, indicating that the matrix effect increases in the order Cl-Br-I. This also explains why the cluster phases with higher electron counts are more often seen in the bromide and iodide than in the chloride system.

Structures

This investigation provided more than thirty new bromide cluster phases in ten distinct structure types, plus several structural variations thereon. The cluster network Zr/Br ratio ranges from 6/12 to 6/18, the same as found in the chloride system. These results indicate that the bromide system has a structural chemistry as fruitful as that of the chloride system, and much richer than that of the iodide system which has only two structure types, i.e., $Zr_6I_{12}C$ and Nb_6Cl_{14}-type. When the chloride and bromide systems are compared, several noticeable different structural features are observed.

First of all, the bromide phases are generally very sensitive to the interstitial elements. For instance, $Cs_3Zr_6Cl_{16}C$ structure type could also form with B and Be as interstitials in the chloride system; the same structure type, on the other hand, could only be realized with Be in the zirconium bromide system. The replacement of Be with either B or C provided two completely different structure types. i.e., $Cs_3Zr_6Br_{15}C$ and $(Cs_4Br)Zr_6Br_{16}B$. Another example is $K_4Zr_6Br_{18}C$ which is structurally related to $Rb_4Zr_6Cl_{18}C$ and $Rb_5Zr_6Cl_{18}B$. In these two 6-18 chloride phases, even though the interstitials as well as the number of countercations are different, their structures are fairly closely related in terms of the cluster arrangement and cation environment. In the bromide system, however, the substitution of C by B yields a totally different 6-18 phase, namely, $(K_4Br)_2Zr_6Br_{18}B$. Not only the arrangement of the cluster units but also the environment as well as the distribution of the countercations are all different from those in $K_4Zr_6Br_{18}C$.

The zirconium bromide cluster phases are also very sensitive to the countercations used in the reactions, for certain structure types can only form with certain kinds and numbers of countercations. One of the most noticeable example is the synthesis of $Cs_{3.4}Zr_6Br_{15}B$ which is isostructural with $Cs_3Zr_6Br_{15}C$. Firstly, this structure type only forms with Cs as$^+$ countercations. Secondly, the boride phase could only be made with slightly lower (~3.0) Cs content. A higher Cs content yielded the novel $(Cs_4Br)Zr_6Br_{16}B$, and a lower Cs content (~2.0) gave a high yield of unknown phase B. The same is true for $Rb_3Zr_6Br_{15}Be$, as a higher cation content yielded $Rb_5Zr_6Br_{15}Be$, and a lower cation content produced a unknown cluster phase (Phase C). Besides, certain structure types can be stabilized with certain size of countercations. As mentioned early

$Cs_{3.4}Zr_6Br_{15}B$ and $Cs_3Zr_6Br_{15}C$ only form with Cs. The same is true for $(Cs_4Br)Zr_6Br_{16}B$. The framework of $Rb_3Zr_6Br_{15}Be$ can only be stabilized by either Rb^+ or K^+ cations, not Cs^+ or Na^+.

The formation of polycations $[M_4Br]^{3+}$, where M=Na, K, Rb, and Cs, is another distinguishing structure feature observed only in the bromide system. Prior to the discovery of $(M_4Br)_2Zr_6Br_{18}Z$ (M=Na, K, Rb; Z=H, Be, B, Mn) and $(Cs_4Br)Zr_6Br_{16}B$, the tetrahedrally coordinated halogen anions had only been observed in the cavity of zeolites, i.e., sodalite. In terms of the size and the charge of countercations, polycations $[M_4Br]^{3+}$, so far, are the best in stabilizing cluster anion frameworks. Their large sizes and high charges greatly help to reduce the repulsive forces among negatively charged cluster units by pushing them much farther than any kind of single countercations can do, while keeping a very strong interaction with the anion networks or cluster units.

FUTURE WORK

Over thirty new interstitially stabilized zirconium bromide cluster phases have been discovered in the course of this work, which marks the beginning of the study of zirconium bromide systems. So far, the synthetic effort in this system has been involved in a relatively limited number of interstitial elements, namely, light main-group elements (H, Be, B, C), and mainly alkali-metal elements as countercations. Further research along these lines is bound to result in even more new and interesting compounds. As listed in Table 45, several unknown phases with high yields have been repeatedly observed. The study of these new phases is only a matter of luck in getting good single crystals. A longer reaction period and/or some vapor transporting agents may help the crystal growth.

In addition, the following are suggested as potentially fruitful routes for further investigation. First of all, Mn and Fe are the only transition-metal elements tried in this study. Therefore, synthetic studies need to be conducted systematically to incorporate more transition-metal elements (3d, 4d, and 5d) into the zirconium bromide clusters, which may result in some structure modifications or even new structure types. Only a few reactions have been tried with Al or Si as interstitials, but without success. More reactions with heavy main-group elements are needed to be carried out either at different temperatures, or with a different source instead of the elemental form. Countercations other than alkali-metal elements are also worth a try.

Table 45. The unknown phases observed in the zirconium bromide System

Loaded Stoichiometry	Reaction conditions	Phase label	yield
$Na_4Zr_6Br_{15}C$	840°C/4 weeks	Phase A	~ 30%
$Na_8Zr_6Br_{20}C$	850°C/4 weeks		~ 50%
$Na_6Zr_6Br_{10}C$	850°C/3 weeks		> 60%
$Ca_3Zr_6Br_{18}C$	1000°C/4 weeks	phase B	> 90%
$Ba_3Zr_6Br_{18}C$	1000°C/4 weeks		> 90%
$NaZr_6Br_9B$	850°C/3 weeks	Phase C	~ 50%
$Na_4Zr_6Br_{15}B$	830°C/5 weeks		~ 90%
$Rb_2Zr_6Br_{15}Be$	850°C/4 weeks	Phase D	> 95%
$Cs_2Zr_6Br_{15}Be$	850°C/6 weeks	Phase E	> 90%

As shown in Table 45, new phases with Ba^{2+} or Ca^{2+} as countercations have been observed. Other alkaline-earth and rare-earth metal elements are the potential candidates in making new cluster frameworks as well as new compounds.

Another untouched area in the zirconium bromide system are the phases containing mixed countercations. Based on the results obtained in the zirconium chloride system, the mixing of countercations may lead to the formation of new structure networks or modifications. Finally, the primary studies in the Zr-Cl-I system have provided numerous interesting phases with known, modified or even new structure types. Further investigations in this system should be at least as fruitful as in the pure halide systems, for the mixing of the halogen anions provides one a considerable power to modify or to control the anion networks.

Properties: In the course of this work, the major means used in the property study has been magnetic susceptibility measurements, which has provided some insight about the orders of bonding orbitals and the number of electrons in (Zr_6Z) cluster units, especially in those of 15e and 16e cluster phases. Optical studies in the tungsten, molybdenum, niobium as well as zirconium cluster halide systems [79-85] have revealed that some of these cluster phases exhibit very interesting optical properties, e.g., luminescence, redox photochemistry as well as unusual emissive behavior, and so on. Similar studies in the zirconium bromide system will provide some at least equally interesting and useful information about the optical properties of zirconium bromide cluster phases. The same is true for other cluster halide systems.

REFERENCES

(1) Schäfer, H.; Schnering, H.-G. *Angew. Chem.* **1964**, *76*, 833.

(2) Wells, A. F. *Structural Inorg. Chem.*, 5th ed., Clarendon Press, Oxford, **1984**, 432-437.

(3) Simon, A.; von Schnering, H.-G.; Schäfer, H. *Z. Anorg. Allg. Chem.* **1968**, *361*, 235.

(4) Bauer, D.; Schnering, H.-G. *Z. Anorg. Allg. Chem.* **1968**, *361*, 259.

(5) Schäfer, H.; Schnering, H.-G.; Niehues, K.-J.; Nieder-Vahrenholz, H. G. *J. Less-Common Met.* **1965**, *9*, 95.

(6) Simon, A.; von Schnering, H.-G.; Wöhrle, H.; Schäfer, H. *Z. Anorg. Allg. Chem.* **1965**, *339*, 155.

(7) Corbett, J. D. *Pure and Applied Chem.* **1984**, *56*, 1527.

(8) Gronwold, F.; Kjekshus, A.; Raaum, F. *Acta Crystallogr.* **1961**, *14*, 930.

(9) Bateman, L. R.; Blorent, J. F.; Dahl, L. F. *J. Am. Chem. Soc.* **1966**, *88*, 1082.

(10) Simon, A.; von Schnering, H.-G.; Schäfer, H. *Z. Anorg. Allg. Chem.* **1967**, *355*, 295.

(11) Meyer, H.-J.; Corbett, J. D. *Inorg. Chem.* **1991**, *30*, 963.

(12) Chevrel, R.; Sergent, M.; Prigent, J. *J. Solid State Chem.* **1971**, *3*, 515.

(13) Perrin, A.; Leduc, L.; Sergent, M. *Eur. J. Solid State Inorg. Chem.* **1991**, *28*, 919.

(14) Gabriel, J.-C.; Boubekeur, K.; Batail, P. *Inorg. Chem.* **1993**, *32*, 2894.

(15) Ziebarth, R. P.; Corbett. J. D. *J. Am. Chem. Soc.* **1985**, *107*, 4571.

(16) Ziebarth, R. P.; Corbett, J. D. *J. Am. Chem. Soc.* **1987**, *109*, 4844.

(17) Zhang, J.; Corbett, J. D. *Inorg. Chem.* **1991**, *30*, 431.

(18) Corbett, J. D. *Modern Perspectives in Inorganic Crystal Chemistry*, E.Parthé, ed. (NATO ASI Series C), Kluwer Academic Publishers, Dordrecht, The Netherlands, **1992**, 27-56.

(19) Smith, J. D.; Corbett. J. D. *J. Am. Chem. Soc.* **1986,** *108,* 1927.

(20) Rosenthal, G.; Corbett, J. D. *Inorg. Chem.* **1988,** *27*, 53.

(21) Rogel, F.; Zhang, J.; Payne, M. W.; Corbett, J. D. *Adv. Chem. Ser.* **1990,** *226*, 369.

(22) Hughbanks, T.; Corbett, J. D. *Inorg. Chem.* **1988,** *27*, 2022.

(23) Hughbanks, T.; Corbett. J. D. *Inorg. Chem.* **1989,** *28*, 631.

(24) Payne,M. W.; Corbett, J. D. *Inorg.Chem.* **1990,** *29,* 2246.

(25) Payne, M. W.; Dorhout, P. K.; Corbett, J. D. *Inorg. Chem.* **1991,** *30,* 1467.

(26) Dorhout, P. K.; Payne, M. W.; Corbett, J. D. *Inorg. Chem.* **1991,** *30,* 4960.

(27) Payne, M. W.; Ebihara, M.; Corbett, J. D. *Angew. Chem.* **1991,** *30,* 856.

(28) Ebihara, M.; Martin, J. D.; Corbett, J. D. submitted to *Inorg. Chem.* **1993.**

(29) Smith, J. D.; Corbett, J. D. *J. Am. Chem. Soc.* **1985,** *107,* 5704.

(30) Ziebarth, R. P.; Corbett, J. D. *Acc. Chem. Res.* **1989,** *22,* 256.

(31) Ziebarth, R. P.; Corbett, J. D. *J. Am. Chem. Soc.* **1989,** *111,* 3272.

(32) Hughbanks, T.; Rosenthal, G.; Corbett, J. D. *J. Am. Chem. Soc.* **1986,** *108,* 8289.

(33) Hughbanks, T.; Rosenthal G.; Corbett. J. D. *J. Am. Chem. Soc.* **1988,** *110,* 1511.

(34) Rogel, F.; Corbett, J. D. *J. Am. Chem. Soc.* **1990,** *112,* 8198.

(35) Ziebarth, R. P.; Corbett, J. D. *J. Solid State Chem.* **1989,** *80,* 56.

(36) Chu, P. J.; Ziebarth, R. P.; Corbett, J. D.; Gerstein, B. C. *J. Am. Chem. Soc.* **1988,** *110,* 5324.

(37) Qi, R.-Y.; Corbett, J. D., Iowa State University, unpublished research, **1992**.

(38) Guthrie, D. H.; Corbett, J. D. *Inorg. Chem.* **1982**, *21*, 3290.

(39) Imoto, H.; Simon, A, Max-Planck-Institut für Festkörperforschung, Stuttgart, Germany, unpublished research, **1980**.

(40) Ziebarth, R. P.; Corbett, J. D. *J. Am. Chem. Soc.* **1988**, *110*, 1132.

(41) Zhang, J.; Corbett, J.D., Iowa State University, unpublished research, **1990**.

(42) Ziebarth, R. P.; Corbett, J. D. *Inorg. Chem.* **1989**, *28*, 626.

(43) Zhang, J.; Corbett, J. D. *J. Less-Common Met.* **1989**, *156*, 49.

(44) Imoto, H.; Corbett, J. D.; Cisar, A. *Inorg. Chem.* **1981**, *20*, 145.

(45) Mattausch, H.; Hendricks, J. B.; Eger, R.; Corbett, J. D.; Simon, A. *Inorg. Chem.* **1980**, *19*, 2128.

(46) Poeppelmeier, K. R.; Corbett, J. D. *Inorg.Chem.* **1977**, *16*, 294.

(47) Araujo, R.; Corbett, J. D. *Inorg. Chem.* **1981**, *20*, 3082.

(48) Mattausch, H.; Simon, A.; Holzer, N.; Eger, R. *Z. Anorg. Allg. Chem.* **1980**, *466*, 7.

(49) Corbett, J. D. and coworkers, Iowa State University, unpublished research.

(50) Miller, A. E.; Daane, A. H.; Haberman, C. E.; Beaudry, B. J. *Rev. Sci. Inst.* **1963**, *34*, 644.

(51) Schäfer, H. *Chemical Transport Reactions*, Academic Press Inc., New York, **1964**, Chapter 2.

(52) Holland L. *The properties of Glass Surfaces*, Chapman and Hall, London, **1966**, Chapter 4.

(53) Clark, C. M.; Smith, D. k.; Johnson, G. J. A Fortran IV Program for Calculating X-Ray Powder Diffraction Patterns - Version 6, Department of Geosciences, Pennsylvania State University: University Park, PA, **1973**.

(54) Imoto, H., Ames Laboratory, Iowa State University, unpublished research, **1978**.

(55) Takusagawa, F., Ames Laboratory, Iowa State University, unpublished research, **1981**.

(56) Werner, P. E. TREOR-V5, Department of Strusture Chem., Arrhenius Laboratory, University of Stockholm: Stockholm, Sweden, **1984**.

(57) Sheldrick, G. M., SHELXS-86, Programs for Structure Determination, Universit Göttingen, Germany, **1986**.

(58) TEXSAN: Single Crystal Structure Analysis Software, Version 5.0, Molecular Structure Corporation, The Woodlands, TX, **1989**.

(59) International Tables for X-Ray Crystallography, Kynoch Press: Birmingham, England, **1968**, Vol. III.

(60) Johnson, C. K., ORTEP, A Fortran Thermal-Ellipsoid Plot Program for Crystal Structure Illustrations, Oak Ridge National Laboratory, Oak Ridge, TN, **1970**.

(61) Coppens, P.; Hamilton, W. C. *Acta Crystallogr.* **1970,** *A26*, 71.

(62) Köckerling, M., Iowa State University, unpublished research, **1993**.

(63) Zhang, J.; Ziebarth, R. P.; Corbett, J. D. *Inorg. Chem.* **1992**, *31*, 614.

(64) Ihmaine, S.; Perrin, C.; Sergent, M. *Z. Acta Crystallogr.* **1989**, *C45*, 705.

(65) Von Dreele, R. B.; Jorgensen, J. D.; Windsor, C. B. *J. Appl. Crystallogr.* **1982**, *15*, 581.

(66) Karcher, B. A., Ph.D. Dissertation, Iowa State University, Ames, IA, 1981.

(67) Newnham, R. E. in "Structure-Property Relations," R. Roy, ed., Springer-Verlag: New York, **1975**, 134.

(68) Zhang, J.; Corbett, J. D. *Z. Anorg. Allg. Chem.* **1991**, *598/599*, 363.

(69) Ziebarth, R. P., Ph.D. Dissertation, Iowa State University, Ames, IA, **1987**.

(70) Bronger, W.; Missen, H.-J. *J. Less-Common Met.* **1982**, *83*, 29.

(71) Qi, R.-Y.; Corbett, J. D. manuscript in preparation.

(72) Chapuis, G. C. *Modern Perspectives in Inorganic Crystal Chemistry*, E.Parthé, ed. (NATO ASI Series C), Kluwer Academic Publishers, Dordrecht, The Netherlands, **1992**, 1-16.

(73) Converse, J. G.; McCarley, R. E. *Inorg. Chem.* **1970**, *9*, 1361.

(74) Van Vleck, J. H. *The Theory of Electric and Magnetic Susceptibilities*, Oxford University Press, Oxford, England, **1932**, 277.

(75) West, A. R. *Solid State Chemistry and Its Applications*, John Wiley & Sons, New York, **1984**, 31-32.

(76) Shannon, R. P. *Acta Crystallogr. Sec. A* **1976**, *A32, 751.*

(77) Martin, J. D.; Corbett, J. D., Iowa State University, unpublished research, **1993**.

(78) Zhang, J.; Corbett, J. D. submitted to *Inorg. Chem.* **1993**.

(79) Payne, M. W.; Corbett, J. D. *J. Solid State Chem.* **1993**, *102*, 553.

(80) Maverick, A. W.; Gray, H. B. *J. Am. Chem. Soc.* **1981**, *103*, 1298.

(81) Maverick, A. W.; Najdzionek, J. S.; MacKenzie, D.; Nocera, D. G.; Gray, H. B. *J. Am. Chem. Soc.* **1983**, *105*, 1878.

(82) Nocera, D. G.; Gray, H. B. *J. Am. Chem. Soc.*, **1984**, *106*, 824.

(83) Jackson, J. A.; Turro, C.; Newsham, M. D.; Nocera, D. G. *J. Phys. Chem.* **1990**, *94*, 4500.

(84) Zietlow, T. C.; Schaefer, W. P.; Sadeghi, B.; Hua N.; Gray, H. B. *Inorg. Chem.* **1986**, *25*, 2195.

(85) Bond, M. R.; Hughbanks, T. *Inorg. Chem.* **1992**, *31*, 5015.

ACKNOWLEDGMENTS

During my Ph. D. research period at Iowa State University, I received help and support from many people both in and out of the group. Without their generosity, the completion of my thesis would have been impossible. I would like to give my special thanks to Dr. John D. Corbett, my major professor, for his patience, guidance and support over the years. I am very grateful to Dr. Hugo F. Franzen and Dr. Robert E. McCarley, as I learned a lot from their classes as well as from private discussions with them.

I would like to acknowledge Dr. Robert A. Jacobson and his group and Dr. Victor Young for their persistent efforts in maintaining single crystal diffractometers. Mr. Jerome E. Ostenson did all the magnetic measurements. His help is greatly appreciated. Special thanks also go to Ms. Shirley Standley. Her daily smile and generous help over the years made my graduate study much easier and more enjoyable. All the group members are sincerely appreciated for sharing their wisdom, experience, humor, and friendship with me and for their constant help in everyday life.

I feel very grateful to my parents for their patience, confidence, and love, and to my brothers for their concern, support, and help prior to and since the day I left home. To all of them I owe my deepest respects. And finally, I wish to particularly thank my husband Baokang whose care, love, encouragement, and help have made my life much more meaningful and my dream come true.